GALVANIC ASPECTS OF ALUMINUM SACRIFICIAL ANODE ALLOYS IN SEAWATER.

Jon Richard Cummings

NAVAL POSTGRADUATE SCHOOL
Monterey, California

THESIS

Galvanic Aspects of
Aluminum Sacrificial Anode Alloys
in Seawater

by

Jon Richard Cummings

December 1977

Thesis Advisor: Jeff Perkins

SECURITY CLASSIFICATION OF THIS PAGE (When Date Entered)

REPORT DOCUMENTATION PAGE

READ INSTRUCTIONS BEFORE COMPLETING FORM

1. REPORT NUMBER	2. GOVT ACCESSION NO.
3. RECIPIENT'S CATALOG NUMBER	
4. TITLE (and Subtitle) Galvanic Aspects of Aluminum Sacrificial Anode Alloys in Seawater	5. TYPE OF REPORT & PERIOD COVERED Master's Thesis; December 1977
6. PERFORMING ORG. REPORT NUMBER	
7. AUTHOR(s) Jon Richard Cummings	8. CONTRACT OR GRANT NUMBER(s)
9. PERFORMING ORGANIZATION NAME AND ADDRESS Naval Postgraduate School Monterey, California 93940	10. PROGRAM ELEMENT, PROJECT, TASK AREA & WORK UNIT NUMBERS
11. CONTROLLING OFFICE NAME AND ADDRESS Naval Postgraduate School Monterey, California 93940	12. REPORT DATE December 1977
	13. NUMBER OF PAGES 170
14. MONITORING AGENCY NAME & ADDRESS(If different from Controlling Office) Naval Postgraduate School Monterey, California 93940	15. SECURITY CLASS. (of this report) Unclassified
	15a. DECLASSIFICATION/ DOWNGRADING SCHEDULE

16. DISTRIBUTION STATEMENT (of this Report)

Approved for public release; distribution unlimited.

17. DISTRIBUTION STATEMENT (of the abstract entered in Block 20, if different from Report)

18. SUPPLEMENTARY NOTES

19. KEY WORDS (Continue on reverse side if necessary and identify by block number)

20. ABSTRACT (Continue on reverse side if necessary and identify by block number)

Galvanic aspects of aluminum sacrificial anode alloys in artificial seawater were investigated. Specifically, two mercury-bearing alloys and one tin-bearing alloy were studied. The polarization behavior of the aluminum sacrificial anode alloys coupled to HY-80 steel is discussed. Current versus time curves were obtained for aluminum/steel galvanic couples

immersed in artificial seawater for specific intervals. Scanning electron microscopy was used to characterize the anode dissolution patterns and the corrosion mechanisms. A correlation is made between the dissolution morphologies exhibited by each anode alloy and the polarization and galvanic current data.

Approved for public release; distribution unlimited.

Galvanic Aspects of Aluminum Sacrificial Anode Alloys in Seawater

by

Jon Richard Cummings
Lieutenant, United States Navy
B.S., University of Missouri, 1971

Submitted in partial fulfillment of the
requirements for the degree of

MASTER OF SCIENCE IN APPLIED SCIENCE

from the

NAVAL POSTGRADUATE SCHOOL
December 1977

ABSTRACT

Galvanic aspects of aluminum sacrificial anode alloys in artificial seawater were investigated. Specifically, two mercury-bearing alloys and one tin-bearing alloy were studied. The polarization behavior of the aluminum sacrificial anode alloys coupled to HY-80 steel is discussed. Current versus time curves were obtained for aluminum/steel galvanic couples immersed in artificial seawater for specific intervals. Scanning electron microscopy was used to characterize the anode dissolution patterns and the corrosion mechanisms. A correlation is made between the dissolution morphologies exhibited by each anode alloy and the polarization and galvanic current data.

TABLE OF CONTENTS

I. INTRODUCTION 19

II. PREVIOUS RESEARCH ON ALUMINUM SACRIFICIAL ANODE ALLOYS 21

III. PLAN OF ATTACK 29

IV. EXPERIMENTAL METHODS 32

A. MATERIALS 32

B. POTENTIODYNAMIC POLARIZATION DETERMINATIONS 33

C. GALVANIC CURRENT MEASUREMENTS 34

D. SCANNING ELECTRON MICROSCOPE AND X-RAY FLUORESCENCE STUDIES 38

V. RESULTS AND DISCUSSIONS 40

A. GALVANIC CURRENT STUDIES 40

B. POTENTIODYNAMIC POLARIZATION BEHAVIOR 46

C. SCANNING ELECTRON MICROSCOPE STUDIES OF ALUMINUM ANODE ALLOYS 52

1. Introduction 52

2. Chronology and Trends of the Corrosion Mechanism of the Galvalum® I Aluminum Sacrificial Anode Alloy 60

3. Chronology and Trends of the Corrosion Mechanism of the Reynode® II Aluminum Sacrificial Anode Alloy 68

4. Chronology and Trends of the Corrosion Mechanism of the KA-90® Aluminum Sacrificial Anode Alloy 73

VI. SUMMARY 78

VII. RECOMMENDATIONS 85

TABLES 88

FIGURES 91

APPENDIX A: Preparation of Artificial Seawater.....154

APPENDIX B: Procedure Developed to Obtain Consistent Results from the PAR-331 Corrosion Measurement System.....156

LIST OF REFERENCES.....165

INITIAL DISTRIBUTION LIST.....170

LIST OF TABLES

I. Potentiodynamic Polarization Data for Freely Corroding Aluminum Sacrificial Anode Alloys.....88

II. Predicted Corrosion Rates of Aluminum Sacrificial Anode Alloys Coupled to HY-80 Steel for Cathode to Anode Area Ratio of 5:4.....89

III. Predicted Corrosion Rates of Aluminum Sacrificial Anode Alloys Coupled to HY-80 Steel for Cathode to Anode Area Ratio of 27:1.....90

LIST OF FIGURES

1. Apparatus used for galvanic current vs. time experiments 91

2. Markson Electromark® analyzer 92

3. Hewlett-Packard Model 428-A clip-on D.C. milliammeter 92

4. Cambridge Stereoscan S4-10 scanning electron microscope 93

5. Princeton Gamma Tech (PGT-1000) X-ray fluorescence analyzer 94

6. MIL-SPEC Zinc anode after fourteen-day immersion test 95

7. Galvalum®I anode after fourteen-day immersion test 95

8. Galvalum®II anode after fourteen-day immersion test 95

9. Galvalum®III anode after fourteen-day immersion test 96

10. Reynode®II anode after fourteen-day immersion test 96

11. KA-90® anode after fourteen-day immersion test 97

12. KA-95® anode after fourteen-day immersion test 97

13. MIL-SPEC Zinc - protected cathode after fourteen-day immersion test 98

14. Galvalum®I - protected cathode after fourteen-day immersion test 98

15. Galvalum®II - protected cathode after fourteen-day immersion test 99

16. Galvalum®III - protected cathode after fourteen-day immersion test 99

17. Reynode® II - protected cathode after fourteen-day immersion test 100

18. KA-90® - protected cathode after fourteen-day immersion test 100

19. KA-95® - protected cathode after fourteen-day immersion test 101

20. Galvanic current vs. time curves of the fourteen-day immersions of Galvalum® I 102

21. Galvanic current vs. time curves of the fifteen-minute, thirty-minute and one-hour immersions of Galvalum® I 103

22. Galvanic current vs. time curves of the fourteen-day immersions of Reynode® II 104

23. Galvanic current vs. time curves of the fifteen-minute, thirty-minute and two-hour immersions of Reynode® II 105

24. Galvanic current vs. time curves of the fourteen-day immersions of KA-90® 106

25. Galvanic current vs. time curves of the fifteen-minute, one-hour and two-hour immersions of KA-90® 107

26. Illustration of macroscopic corrosion patterns on large-scale aluminum sacrificial anode alloy specimens 108

27. Potentiodynamic polarization plots of Galvalum® I, runs 1 and 2 109

28. Potentiodynamic polarization plots of Galvalum® I, runs 3 and 4 110

29. Potentiodynamic polarization plots of Reynode® II, runs 1 and 2 111

30. Potentiodynamic polarization plots of Reynode® II, runs 3 and 4 112

31. Potentiodynamic polarization plots of KA-90®, runs 1 and 2 113

32. Potentiodynamic polarization plots of KA-90®, runs 3 and 4 114

33. Potentiodynamic polarization plot of HY-80 steel 115

34. GI-0.25 (50X) Corroded area on the edge of a Galvalum®I specimen immersed for fifteen minutes 116

35. RII-0.25 (65X) Pitting on broad surface of Reynode®II specimen immersed for fifteen minutes 116

36. KA90-0.25 (60X) Generalized pitting attack on broad surface of KA-90® specimen immersed for fifteen minutes 116

37. GI-24 (610X) Herringbone pattern on dissolution surface of Galvalum®I immersed for twenty-four hours 117

38. RII-24 (600X) Dissolution surface of pit on Reynode®II specimen immersed for twenty-four hours 117

39. KA90-24 (600X) Dissolution surface of KA-90® specimen immersed for twenty-four hours 117

40. GI-0.25 (200X) Galvalum®I specimen immersed for fifteen minutes showing cracked crust formation on an edge of the anode 118

41. GI-0.25 (1250X) Magnified view of Figure 40, showing the unstructured cracked crust 118

42. GI-1 (120X) Galvalum®I specimen after one-hour immersion showing regular patterns on dissolution surface 119

43. GI-1 (1220X) Magnified view of Figure 42, showing the "herringbone" dissolution pattern on one grain surface 119

44. GI-2 (250X) Galvalum®I two-hour immersion specimen showing directionality of the herringbone dissolution pattern on different grains 120

45. GI-2 (650X) Evidence of slight increase of corrosive attack between the grains on Galvalum®I two-hour immersion specimen 120

46. GI-1 (610X) Grain boundary (at upper right) clearly illustrates stepped structure formed by preferential etch of non-close-packed planes.....121

47. GI-4 (63X) Galvalum®I four-hour immersion specimen showing dissolution regions advancing from the edge of the specimen.....122

48. GI-4 (2300X) Galvalum®I four-hour immersion specimen showing cracked film on uncorroded surface.....122

49. GI-12 (110X) Pit in center of Galvalum®I twelve-hour immersion specimen - one of very few dissolution cavities which initiated on the broad surface of a Galvalum®I specimen.....123

50. GI-12 (530X) Magnified view of the center of the pit shown in Figure 49.....123

51. GI-12 (1100X) Magnified view of Figure 50 showing a buildup of corrosion product on the herringbone spine.....123

52. GI-12 (240X) Evidence of increased corrosive attack at grain boundary region of Galvalum®I twelve-hour immersion specimen.....124

53. GI-12 (1200X) Galvalum®I twelve-hour immersion specimen showing buildup of corrosion product on spines of the herringbones.....124

54. GI-24 (220X) Illustration of many symmetrical "herringbone" clusters and the undercutting of an uncorroded area of the Galvalum®I twenty-four-hour immersion specimen.....125

55. GI-24 (2000X) "Herringbone" pattern magnified.....125

56. GI-48 (60X) Illustration of the Galvalum®I forty-eight-hour immersion specimen showing the continuing corrosion attack from the edge inward.....126

57. GI-48 (1220X) Unattacked area on the surface of Galvalum®I forty-eight-hour immersion specimen showing oxide film and flocculent corrosion product.....126

58. GI-72 (1200X) Concentration of corrosion product on top of "herringbone" spine on seventy-two-hour immersion specimen. This area was analyzed by x-ray fluorescence.....127

59. X-ray spectrum of the corrosion product on seventy-two-hour Galvalum®I immersion specimen shown in Figure 58.....127

60. X-ray distribution image for sulfur, showing the presence of sulfur in the same areas as the corrosion product in Figure 58.....128

61. GI-96 (575X) Galvalum®I specimen after ninety-six-hour immersion showing "herringbone" structure and an area of cracked crust.....129

62. GI-96 (230X) Area of ninety-six-hour immersion specimen showing similar patterns as Figure 54 and evidence of the continued undercutting of the oxide film.....129

63. GI-96 (1150X) Corrosion product outcropping on the Galvalum®I ninety-six-hour immersion specimen.....130

64. Galvalum®I specimen polished and etched in 0.5% Hydrofluoric Acid, 32X.....131

65. RII-0.25 (110X) Pitting on surface of Reynode®II aluminum anode specimen immersed for fifteen minutes.....132

66. RII-0.25 (525X) Magnified view of pit in Figure 65.....132

67. RII-0.5 (220X) Dissolution of Reynode®II aluminum sacrificial anode specimen that was galvanically coupled to HY-80 steel and immersed in artificial seawater for thirty minutes.....133

68. RII-0.5 (1100X) Magnified view of the grain boundary at left of center in Figure 67.....133

69. RII-0.5 (1100X) Magnified view of peaks in the grain to the right of center in Figure 67.....134

70. RII-1 (240X) Dissolution of Reynode®II aluminum sacrificial anode specimen that was galvanically coupled to HY-80 steel and immersed in artificial seawater for one hour.....134

71. RII-1 (550X) Magnified view of dissolution cavity in the one-hour immersion specimen which illustrates varying rates of anodic dissolution of several grains 135

72. RII-1 (1100X) Dissolution cavity in the one-hour immersion specimen which illustrates the octahedral, or peak, formations, and variable dissolution rates of Reynode®II grains 135

73. RII-2 (525X) Interior of dissolution cavity in two-hour immersion specimen of Reynode®II illustrating striations within separate grains 136

74. RII-2 (1100X) Peak formations on the two-hour immersion specimen of Reynode®II 136

75. RII-4 (110X) Dissolution of Reynode®II aluminum sacrificial anode specimen that was galvanically coupled to HY-80 steel and immersed in artificial seawater for four hours 137

76. RII-4 (1050X) Magnified view of pit shown in Figure 75 illustrating more rounded octahedrons or peaks 137

77. RII-4 (1200X) Four-hour immersion specimen illustrating varying anodic dissolution rates of separate grains and characteristic peaks 138

78. RII-8 (60X) Extensive dissolution cavity formation in an eight-hour immersion specimen of Reynode®II 138

79. RII-8 (1150X) Evidence of different anodic dissolution rates of grains in Reynode®II eight-hour immersion specimen 139

80. RII-24 (26X) Illustration of development of a dissolution region on the twenty-four-hour immersion specimen of Reynode®II 139

81. RII-24 (1200X) Characteristic peaks and grain boundary within dissolution cavity of twenty-four-hour immersion specimen of Reynode®II 140

82. RII-48 (24X) Reynode®II specimen after forty-eight-hour immersion showing formation of dissolution cavities 140

83. RII-48 (500X) Corrosion product tower emerging from pit on Reynode®II forty-eight-hour immersion specimen 141

84. RII-72 (24X) Reynode®II specimen after seventy-two-hour immersion showing "wormpitting" vertically down the face of the specimen 141

85. RII-72 (610X) Surface of dissolution region on Reynode®II seventy-two-hour immersion specimen showing striations and peaks in various grains 142

86. RII-96 (1100X) Corrosion product on surface of Reynode®II ninety-six-hour specimen which was analyzed with the X-ray spectrometer.....142

87. RII-96 (1100X) Aluminum dot map of corrosion product shown in Figure 86.....143

88. X-ray spectrum of corrosion product shown in Figure 86. The large peaks are (from the left) aluminum, sulfur and chlorine 143

89. Base-metal microstructure of Reynode®II (32X), etched with 0.5% Hydrofluoric Acid. Note dendritic patterns in the grain.....144

90. KA90-0.25 (1200X) Pit in the surface of a KA-90® specimen immersed for fifteen minutes 145

91. KA90-0.5 (60X) Pitting of a KA-90® aluminum sacrificial anode specimen that was galvanically coupled to HY-80 steel and immersed in artificial seawater for thirty minutes 145

92. KA90-0.5 (1200X) Dissolution cavity in KA-90® thirty-minute specimen. Note evidence of surface undercutting and corrosion product buildup 146

93. KA90-1 (20X) Pitting of KA-90® aluminum sacrificial anode specimen that was galvanically coupled to HY-80 steel and immersed in artificial seawater for one hour 146

94. KA90-1 (610X) Magnified view of pit in surface of KA-90® one-hour immersion specimen.....147

95. KA90-2 (1200X) Pit in surface of KA-90® two-hour immersion specimen evidencing corrosion product buildup 147

96. KA90-12 (22X) Distribution of pitting on KA-90® twelve-hour immersion specimen 148

97. KA90-12 (240X) Evidence of pit growth and surface undercutting on KA-90® twelve-hour immersion specimen 148

98. KA90-1 (610X) Hemispherical dome-like "pods" adhering to surface of KA-90® one-hour immersion specimen 149

99. KA90-12 (1200X) Broken "pod" on surface of KA-90® twelve-hour immersion specimen 149

100. KA90-24 (22X) Pitting of KA-90® twenty-four-hour immersion specimen 150

101. KA90-24 (1200X) Intergranular corrosion evidenced in KA-90® twenty-four-hour immersion specimen 150

102. KA90-24 (2400X) Intergranular corrosion evidenced in KA-90 twenty-four-hour immersion specimen.....151

103. KA90-24 (1200X) Intergranular corrosion and grain encapsulation in a KA-90® twenty-four-hour immersion specimen.....151

104. KA90-48 (60X) Accumulation of corrosion product around the pits on the surface of a KA-90® forty-eight-hour immersion specimen.....152

105. X-ray spectrum of corrosion product on a seventy-two-hour KA-90® immersion specimen.....152

106. Sketch of base-metal microstructure of KA-90® aluminum sacrificial anode alloy (100X).....153

B1. Corrosion cell and ancillary attachments atop magnetic stirring mechanism.....162

B2. Princeton Applied Research Model-331, Deluxe Corrosion Measurement System.....163

B3. Hewlett-Packard Model 7040A, X-Y Recorder.....164

LIST OF SYMBOLS

Å	angstrom
ca	about
C.D.	current density
cm	centimeter
cm^2	square centimeter
da	day
d.c.	direct current
dm	decimeter
dm^2	square decimeter
E_{corr}	corrosion potential of single metal
E_{couple}	corrosion potential of metal couple
EMF	electromotive force
eq	equivalent
g	gram
GI	Galvalum®I
hr	hour
I	current (ampere)
I_{corr}	corrosion current of single metal
i_{corr}	corrosion current density of single metal
I_{couple}	corrosion current of metal couple
i_{couple}	corrosion current density of metal couple
in	inch
KA90	KA-90®
kg	kilogram

L(l)	liter
M	mole
mA	milliampere
mdd	milligrams per square decimeter per day
mg	milligram
min	minute
ml	milliliter
mm	millimeter
mmpy	millimeter per year
mpy	mils per year
mV	millivolt
μA	mocroampere
μm	micrometer
ϕ	reduction potential
PFZ	precipitate free zone
RII	Reynode®II
R_{mdd}	corrosion rate in milligrams per square decimeter per day
R_{mmpy}	corrosion rate in millimeters per year
R_{mpy}	corrosion rate in mils per year
SCE	saturated calomel electrode
sec	second
SEM	scanning electron microscope
sq	square
σ	standard deviation
V	volt
W_{lost}	weight lost
$\bar{x}$	average

ACKNOWLEDGEMENT

It is difficult to express adequately the feelings of appreciation that one has upon completion of a Master's Thesis. Succinctly, though, I thank Professor Jeff Perkins for his advice, Professor R.A. Reinhardt for spending many hours as my mentor, Mr. Ken Graham and Mr. Roy Edwards for showing me how to do what I did, and Maureen, Gill and Sean for their understanding and support.

I. INTRODUCTION

The purpose of this thesis is to present the experimental procedures, results and conclusions of research conducted into the galvanic aspects of aluminum sacrificial anode alloys. Several aluminum anodes are now being developed and manufactured. Since a study of all available alloys would be redundant and beyond the scope of this thesis project, a total of six different alloys from three available manufacturers were judiciously selected for this research.

The United States Navy has been aware of the importance of good cathodic protection of its ships hulls for many years [1] and has relied on military specification zinc anodes to afford this protection [2]. Microscopic aspects of the anodic corrosion of these zinc anodes has received attention in previous research at the Naval Postgraduate School [3,4]. In recent years (1973 to present) the zinc anode systems on some surface ships have been replaced with impressed-current cathodic protection systems. "Current" U.S. Navy plans are to install eventually impressed-current systems on all surface ships [5].

Given that the hulls of Naval vessels will be protected by impressed-current systems, one may ask: What use will be made of aluminum sacrificial anodes? It is reported that the aluminum anode will be used in accordance with General Specifications for Ships of the United States Navy, section 633, to protect machinery, bilges, engineering space

structural supports and other internal areas of the ships [5]. Therefore, the present research was initiated to develop a fundamental understanding of the corrosion of commercially available aluminum sacrificial anode alloys.

To achieve this goal a number of experimental approaches was applied, resulting in the accumulation of considerable information on the behavior of the subject materials. Briefly, these experiments were designed to: (1) establish the time-dependence of galvanic current for different aluminum anode alloys when coupled to HY-80 hull steel and immersed in artificial seawater; (2) characterize the polarization behavior of these aluminum alloys in artificial seawater; (3) utilize surface microanalytical techniques such as scanning electron microscopy and energy dispersive x-ray spectroscopy in order to study details of the corrosion processes of the different alloys, and (4) discover if any of the alloys exhibited inhomogeneous attack or passivation effects that might hinder practical application as sacrificial anodes for marine cathodic protection.

Prior to discussing experimental procedures and results, it will be useful to present a brief summary of previous research that led this author to the experimental plan for the present research.

II. PREVIOUS RESEARCH ON ALUMINUM SACRIFICIAL ANODE ALLOYS

To date, the major contributors in the field of research pertaining to aluminum sacrificial anode alloys have been the producers and users of the product. Much research on this subject started in the early 1960's, and an assortment of basic and empirical work has been accomplished in the fields of electrochemistry and physical metallurgy.

It has long been realized that aluminum possesses the primary attributes needed by a sacrificial anode [6], namely: (1) a potential sufficiently electronegative to provide an adequate current flow; (2) a high electrical output per pound of anode consumed, and (3) a sufficiently low cost. However, pure aluminum cannot be utilized as a sacrificial anode because of a protective oxide surface layer which forms on it [7] and limits its current output [7]. Prior to the early 1960's, some aluminum alloy development was partially successful in overcoming the detrimental effects of the oxide film [8], but the alloys were inconsistent in their electrochemical behavior and had a much lower efficiency than the theoretical 1352 ampere-hours per pound of pure aluminum [9].

A major thrust to develop a superior aluminum sacrificial anode alloy began when the economics of the metals industry dictated a shift from conventional zinc- and magnesium-based alloys to aluminum-based materials [10]. Especially as more

and more oil-drilling platforms were put into use, the aluminum industry had greater justification to conduct active research to improve and market economical and useful aluminum alloy sacrificial anodes.

Such research was conducted by producers in Europe [11-15], Japan [16] and the United States [17-30], and consisted of two phases: (1) the development phase [6,8,9,12,16,18,21,27,29], and (2) macro, or bulk, testing of these alloys in laboratory and field conditions [7,10,11,13-15,17-20,22-29].

The United States Navy began to conduct significant research into the usefullness of aluminum sacrificial anode alloys on Naval vessels in the mid-1960's [9]. This research has been centered at the Naval Research Laboratory in Washington, DC [9,31-34]. The results of NRL-based research have been most beneficial to anode producers and have recently resulted in a preliminary Military Specification for aluminum anodes [35].

On the standard EMF series, aluminum is between magnesium and zinc in electronegativity; but for a galvanic series in salt water, it is below magnesium and zinc because of passivation by a surface film [7]. Since research had shown that magnesium and zinc could be made more active by additions of mercury [12], some experimenters believed that mercury added to aluminum would make it more active and prevent passivation [9]. The major problem was in obtaining an aluminum-mercury alloy since a very minute amount of mercury in contact with aluminum is a catalyst for the formation of

aluminum oxide [12]. A simple experiment conducted during this research graphically demonstrated this fact. A specimen of 1100 aluminum was stirred in a beaker of mercury for a few seconds and then withdrawn. A few globules of mercury were on the end of the aluminum specimen. In less than one minute in air, "ribbons" of an aluminum oxide were growing from the tip of the specimen. This growth continued until the movement of the ribbons forced the mercury from the specimen.

In 1963, B. Rachlot developed a method to add small amounts of mercury to aluminum without the catalytic reaction discussed above [12]. It was of interest to develop a mercury-bearing alloy in order to maintain a non-passivated surface on an aluminum sacrificial anode. Rachlot accomplished this by use of a pre-alloy of magnesium-zinc-mercury. This pre-alloy was successful in limiting the catalytic action of the mercury upon aluminum. Rachlot's work also considered the methods by which the appropriate percentage of each alloy constituent was determined [12].

The magnitude and variety of difficulties encountered during initial research toward better aluminum sacrificial anode alloys must be appreciated. As late as 1966 there was only limited information available on the effect of alloy additions on the performance of an aluminum alloy as a sacrificial anode. As with Rachlot, most of the experimentation involved large numbers of empirical observations [7-30]. As a case in point, J.T. Reding and J.J. Newport of the Dow Chemical Company reported that over 2500 alloys were processed

and evaluated in order to be able to produce an anode with a high enough efficiency to be marketable [6].

Reding and Newport made extensive studies of the effects of alloying elements added singly and in combination to aluminum, and determined that gallium, tin, indium, zinc, magnesium, barium, cadmium and mercury caused aluminum to exhibit a potential more anodic than unalloyed aluminum [6]. It was shown that the required concentrations of these elements were quite small. Of course, the effect of each alloying constituent was somewhat different; for instance, mercury-bearing alloys had efficiencies on the order of 90-95%, while some tin-bearing alloys exhibited only 30% efficiencies. When the various favorable elements were combined in various proportions and added to aluminum, Reding and Newport [6] found that aluminum-mercury-tin and aluminum-mercury-bismuth alloys were fairly good, but still not approaching the theoretical efficiency of aluminum, and that aluminum-mercury-zinc, consistent with Rachlot's conclusions, showed a high efficiency, approximately 95% (1290 ampere-hours per pound of aluminum alloy). At this point extensive macro-scale seawater testing was started on the aluminum-mercury-zinc alloy by Dow Chemical Company and the Navy [9,32].

Of major concern to governments and commercial oceanic shippers was the possible mercury contamination which might be caused by an aluminum-mercury-zinc alloy if used in the internal areas of the ships. Even though the actual mercury

content is normally less than one-half of one percent, this was and is a legitimate concern. Although concern about mercury contamination was not publicized until the late-1960's and early-1970's, there were some experimenters, particularly in Japan [16], that were already attempting to find other alloys which had suitable efficiency but lacked the problems of mercury. Sakano, Toda and Hanada [16] found that an anode with long continuing activity and high current efficiency could be prepared by the addition of indium and zinc to aluminum. Reding and Newport [6] had noted that indium was a possible addition to aluminum, but it was quite a few years before Dow Chemical marketed an aluminum-indium-zinc anode (Galvalum® III) [29,30].

Sakano, Toda and Hanada [16] introduced additive elements to the melt in a "pre-alloy" with zinc; galvanic efficiencies of about 92% were obtained. (Smith, et. al., in Ref. 29, reported an 88% efficiency for their aluminum-indium anode ten years after the Japanese work.) This compared quite favorably with the 95% efficiency figure reported by Reding and Newport [6] for aluminum-mercury anodes.

One difficulty with the aluminum-indium-zinc alloy was irregular corrosion patterns over the test anode surfaces. These irregular patterns were obtained in both field and laboratory studies [16]. Various alloy additions were tested to try to increase the uniformity of corrosive attack, and eventually cadmium in small amounts (0.01-0.02%) was found to be useful for this purpose [16]. The distribution of

corrosive attack on the macroscale is important because, after all, an anode must be attached to the structure it is to protect; and if the area around the attachment is corroded or consumed at a higher rate than the remaining portion of the anode, there is a distinct possibility that the anode will fall from the structure long before it has provided its full output.

After laboratory development of the aluminum-indium-zinc anode alloy, it was full-scale tested in the ocean [16]. (Author's note: The tests were similar to other alloy testing and development reported in Refs. 13,17,22,24,etc.) Sakano, et. al. [16], reported that there were some discrepencies between laboratory and ocean data, but they were of such small magnitude that both sets of data were considered accurate enough to begin active commercial production and marketing.

Anode performance tests and evaluations have been conducted on a continuing basis since the early-1960's [7,12,27,33,34,etc.]. Unlike the alloy development work, these tests have not been conducted by the anode manufacturers alone but also by some of the prime users of the products [9,18,21-23,31-34]. Notable in the later category have been Lennox, Peterson, et. al., of NRL [9,31-34], previously mentioned.

With the proliferation of off-shore oil drilling platforms have come series of large field tests [11,13,14,20, 21,23,25,26,28] to verify that aluminum anodes will perform

at their rated values in deep water, thereby protecting the multi-million dollar structure. This is of extreme importance since many drilling rigs require over 200,000 pounds of anodes to provide adequate protection over a 10-20 year period [24]. It has been reported [13,14] that aluminum-mercury-zinc anodes exhibit 90-95% efficiency at depths as much as 490 feet. Davis, Doremus and Bass [24] evaluated the performance of aluminum-mercury-zinc anodes on drilling platforms in the Gulf of Mexico, and verified the high efficiency of these anodes. They also commented that a financial savings of 100% could be obtained with the use of aluminum anodes rather than zinc or magnesium [24].

Some of the significant results obtained by Lennox, Peterson, et. al. [9,31-34], include the following: Aluminum-mercury-zinc anodes typically show efficiencies greater than 90%. When this efficiency is compared to the efficiency of the military specification zinc anode, it is found that the aluminum anode is about 3.5 times as efficient [31]. Electrochemical efficiencies and corrosion patterns of some anode alloys, particularly aluminum-zinc-tin, are found to have such wide variation that their reliability for cathodic protection systems may be questioned [34]. Aluminum anodes of both mercury and tin bearing alloys have been found suitable for protection of ships with structural aluminum alloy super-structures, in that the alloying constituents do not accelerate corrosion of the structural aluminum [33]. Finally, mercury bearing anode alloys, although most efficient,

sometimes exhibit localized corrosive attack at unpredictable sites on the anodes and could, in the long term, result in (dramatically) decreased protection because the anode might fall from the vessel [32].

In 1976, Finn O. Jensen of the Ship Research Institute of Norway agreed with the concerns expressed in NRL findings that aluminum anodes may fall off protected structures. Jensen reported that some anode users (ship and drilling-rig owners) were asking whether any aluminum anodes behaved "as advertised" [11], a concern reported to be especially true in the case of aluminum-mercury-zinc anodes.

The only information to date in the microgalvanic behavior of aluminum anodes was reported in a thesis by P.W. Wright at the Naval Postgraduate School [36]. Wright noted that an aluminum-mercury anode experienced non-uniform microcavity formation over its surface when galvanically coupled and immersed in quiescent artificial seawater. He proposed that the observed mode of dissolution attack is caused by an anti-intergranular corrosion process.

The research conducted for this current thesis was designed to continue the study of the microgalvanic behavior of aluminum anode alloys and to correlate the results, as much as possible, to the previous research discussed in this section.

III. PLAN OF ATTACK

After studying the large amount of information available on the subject of aluminum sacrificial anodes, it became obvious that large scale ocean experiments would be redundant and beyond the scope of this research program. A full-scale on-site experimental program would probably take several years to complete, an amount of time not available. Also, most experimental programs completed to date have involved special on-site structures, such as along sea walls, or elaborate laboratory apparatus. Because this research was not directly funded, a large, complex and extensive study was ruled out in favor of selected laboratory experiments, and it was decided to focus on commercially available aluminum anodes at the microscopic scale. Specifically, it was decided to study the microscopic aspects of corrosive attack using synthetic seawater in the laboratory.

It should be noted that the U.S. Navy has apparently already decided, on the basis of empirical studies [9,31-34], what type of alloy should be used aboard surface vessels, and a preliminary military specification has been drafted [35]. Early in the conception of this study, it was verified [37,38] that information on the microscopic behavior of various anodes would certainly provide basic insight and might even be of practical use, such as contributing to the iterative process of alloy development. To be quite frank,

cognizant individuals in the Navy Department have not expressed much interest in the microscopic properties of sacrificial anode alloys, apparently because their philosophy is more oriented towards large scale empirical results.

Prior to beginning the experimental portion of this thesis a decision was made to obtain representative samples of the basic types of commercially available aluminum anodes, i.e., aluminum-mercury-zinc, aluminum-tin-zinc, and aluminum-indium-zinc alloys. With the assistance of Dow Chemical U.S.A., Reynolds Metal Company and Kaiser Magnesium Company, these types of aluminum sacrificial anode alloys were obtained.

It was then prudent to construct an experimental plan of attack, a data matrix and a list of basic questions that needed answers. Such questions included the following:

1. Do aluminum anode alloys that have similar alloy constituency (e.g., aluminum-mercury-zinc) experience the same form of corrosive attack (on the macroscale) and have similar dissolution patterns (on the macroscale)?

2. Do the microstructural characteristics of the alloys, such as affected by casting and/or heat treating processes, affect the corrosion mode and morphology?

3. Exactly what is the distribution and mode of corrosive attack on the various alloys?

4. What is the relation between microscale corrosion processes and galvanic current output?

5. Can the utilization of small specimens in a limited test program provide information that can be correlated with large-scale field tests.

6. If information relating to basic differences between the corrosion behavior of the various alloys can be obtained, can this information be utilized to make viable decisions relative to the utility of the various alloys, and in what circumstances is it necessary to go to full-scale field tests?

7. What are the polarization characteristics of the various alloys, and what is their relationship to, and correlation with, the modes of corrosive attack and galvanic current output?

8. What are the corrosion products formed on sacrificial aluminum anode alloys in seawater?

IV. EXPERIMENTAL METHODS

A. MATERIALS

Six commercially-developed aluminum sacrificial anode alloys were obtained from three producers for study in this research. The alloys and trade names are proprietary. The nominal chemical compositions are as follows:

Galvalum®I*:	0.047%Hg	Reynode®II**:	1.25-2.0%Zn
	0.45%Zn		0.03-0.06%Hg
	0.019%Cu		0.003%(max)Cu
	0.034%Fe		0.07%(max)Fe
Galvalum®II*:	0.048%Hg	KA-90®***:	6.0-7.4%Zn
	0.0018%Cu		0.12-0.20%Sn
	3.0%Zn		<0.1%Fe
	Fe - not determined		<0.1%Si
			<0.005%Cu
Galvalum®III*:	0.0156%In		
	2.9%Zn	KA-95®***:	1.2%Zn
	0.13%Si		0.05%Hg
			<0.1%Fe
			<0.1%Cu

Obtained from: *Dow Chemical U.S.A.

**Reynolds Metal Company

***Kaiser Magnesium Company

These anode materials were machined into specimens for polarization studies and galvanic current measurements.

B. POTENTIODYNAMIC POLARIZATION DETERMINATIONS

Potentiodynamic polarization studies were conducted to determine the single metal corrosion rates and polarization characteristics of the aluminum sacrificial anode alloys [39]. These tests were conducted in artificial seawater electrolyte [Appendix A]. The specific procedural methods are described in Appendix B of this thesis. The potentiostat used was a Princeton Applied Research Model-331 Deluxe Corrosion Measurement System (Figure B2, Appendix B). A rapid-scan potentiodynamic technique was used by which the potential was scanned from the least noble potential through E_{corr} (corrosion potential) to the most noble potential. It has been postulated that this rapid-scan technique is successful [40] because dissolved oxygen is removed from the specimen surface by hydrogen liberation during the cathodic polarization, and the anodic polarization curve is completed before the oxygen is replenished. Also, the electrode (specimen) is electrochemically cleaned during the cathodic reactions, and the plotting of the anodic curve is completed before the surface returns to an equilibrium state [40].

It was noticed at the start of the polarization studies that the aluminum sacrificial anode alloys were very sensitive to changes in the specimen preparation method and the techniques used when running the potentiostat. But after developing a standardized procedure (Appendix B), accurate and reproducible potentiodynamic measurements were obtained [41].

Briefly, the specimen preparation consisted of surface finishing and cleaning, standard timing (two minutes) between immersion in the electrolyte and commencement of the potentiodynamic polarization run, and a standard operational "check-list" to insure that each run was conducted in precisely the same way.

C. GALVANIC CURRENT MEASUREMENTS

These experiments were designed to determine the galvanic current produced by an aluminum sacrificial anode alloy coupled to HY-80 steel and immersed in quiescent artificial seawater, and it was intended to study subsequently these anode specimens microscopically in order to investigate the details of the corrosion process.

Initially, six different aluminum anode alloys were studied in duplicate, fourteen-day immersion tests. After these initial trials were completed, three of the six alloys were selected for further study. The three alloys were: Galvalum®I, Reynode®II and KA-90®. Each of these three alloys was subjected to a series of ten timed-interval immersions of from fifteen minutes to 96 hours. These timed-interval tests were intended to provide a history of the corrosion process as well as additional galvanic current data.

Design of the cells for galvanic current measurements was kept simple so as to reduce unknown parameters. The apparatus used is shown in Figure 1, consisting of an array of 3000 ml beakers, each containing 2500 ml of artificial

seawater. Aeration was accomplished by connections to a manually regulated air supply to simulate the aeration of ocean water at the level of ships-hull anodes and of bilge water. The instrumentation used to measure the galvanic current, pH, and conductivity of the electrolyte is shown in Figures 2 and 3. A clip-on d.c. milliammeter was used to obtain galvanic current.

The clip-on d.c. milliammeter does not interrupt the electrical circuit in order to obtain a current reading. The head of the electrode-probe, seen in Figure 3, separates to fit around a wire and is firmly closed to obtain a reading. For accuracy and consistency in the use of such a meter, it must be kept in mind that the meter actually measures magnetic flux that surrounds the wire and is therefore sensitive to the magnetic flux of the earth. All readings must be taken with the probe degaussed and consistently oriented in the same geometric plane.

As previously stated, construction of the galvanic cell was simple in design. The aluminum sacrificial anode specimen was connected to an HY-80 steel cathode with 14 in. (36 cm) of insulated #12 solid copper wire having a resistance of 1.85×10^{-3} ohms, a resistance considered negligible to these experiments. The HY-80 steel cathode had dimensions of 3.25 in. x 3.25 in. x 0.13 in. (8.25 cm x 8.25 cm x 0.32 cm), giving a surface area ratio between the opposing faces of the cathode and anode of approximately 46:1. Specimens machined for galvanic current measurements were 0.48 in. x 0.48 in. x 0.20 in. (1.22 cm x 1.22 cm x 0.51 cm). A 0.375 in. (0.95 cm) deep

hole was drilled into one side of the specimen, and a #12 copper wire was inserted to connect the aluminum anode and HY-80 steel cathode.

Consistency in experimental procedure is of course essential to allow the researcher to collect accurate and reliable data in a series of experiments. Therefore, the total of thirty timed-immersion tests were conducted with special care to employ a consistent procedure. All the galvanic couples were prepared and tested in the same manner so that variations in results obtained could be reasonably assumed to be associated with differences in the characteristics of the subject materials. The following is a chronology of steps taken to prepare the materials, laboratory apparatus and galvanic cells.

HY-80 plates were cut to size, with a hole (sized for #12 gauge wire) drilled into one edge. Surfaces of the steel plates were not polished, so that they would more accurately represent actual hull plating. The plates were ultrasonically cleaned in acetone and boiled in a solution of 20% NaOH and 200 g/l zinc dust for ten minutes [42], then cleaned with steel wool, rinsed with acetone and alcohol, and blow-dried with warm air. The steel plates were stored under a nitrogen blanket in sealed plastic bags to minimize corrosive action prior to their use.

The laboratory apparatus was thoroughly cleaned prior to filling each beaker with 2500 ml of artificial seawater.

The end of the aeration tubing was placed 0.25 in. (0.64 cm) to 0.5 in. (1.3 cm) from the bottom of the beaker, and air supplied to each beaker was mechanically regulated to provide approximately the same amount of aeration in each test. Prior to the start of each immersion test, the artificial seawater was aerated for two hours, with aeration continued through the timed immersion.

Fourteen-inch (36 cm) sections of #12 gauge copper wire were connected between the sacrificial aluminum anode specimens and HY-80 steel plates. The anodes and cathodes were sharply peened at the spot above the inserted wire to insure a better mechanical bond. For immersion tests of 96 hours or longer, an epoxy resin was used to seal the area around the inserted wire, and paraffin was used to seal this area for all other immersion tests. Both of these sealing techniques were successful in preventing bi-metallic corrosion at this area.

After the anodes and cathodes were connected, they were cleaned with acetone and blow-dried. The anode and cathode were placed approximately 4 in. (10 cm) apart with faces parallel. This galvanic couple was placed in the cell in a position to avoid the bubbles from the aeration systems and keep the anode and cathode from touching the side of the beaker. The probe of the clip-on d.c. milliammeter was placed around the wire of the galvanic cells used for the fifteen-minute to 24-hour timed-immersion tests prior to inserting the cells into the electrolyte. This was done to avoid moving the cell during the immersion test because the

galvanic current was being monitored on a strip-chart-recorder, and movement of the cell was found to vary the galvanic current.

As a summary note, the above procedures were in accordance with the applicable sections of Ref. 42.

D. SCANNING ELECTRON MICROSCOPE AND X-RAY FLUORESCENCE STUDIES

Aluminum sacrificial anode alloy specimens that were used for the timed immersion (galvanic current) tests were also used to study the microscopic corrosion mechanisms of the Galvalum®I, Reynode®II and KA-90® alloys. A Cambridge Stereoscan S4-10 scanning electron microscope (SEM) and a Princeton Gamma Tech (PGT-1000) X-ray fluorescence analyzer were used in these studies. These instruments are illustrated in Figures 4 and 5.

A difficulty in using the SEM to study corroded aluminum anodes is the electron charging of the corrosion products. Bombardment of the non-conductive corrosion products with an electron beam tends to build up a charge which, if not conducted away, causes image distortion. In order to minimize the electron charging, a 40-50 Å layer of gold was evaporated over the specimen surfaces [43]. This technique was successful for all specimens except some (KA-90®) specimens which had significant corrosion product present, in which case the gold coating did not significantly improve the photo quality at high magnifications. One specimen of each alloy was not gold coated so that it could be used with

the PGT-1000, in conjunction with the SEM, in an attempt to determine the chemical makeup of the corrosion products.

V. RESULTS AND DISCUSSION

A. GALVANIC CURRENT STUDIES

Fourteen-day immersion tests were done twice with each of the six available aluminum sacrificial anode alloys. Duplicate testing was accomplished to gather redundant galvanic current vs. time data for each alloy and to establish baseline information to aid in the selection of alloys for more detailed study. One zinc alloy anode was also tested in a fourteen-day test. Galvanic current vs. time curves were prepared in order to make comparisons with the predictions of potentiodynamic polarization curves. Also, it was planned to correlate visual observations of the galvanically exposed samples with trends exhibited by the galvanic current vs. time curves. The fourteen-day tests produced very similar electrochemical data for the various alloys but distinctly different macro-galvanic corrosion characteristics and morphology. Macrophotographs of the anodes and cathodes after these immersion tests are shown in Figures 6 to 19.

Two sets of curves are presented for each of the three alloys investigated (Figures 20-25). One set of curves (Figures 21,23,25) presents galvanic current for short immersion times, i.e., fifteen minutes to two hours, while a separate set of curves (Figures 20,22,24) shows galvanic current as a function of time over the entire fourteen-day immersion periods.

Observations from the galvanic current vs. time curves include the following:

1. The aluminum anodes have a relatively high starting current density (C.D.) compared to MIL-SPEC zinc. For instance, the MIL-SPEC zinc anode tested showed a starting C.D. of approximately 3mA/cm^2, while Galvalum®I started at about 4.5mA/cm^2, Reynode®II started at about 7.4mA/cm^2, and KA-90® started at about 8.4mA/cm^2. The high starting C.D. of KA-90® may be related to the large number of pits that form on the surface of the specimens within fifteen minutes after the start of each immersion.

2. The aluminum sacrificial anode alloys all exhibit the same general trend of galvanic current, with a high starting C.D. which rapidly decreases to a stable value.

3. The decrease in galvanic current output from each anode with time is not entirely attributable to a passivation phenomenon on the anode surface but is also due to calcareous deposits which form on the coupled cathodes. This deposit reduces the cathodic area which the anode has to protect, thereby lowering the required galvanic current output.

The fourteen-day immersion tests produced very similar electrochemical data for the various alloys but distinctly different macro-galvanic corrosion characteristics and morphology. MIL-SPEC zinc (Figure 6) shows a more general uniform pattern of corrosion than any of the aluminum alloys, with no local dissolution cavities. The surface of the zinc anode becomes covered with a powdery white corrosion product

which has previously been determined to consist of an array of microscopic zinc oxide crystal platelets [3,4].

All mercury-bearing alloys, except Galvalum®II (Figure 8), show attack that is free of corrosion product buildup. Galvalum®I, Reynode®II and KA-95® (Figures 7,10 and 12 respectively) develop a corrosion pattern that has previously been reported as typical of mercury-bearing anode alloys [9,31-34], consisting of large areas of general dissolution, with other areas of the surface void of significant corrosion, or corrosion product. On the other hand, Galvalum®II becomes covered with a white and fragile corrosion product (Figure 8).

The specimen of Galvalum®I shown in Figure 7 is seen to have corroded along the lower edge of the specimen, while the Reynode®II specimen in Figure 10 formed two elongated dissolution cavities parallel to its vertical edges. It is characteristic of the respective anode alloys to corrode in this manner, i.e., Galvalum®I tends to corrode along specimen edges, while Reynode®II tends to develop a set of parallel elongated cavities on the surface of the specimens, that grow by "worming" vertically down the face.

Both of the alloys (Galvalum®I and Reynode®II) have approximately the same alloy composition, but Reynode®II is heat treated. It is reasoned that the heat treatment of Reynode®II, as compared to the simple chill casting of Galvalum®I, must account for the distinct differences in corrosion patterns observed for these two alloys. While an exact mechanism accounting for the different behaviors cannot

be described, it may be that the heat treatment effect is realized in terms of the location of alloying elements in the respective microstructures. This contrast in behavior between two compositionally similar commercial anode alloys serves to point out that factors other than alloy composition can be of great importance in aluminum sacrificial anode alloys. This becomes particularly evident when comparing the macroscopic corrosion patterns.

The macroscopic appearance of KA-90® (mercury-zinc-tin alloy) after fourteen days exposure is illustrated in Figure 11. The specimens are coated with a white, brittle corrosion product which when dried and scraped from the specimens reveals a uniformly corroded surface. The corroded anode is brittle, and relatively large areas of it can be chipped off. The texture of the corroded KA-90® anode is grainy and coarse, indicative of severe intergranular corrosion. It would be of interest to conduct velocity studies with the KA-90® alloy to determine what effect, if any, this mode of corrosive attack may have on the erosion characteristics.

Tin is added to the alloy composition in order to increase the potential above the potential of pure aluminum [16]. It was reported in Ref. 6 that small additions of tin (0.12-0.20%) will increase the potential of aluminum from 0.7 volts SCE to approximately 1.3 volts SCE, with any greater addition not having a significant effect.

One might ask whether observations on these small-scale anode coupons are comparable with the behavior of full-scale

sacrificial anodes. The answer is very definitely "yes", as can be seen by comparing the macroscopic photographs of specimens studied in this research (Figures 6 through 12) with the macroscopic appearance of large scale field test specimens (Figure 26) [44].

When the fourteen-day immersion studies were completed three alloys were selected for in-depth studies: Galvalum® I, Reynode® II and KA-90®. Galvalum® I and Reynode® II were selected because of their mercury content (They met the alloy constituent percentages indicated in the preliminary military specification [35].) and KA-90®, because it displays a high initial galvanic current and has a different alloy constituency.

Two other notable observations of the fourteen-day immersion tests are:

1. All cathodes connected to the anodes become covered with a calcareous deposit, resembling calcite (calcium carbonate)..

2. A large amount of flocculent precipitate forms and settles out in the artifical seawater (collecting in the bottom of the cells in these tests).

Figures 13 through 19 show macrophotographs of the various cathodes, with some calcareous deposits remaining on them after most of the deposits were removed for x-ray diffraction analysis. Cathodes galvanically coupled to Reynode® II and KA-90® anodes had more deposits on them than cathodes coupled to the other anodes.

Artificial seawater (Appendix A), containing predominately sodium chloride, also contains significant amounts of bicarbonates and sulphates [45]. These compounds are important in the corrosion process because they act as cathodic inhibitors [46]. Under quiescent conditions, as in the fourteen-day immersion tests, calcium carbonate and other compounds may be precipitated at the cathodic areas [46]; and if the deposits adhere to the cathodic surfaces, the cathodic process will be stifled [45]. The calcareous deposits effectively reduce the area of the cathode and therefore reduce the anodic current output required for adequate cathodic protection [46,47]. It is believed that this factor contributed to the reduction in galvanic current output observed for all the aluminum anode alloys tested. This may be of particular importance in the case of the alloy anodes which do not become covered with corrosion product, i.e., Galvalum®I, Reynode®II, Galvalum®III and KA-90®.

X-ray diffraction analyses were conducted on the deposits removed from the cathodes that had been galvanically coupled to the Galvalum®I, Reynode®II and KA-90® anodes. These analyses were not totally conclusive, but there was good correlation with some peaks of calcium carbonate and a dihydrous calcium sulphate ($CaSO_4 \cdot 2H_2O$). Per LaQue [47], the composition of calcareous deposits found on steel cathodes immersed in seawater includes calcium carbonate and calcium sulphate, plus various other bicarbonates, sulphates and water. The variable proportion of water bound in the various

compounds [48] is what causes difficulty in identification by x-ray diffraction. While positive identification was not possible, it was observed that the cathodic deposits for different anodes have identical x-ray diffraction patterns, which at least verifies that the deposits are of the same identity, independent of the coupled anode alloy.

Formation of the opaque, flocculent precipitate in the seawater was in the same proportion as the calcareous deposits on the cathodes. That is, couples involving Reynode®II and KA-90® form the most precipitate. The cell solutions used for the timed immersion tests of Galvalum®I, Reynode®II and KA-90® were subsequently filtered to collect these precipitates, which were then analyzed by x-ray diffraction. The finely powdered precipitate material did not produce coherent x-ray diffraction patterns, indicating that it is either an amorphous substance, or if crystalline, the crystals are so small the x-ray peaks are smeared out.

B. POTENTIODYNAMIC POLARIZATION BEHAVIOR

The freely corroding potentiodynamic polarization behavior of Galvalum®I (Figures 27-28) is very similar to that of Reynode®II (Figures 29-30). Parameters such as I_{corr}, R_{mdd}, etc. (Table I), obtained and calculated from these potentiodynamic polarization curves (Figures 27-30) have small standard deviations. Potentiodynamic polarization curves for freely corroding KA-90® (Figures 31-32) were not as consistent as those of Galvalum®I and Reynode®II; but even so, the data has reasonably small standard deviations (Table I). Consistent

procedures and constant polarization parameters, described in Appendix B, insured this repeatability.

Potentiodynamic polarization curves of freely corroding metal cannot by themselves predict the corrosion potential and current when the metal is galvanically coupled. During galvanic current tests in this research, and in practical applications, aluminum anodes are galvanically coupled (in these experiments, to HY-80 steel). Therefore, it was of interest to see if the independent potentiodynamic polarization curves of the coupled metals would predict the actual corrosion rates experienced by the aluminum anodes in the galvanic current immersion tests. To this end, a potentiodynamic polarization curve of HY-80 steel was obtained, utilizing the same technique as for the aluminum anodes. The polarization curve for the HY-80 steel is shown in Figure 33.

Using the HY-80 steel polarization curve in conjunction with the aluminum anode curves enabled this author to predict the corrosion characteristics of the HY-80 steel and aluminum anode galvanic couples in artificial seawater. Calculations (as outlined below) were made for cathode to anode area ratios of 5:4 and 27:1. Five:four is the ratio of the area of the HY-80 steel specimen to that of the aluminum anode specimens, which were independently used for the potentiodynamic polarization runs. Twenty-seven:one is the ratio of the area of the steel plate cathode to that of the aluminum anode specimens used in the coupled galvanic current tests. The polarization data for freely corroding aluminum sacrificial

anode specimens are listed in Table I, and the predicted values obtained for these area ratios are listed in Tables II and III.

A few comments are necessary about the procedures used to make the area ratio calculations. Data for I_{couple} (μA) and E_{couple} (Volts, SCE) for the 5:4 ratio galvanic couple were obtained by placing the HY-80 steel potentiodynamic polarization curve directly over the aluminum anode polarization curves and marking the intersection of the cathodic branch of the HY-80 curve and the anodic branch of the aluminum anode curves. The intersection points of the curves are marked with a dot on Figures 27 through 32.

Calculations of the aluminum anode's predicted corrosion rates (R_{mdd}, R_{mmpy}, R_{mpy}) were made from these data (Table II).

Data for I_{couple} (μA) and E_{couple} (Volts, SCE) for the 27:1 ratio galvanic couple were obtained by placing the potentiodynamic polarization curve of the HY-80 steel over the polarization curves of the aluminum anodes and then moving the HY-80 curve 1.11 decades (on the log scale) to the right. This 1.11 decade shift compensates for the ratio between the 5:4 and 27:1 surface area ratios. The intersections of the cathodic branch of the HY-80 steel polarization curve with the anodic branch of the aluminum anode curves are marked by an asterisk on Figures 27 through 32. Calculations of the aluminum anode's predicted corrosion rates (R_{mdd}, R_{mmpy}, R_{mpy}) in a 27:1 (steel-aluminum couple) ratio were made from these data (Table III).

Data from the fourteen-day immersion tests were used to verify the accuracy of the predicted corrosion rates, by comparing the predicted values with the actual aluminum anode specimen weight loss. The fourteen-day immersion test data were selected for this verification because the HY-80 plate: aluminum anode galvanic couples maintained nearly constant current over this period.

The analytical procedure used to compare (1) the anode weight loss predicted from the polarization curves, (2) the weight loss calculated by integrating the area under the current vs. time curves, and (3) the actual weight measurements is described below.

(a) The total number of coulombs produced by the galvanic couples of HY-80 steel and Galvalum®I, Reynode®II and KA-90® anodes over a 340-hour immersion period was calculated by graphical integration of the galvanic current vs. time curves (Figures 20,22,24). Results of these integrations are:

Galvalum®I: 4.3×10^3 amp-sec

Reynode®II: 4.6×10^3 amp-sec

KA-90®: 6.1×10^3 amp-sec

(b) The number of coulombs produced by the galvanic couples was used to calculate the weight loss for each of the three anode alloys for the 340-hour immersion period. Results of these calculations are:

Galvalum®I: 0.40g

Reynode®II: 0.43g

KA-90®: 0.68g

Calculation for Galvalum®I is shown below:

$$W_{lost} = \frac{26.98 \text{ g/mole}}{3 \text{ eq/mole} \times 96500 \text{ amp-sec/eq}} \times 4.3 \times 10^3 \text{ amp-sec} = 0.40\text{g}$$

(c) Corrosion rates in mdd, calculated from these predicted weight losses, are:

Galvalum®I:	698.0 mdd
Reynode®II:	745.7 mdd
KA-90®:	1172.0 mdd

Calculation for Galvalum®I is shown below:

$$\frac{0.40\text{g}}{340 \text{ hr} \times 4.07 \text{ cm}^2} \times 24 \frac{\text{hr}}{\text{da}} \times 1000 \frac{\text{mg}}{\text{g}} \times 100 \frac{\text{cm}^2}{\text{dm}^2} = 697.7 \frac{\text{mg}}{\text{dm}^2\text{-da}}$$

(d) Physical measurements of aluminum anode specimen weight losses after the fourteen-day immersion are (±0.05g):

Galvalum®I:	0.38g
Reynode®II:	0.45g
KA-90®:	0.87g

Correlation between the physical weight loss measurements and weight loss calculations (using the galvanic current vs. time curves) is extremely good for all three anode alloys. Correlation between the actual weight loss measurements (both physical and calculated) and the predicted weight loss calculated from the potentiodynamic polarization data is not as good as expected, but still within an order of magnitude.

For instance, Galvalum®I's predicted weight loss (in mdd) is 164.7 (Table III) and its actual weight loss is 698.0 mdd.

Consideration of the characteristics of the aluminum potentiodynamic polarization curves (Figures 27-32) enables predictions regarding the macroscopic anodic behavior of the respective anode alloys. For example, on this basis it is predicted that Galvalum® I and Reynode®II anode specimens, when galvanically coupled to HY-80 steel with an area ratio of 27:1 and immersed in quiescent artificial seawater, will not experience significant pitting on the specimen's surfaces. On the other hand, it is predicted the KA-90® aluminum anode specimens will experience significant pitting. These predictions are based on the characteristics of the anodic branches of the polarization curves, as follows.

Polarization curves for Galvalum®I and Reynode®II (Figures 27-30) show that a relatively large potential must be applied in order to obtain the transpassive, or pitting, region of the anodic branch of the polarization curve. The polarization of KA-90® is quite different from that of Galvalum®I and Reynode®II. Polarization curves for KA-90® (Figures 31-32) do not show an abrupt transition to a transpassive region during anodic polarization. The implication of this is that Galvalum®I and Reynode®II will not experience general pitting, while KA-90® will. These predictions are validated by scanning electron microscope photographs (Figures 34-39) and macrophotographs of the aluminum anode specimens (Figures 2,7,11).

C. SCANNING ELECTRON MICROSCOPE STUDIES OF ALUMINUM ANODE ALLOYS

1. Introduction

A difficulty faced by those interested in improving cathodic protection systems has been a lack of information concerning the actual corrosion mechanisms involved. There is an abundance of data relating to the macroscopic findings of large scale corrosion testing, but the corrosion processes actually take place on a microscopic level. In order to establish the microscopic corrosion processes of aluminum sacrificial anode alloys, scanning electron microscopy was used extensively in the present research to study the surfaces of aluminum anode alloys after various exposures. Scanning electron microscopy (SEM) provides the researcher with information that can be used to develop ideas about corrosion mechanisms. While much of this information is descriptive, there is considerable theory available to which the descriptive material can be correlated.

The representative SEM photographs included in the Figure section of this thesis are numbered with a simple index system. For instance, a 1000X photograph of a Galvalum® I specimen which had been immersed for one-quarter hour would be indexed as GI-0.25 (1000X), a 610X photograph of a Reynode® II specimen which had been immersed for twenty-four hours would be indexed as RII-24 (610X), and a 200X photograph of a KA-90® specimen immersed for twelve hours would be indexed as KA90-12 (200X).

Figures 34,35 and 36 illustrate rapid pit formation on the surface of the Galvalum®I, Reynode®II and KA-90® alloys, respectively, after fifteen-minute exposures in (area ratio 27:1) couples with HY-80 steel. Figure 34 shows that a Galvalum®I specimen immersed for fifteen-minutes exhibits dissolution localized along specimen edges, as noted earlier (for the fourteen-day immersion test specimen). Figure 35 shows that the local dissolution of the Reynode®II alloy specimens begins as pits on the broad surface faces, rather than along the edge of the specimens like Galvalum®I. The KA-90® aluminum-tin-zinc sacrificial anode alloy demonstrates rapid and uniform pit formation over the entire specimen surface, illustrated by Figure 36 which shows numerous pits on the order of 30 μm in diameter.

Aluminum, exposed to air, forms an oxide film, generally considered to be γ-Al_2O_3 [49]. This film has been regarded as a protective coating which prevents aluminum and its alloys from corroding in seawater. One of the questions to be addressed by the present research was: At the microscopic level, what mechanisms can lead to breakdown of the passivating film and the start of pit formation on aluminum anodes when coupled to steel and immersed in artificial seawater?

In fact, the observations in this work (such as Figures 34,35,36) do not all constitute classical pitting. Classical pitting is considered to be rapid localized corrosive action with deep penetrations and insignificant

weight losses. This thesis research tended to support some pitting theories more than others, and the start of any given pit could possibly have been a combination of more than one mechanism. KA-90® appears to be attacked by a "true" pitting mechansim, i.e., the attack of KA-90® more closely resembles classical pitting than does that of Galvalum®I or Reynode®II.

There are numerous existing theories pertaining to pit formation, and most of these theories, of course, are dependent on the concepts favored by the particular investigators [50]. A few pitting concepts that are considered germane to this thesis research are discussed below.

Keir, Pryor and Sperry [51] showed that tin, a basic alloy constituent of KA-90®, reduces the corrosion resistance of the aluminum oxide film if the tin is dispersed relatively uniformly in the solid solution substrate. Therefore, localized breakdown of the general oxide passivating film on an aluminum anode could occur.

Richardson and Wood [49] are in general agreement with Keir, et. al. [51], but they believe that flaws in the surface of the oxide film can create additional sites for localized pitting. These flaws may be residual, produced during the film growth at "impurity-rich" (alloy-rich) regions in the metal, or mechanical in origin [49]. Mechanical flaws may be associated with the relief of stresses in the film which results from oxide formation over mechanical surface defects such as machine marks or gouges [49].

An anode initially subjected to high current density, or an anode that requires a small potential increase to go from cathodic polarization to transpassive (pitting). polarization, tends to experience rapid pit formation followed by lateral growth, or local dissolution, of the pits [49]. All of the aluminum sacrificial anode alloys studied during this thesis research had relatively high initial current densities compared to the initial current density of MIL-SPEC Zinc. KA-90® had the highest current density, and as evidenced in Figure 36, the largest number of pits per unit surface area. The potentiodynamic polarization behavior of KA-90®, as determined in this work, directly correlates with this microscopically observed behavior, supporting the concept that rapid attainment of transpassive behavior is associated with enhanced pit formation. The polarization behavior of KA-90® is shown in Figures 31 and 32.

Pryor, et. al., [50,51] suggested that chloride ions in the electrolyte are an incentive to pit formation and growth when aluminum is galvanically coupled to steel in seawater. It is believed by this author that the pitting mechanisms discussed above can be applied in part to explain the initiation of pits on the aluminum anodes studied in the present research.

However, again referring to Figures 34,35 and 36, it can be seen that quite different anodic dissolution mechanisms are involved in the initial corrosive behavior of the three alloys. The reason for these differences cannot be found in

any unified theory for pitting. Galvalum®I and Reynode®II have very similar alloy compositions, but Reynode®II is heat treated after a chill casting to resolution zinc and mercury [52] and then air cooled. It would thus be logical to assume that initial pit formation on Reynode®II (tending to locate on the broad surface faces rather than the edges of the specimens) is related to some effect of the heat treatment. All alloy constituents, e.g., mercury, copper and iron [16], are nominally present in similar amounts in Galvalum®I and Reynode®II, but these elements are clearly not distributed the same in these two alloys. It is not clear whether the effect is macroscale or microscale. That is, there may be differences in concentration on the macroscale across the ingots from which the samples were machined, i.e., segregation from edge-to-center, or there may be differences in the distribution of alloying constituents in the microstructures of the respective Galvalum®I and Reynode®II alloys. It is also believed that surface flaws may contribute to the more general pit formation observed on Reynode®II, as opposed to the edge-localized attack on Galvalum®I. This is hypothesized because the specimens of both Galvalum®I and Reynode®II were prepared in the same way, so that the initial surface condition of all specimens was approximately the same. In spite of this, Galvalum®I exhibits dissolution indicating greater sensitivity to macroscopic geometric discontinuities and edge effects, while Reynode®II is insensitive to such features.

As previously mentioned, KA-90® anode specimens exhibit rapid and uniform pit formation of a more classical type over the entire surface (Figure 36). This behavior lends credence to the pit-formation concepts stated by Pryor, et. al. [51]. Pryor's research indicated that tin will reduce the corrosion resistance of an aluminum oxide (γ-Al_2O_3) film but only if the tin is evenly dispersed in the aluminum substrate, as it is in the heat treated KA-90®. Pryor notes that only about 0.1% tin can be retained in a metastable solid solution [51], but that homogenized aluminum-tin alloys containing greater than 0.1% tin will still corrode quite uniformly when coupled to steel and in a sodium chloride solution. KA-90® contains from 0.12 - 0.20% tin, and it is seen to corrode "evenly", i.e., shows pitting attack that is uniformly distributed over its surface.

In summary, it appears that a variety of mechanisms are working to initiate the corrosion process on different aluminum sacrificial anode alloys. In the case of the alloys studied in this work, it is somewhat arbitrary, when observing the various modes of attack, as to what should be considered classical pitting and what should be considered as simply local dissolution. It was decided that "pits" initially formed on Galvalum®I and Reynode®II do not propagate by a classical pitting mechanism; instead they enlarge as "local dissolution cavities". However, in the case of KA-90®, the high initial current density together with the particular polarization behavior, alloy homogenization, and environmental

factors contribute to localized breakdown of the aluminum oxide film, and a true "pitting" mechanism operates.

Another question is: By what mechanism do the various alloys corrode after initial pit formation? It is seen from the current vs. time curves (Figures 20-25) that the electrochemical properties of the galvanic couples change with time. Galvanic current, which starts at a relatively high value for all the anode types, rapidly decreases and then maintains itself at an apparently stable value. Pits which are initially formed grow into larger "local dissolution cavities" or propagate as "true pits", and distinct surface morphologies become evident on the dissolution surfaces when viewed microscopically.

Within the first twenty-four hours of immersion, a number of similar macroscopic aspects of corrosion are exhibited by the three aluminum sacrificial anode alloys, including the following:

1. The corrosion process decreases the total mass of each anode but increases the surface area;

2. Calcareous deposits form on the cathodes;

3. Corrosion products form, to various extents, on the anodes;

4. Large amounts of white flocculent matter precipitate in the artificial seawater.

All these physical phenomena influence the net corrosion behavior of the aluminum anodes. Some of these factors clearly tend to detract from the anodic reactions, but the

current supplied by the anodes tends to continue at a stable rate, as evidenced by the relatively constant level of galvanic current observed. It is of interest to determine how the galvanic current is able to be supplied under the apparently changing conditions related to the corrosion process. In order to pursue this question it is necessary to move to a consideration of more microscopic aspects of dissolution and corrosion product formation.

Prior to presenting a chronology of corrosive attack for each aluminum sacrificial anode alloy, some general microscopic features will be reviewed. Figures 37-39 indicate the general trends representative of each alloy after twenty-four-hour immersions and show that, on the microscale, anodic attack is realized by processes of crystalline dissolution. This is the case for all the alloys, although the details of the dissolution morphology differ for each one.

Galvalum®I, Figure 37, shows dissolution from the edges of the specimen inward. The process undercuts the general surface film to a slight extent as it progresses. A feature noticeable in Figure 37 is the obvious crystallographic nature of the dissolution surface morphology. This crystalline pattern was apparent in all the Galvalum®I specimens studied.

Figure 38 illustrates the typical microscopic corrosion features observed for Reynode®II. Various degrees of anodic dissolution are evident within the region. The grain at the bottom left, for instance, has been preferentially etched as evidenced by comparing its apparent depth to that of the grain

in the middle of the micrograph. A characteristic morphological feature of the Reynode®II dissolution surface evident in Figure 38, is the "peak" (possibly octahedral in form) structure in the center grain.

Microscopic characteristics of the corrosive attack of KA-90® alloy are shown in Figure 39. In this case, also, there is evidence of crystallographic dissolution. Faceting is seen within the various grains, with the orientation of the facets different in each grain, indicative of course, of the different aspects that the grains present at the planar surface. A tendency to intergranular corrosion (IGC) is also noticed in KA-90® (Figure 39). IGC is also evidenced when physically inspecting KA-90® specimens after immersion tests, at which time the specimen surfaces are observed to be loosely granular and tend to crumble.

2. Chronology and Trends of the Corrosion Mechanism of the Galvalum®I Aluminum Sacrificial Anode Alloy

Figures 40 through 64 represent the surface morphology of Galvalum®I samples after timed galvanic immersion tests.

After fifteen-minutes immersion (Figures 40 and 41), it is already noticeable that anodic attack on Galvalum®I is starting at the specimen edges. Dissolution apparently starts as an edge-located pitting phenomenon and then spreads along the edge and into the specimen surface. In Figure 40 it can be seen that dissolution is rapid along the edge of the specimen. The corrosive attack simultaneously, but somewhat more slowly, proceeds inward along the surface of the specimen,

as seen in Figure 47, which illustrates an inward advance of ca 1 mm in four hours. Taking this general corrosive behavior one step further, it was noticed that the front face (meaning the surface of the aluminum anode specimen which faced the steel cathode during the immersion tests) of the fourteen-day immersion specimen of Galvalum®I, Figure 7, was not corrosively attacked over more than one-third of the surface. This shows that the general corrosion behavior of Galvalum®I involves localization of attack in slowly expanding dissolution cavities, yielding a great increase in the net surface area available. This mechanism allows the anode to maintain more easily a current flow to the cathode that is sufficient for cathodic protection. Figure 56 further illustrates this behavior.

Galvalum®I specimens exposed for short times (fifteen and thirty minutes) do not display any distinct crystalline dissolution patterns (Figures 40 and 41). At these short times, an unstructured crust covers corroded areas. But after a one-hour immersion, the crust is no longer evident. The specimens exhibit a distinct corrosion pattern on the dissolution surface, now relatively uncovered by corrosion product (Figures 42,43). The term "herringbone" will be applied to this crystallographic dissolution pattern; this surface morphology consists of a set of hillocks of base metal extending outward from a central ridge, appearing much like ribs extending outward from the spine of a fish skeleton. Figure 43 particularly illustrates this herringbone pattern and is a magnified view of the grain located at the left center of Figure 42. The white "puffs" at the peaks

of the backbone are corrosion product, while the hillocks, or rib-bones, extending from the central spine are base metal. In between the individual herringbone patterns are flat, featureless valleys of more uniform metal dissolution. The rib-bones in such patterns are typically 2-3 μm in width and are separated by troughs that are 1-2 μm in width; these dimensions do not vary with immersion time.

The morphological and dimensional consistency of these herringbone patterns reflects the particular dissolution mechanism of the Galvalum®I sacrificial aluminum anode alloy. To describe the dissolution mechanism in more detail, the crystallography of the face-centered-cubic (FCC) aluminum matrix must be considered.

The atomic arrangement at a planar surface of a polycrystalline solid varies with grain orientation relative to the direction in which the specimen is cut [53]. In many crystal structures, including FCC, certain planes tend to be preferentially etched, leaving other planes geometrically evident [54]. Since the close-packed planes of a crystal have the greatest number of atomic bonds distributed in them [53], they tend to be the faces revealed by etching. Close-packed planes have the highest surface energy [53]; and if this surface energy is plotted as a function of crystal-planar orientation (Wulff Plot), there is maximum energy in the direction of close-packing [55]. For FCC crystals the close-packed planes are {111} and the close-packed directions are ⟨110⟩.

If aluminum is placed in an environment that will preferentially etch the non-close-packed planes, why is it that more base metal structure than just {111} planes remains after the etch? Vermilyea [53] reports that the {111} plane of an FCC crystal lattice maintains a constant potential and remains unchanged during an etch, but the potentials of the other (non-close-packed) planes drift and approach that of the {111}. This leads to the other planes being etched at a rapid rate until they approach the configuration of a {111} plane, and then the etching mechanism slows. From this process, distinct hills and valleys are created, and microscopically the entire surface of the crystal will be bounded by close-packed planes [53].

The grain boundary configuration shown at the upper right of Figure 46 clearly illustrates a "step structure" created by preferential etching. The herringbone patterns, like those in Figure 43, appear similar to hills and valleys. It is conjectured that the rib-bones are made up of close-packed {111} planes of the aluminum, and the preferentially etched areas between the rib-bones are planes of less dense atomic packing. This idea is supported by the fact that the width of the rib-bones does not change with immersion time. Figures 44,45,52 and 53 illustrate the constant dimensionality of the herringbone pattern. As the corrosion process continues, the rib-bones of the herringbone structure show some etching; but at the same time, the valleys between the rib-bones deepen, thereby preserving the herringbone surface morphology.

Figures 44,45 and 47 further illustrate the typical herringbone patterns shown by Galvalum®I and also give evidence that grain boundaries are undercut, i.e., experience some slight increase in the degree of dissolution. As time of immersion increases, some penetration appears along certain boundaries, and outer grain surfaces become revealed due to differences in dissolution rates for different grain aspects. It should be noted that it is not considered that the grain boundaries are being corrosively etched by a classical "intergranular corrosion" mechanism; the attack here is much more subtle in nature. Figure 45 shows the junction of three grains (seen in the center of Figure 44) that display differing dissolution rates. Figure 52 clearly illustrates how the differing dissolution rates can create voids between grains. It is possible that these areas may contain a slightly higher concentration of alloying constituents that lead to somewhat enhanced dissolution rate at the boundaries as compared to the central grains.

Figure 49 shows an isolated dissolution cavity on the broad surface of a Galvalum®I specimen, a rare observation for this alloy. Figures 50 and 51 are magnified views of the structure within the cavity, showing the same herringbone dissolution pattern described earlier.

Figures 48 and 57 illustrate the general appearance of the "uncorroded" surfaces of specimens exposed four- and forty-eight hours, respectively. There is evidence of a continuous (but cracked) film (It is quite possible that the

film cracked during drying.) and small outcroppings or clusters of corrosion product. This film is believed to be a complex aluminum oxide which covered and protected part of the surface of the specimens. The corrosion product clusters were tenacious, in that they did not come off the specimens when the specimens were removed from the artificial seawater immersion and rinsed with distilled water.

As immersion time for Galvalum®I specimens was increased, the amount of corrosion product that deposited on the spines of the herringbones increased to some extent (Figures 45,50,53,54 and 55). The corrosion product localizes on the spines in clusters and appears to be fine crystallites (Recall that no x-ray diffraction peaks were produced by the precipitate matter in the seawater.). An attempt to determine the elemental makeup of the corrosion product was made using the PGT-1000 x-ray fluorescence analyzer. A seventy-two-hour immersion specimen was used for the PGT-1000 analysis; it had not been gold coated. Figure 58 shows the specific area analyzed, and Figure 59 shows the PGT-1000 x-ray spectrum of this area. In addition to the intense aluminum peak, there were peaks (from left to right in Figure 59) showing the presence of zinc, sodium, aluminum, sulfur, potassium and iron.

Figure 60 shows the distribution of sulfur, which is located within the cruciformed area of corrosion product shown in Figure 58. Other dot mappings (not illustrated) show that sodium and chloride are also present in the corrosion product. Although the exact stoichiometry of the corrosion product is

not known, it can be reasoned from the data that sulfates and sodium compounds are in the corrosion product.

The surface structure for Galvalum®I immersed ninety-six hours is illustrated by Figures 61,62 and 63. Figures 61 and 62 show continued formation of the herringbone pattern (The ribs remain 3-4 μm in width, and the valleys between the spine crests are deeper.) and larger amounts of corrosion product on the central spine. Figure 62 shows that the corrosion process continues to undercut unattacked surface areas of the specimen. This observation points up the fact that once the general aluminum oxide passivating film is broken and a dissolution region established, the passivating film is no longer a significant factor.

Some photographs are included here because they illustrate findings that are atypical of the general trends. Figure 62 shows (near the center) a unique protuberance within a dissolution region, and a magnified image of it is shown in Figure 63. Similar features were seen on other specimens, but this was the most dramatic and also the only one noticed within a dissolution region. The protuberance shown is approximately 50 μm wide and 50 μm in height. It is reasoned that features of this sort correspond to isolated "true pits" and that the mechanism of formation is akin to what Kano [56] termed "gaseous arch formation". Kano stated that when a gaseous element, liquid or small piece of solid is formed in the small holes (pits) of a protective film (aluminum oxide), the pressures of these substances may increase

and lead to formation of arches of these materials across the opening of the holes (pits). The shapes of the arches are different, depending on the material, environment and current. The present observations are of solid corrosion product being forced out of pits by an internal force, much like toothpaste from a tube.

Figure 64 shows the typical grain structure of the Galvalum®I specimens. There is very little evidence of localized attack that might be associated with this base metal microstructure, such as second phases or compositional segregation. It should be noted that Figure 64 shows large grains in the center of a chill-cast and cored "pencil". These chill-cast pencils were machined to make the specimens used in the immersion tests; and the outer areas, or edges, did have smaller grains as evidenced in some SEM photographs (Figures 42 and 44). The center grains of the chill-cast pencils (Figure 64) are larger than 1.2 mm, while the grains in the edge of the immersion specimens are on the order of 0.2 mm in diameter.

It is possible, but not confirmed by this work, that the observed discrete herringbone dissolution patterns are related to some base metal microstructural feature, perhaps a fine-scale dendritic pattern. Since the herringbone features are not observed on the dissolution surface of other alloys of similar nominal composition, a base metal microstructural origin seems logical.

When the Galvalum®I microscopic data described in this section are compared with the features shown by the other alloys studied, very different appearances are seen.

3. Chronology and Trends of the Corrosion Mechanism of the Reynode®II Aluminum Sacrificial Anode Alloy

Figures 65 through 89 represent the surface structures of Reynode®II observed in this study. Reynode®II exhibited its own characteristic dissolution patterns and features, quite different from those exhibited by Galvalum®I, although these alloys are similar in constituency. Reynode®II samples typically exhibited:

(1) rapid pit formation, followed by

(2) elongation (downward on vertical faces) into local dissolution cavities (wormpitting), and

(3) within the dissolution cavities, on a fine-scale, variable dissolution rates of separate grains in a given sample, and

(4) what appears to be "peaked" octahedral [57] form, a prevalent microscale feature on grain surfaces within the local dissolution sites (wormpits).

Figure 65 illustrates rapid dissolution pit formation on Reynode®II after fifteen-minute exposure; the large pit in this field is 225 μm in diameter, formed while the galvanic couple was producing an average 3mA/cm^2 current density. A distinction between Reynode®II and Galvalum®I is that pits tend to form on the faces of Reynode®II specimens, whereas they were preferentially located on the edges of Galvalum®I

specimens. Figure 66 is a magnified view of the dissolution cavity in Figure 65 and shows that characteristic corrosion patterns form on Reynode®II within fifteen minutes. A significant feature of Figure 66 is the dissolution undercutting of the unattacked surface of the anode, also illustrated in Figures 67,71 and 84. These observations lead to the conclusion that Reynode®II obtains the transpassive condition during polarization more easily than Galvalum®I (See polarization curves, Figures 27,28,29 and 30.), thereby forming an array of pits on its surface. Enlargement of these initial pits into elongated dissolution cavities is facilitated by undercutting of the passivating film on the surface of the specimens.

Figures 65,67,70,75,78,80,82 and 84 illustrate the chronology of dissolution cavity growth for Reynode®II. The dissolution cavities grow and worm along the surface of the specimens, a growth characteristic evident in Figures 80 and 84. The wormpits shown in Figure 84 grow vertically down the anode surface during exposure, with much slower widening of the cavity. It may be that a gravity effect was letting a corrosion product run out of a local dissolution site, down the vertical face of the specimen, and therefore aiding the corrosive attack. It is not believed that the machine marks have much to do with this orientation of the dissolution cavities, although sometimes the elongated cavities are parallel to machine marks. At higher magnifications, the inner surface of the "pits" show unique dissolution morphologies

(e.g., Figures 70 and 75). Base metal grains, and grain boundaries, are clearly distinguished, and some grains show distinct parallel facets. Some grains are without any particular characteristic, while others have grain boundary-located dissolution surface structures that are similar to Galvalum®I's herringbones (Figure 85). Within many grains are characteristic dense clusters of peaks or octahedra. The specific shape of these peaks depends on the grain aspect, and it is not believed that they are a perfect octahedral form. Also, the peaks do not always appear rounded. Therefore, they are referred to here as "peaks".

Figures 68 and 69 are magnified views of Figure 67. The white crested structure that runs diagonally across Figure 68 corresponds to a base metal grain boundary. The projection of this grain boundary ridge above dissolved inner grains is typical and the opposite of the tendency of Galvalum®I, which exhibited a slight degree of grain boundary grooving. Note the array of peaks to the left of the boundary in Figure 68. These peaks, also illustrated by Figure 69, are 2-4 μm in height and width and appear in a regular, uniformly-spaced array.

Most crystals develop faces of simple orientation when electrolytically etched, and the final face is independent of the orientation of the face initially exposed to the solution [58]. The remaining faces are clearly the most slowly dissolved and most often close-packed [53,54,58]. It is evident from Figure 69 that preferential etching attacks the base metal in this manner and works to develop the peaks while forming the planar surface in the center of the Figure.

Although both Galvalum®I and Reynode®II form distinct crystallographic dissolution surface structures, there is a significant difference between the dissolution morphologies. The question is why, since these two alloys have similar composition, specimens from both alloys were made in the same manner, and all testing was accomplished with a standard procedure. The only known difference between Galvalum®I and Reynode®II is that Reynode®II is heat-treated after casting. This solution heat treatment apparently allows a redistribution of alloying elements in such a way that when the metal is corroded in a saline environment, it appears much different from Galvalum®I, although the same basic corrosive mechanisms and governing factors exist. The exact mechanism which leads to the observed differences in etched surface morphology is not known at this time.

Figure 89 is a base metal micrograph of Reynode®II. This micrograph of Reynode®II exhibits a large single grain size, over 1.2 mm, comparable to Galvalum®I (Figure 64), but also shows dendritic structure within the grains.

Figures 77 and 81 also illustrate the distinct peak (octahedral) formation, for four- and twenty-four-hour immersions respectively. Sometimes these features have a less distinct appearance, as seen in Figures 76 and 79, where they appear rounded and worn. Since these rounded features are 2-4 μm in diameter (same as the distinct peaks) and are regularly arrayed, it is supposed that these are in fact evidence of the same basic dissolution morphology.

Figures 71 and 79 give striking evidence of the crystal orientation-dependence of dissolution in Reynode®II. The topological relief seen in Figure 71 reflects the fact that each of the eight grains in the field had a different corrosion rate. There is very little corrosion product present on any of the dissolved surface, a feature in common with the Galvalum®I alloy and undoubtedly related to the mercury content of these alloys [12].

Another common dissolution morphology seen for Reynode®II is illustrated by Figures 73 and 85, where the surface dissolution topology appears striated, meaning grooved or channeled. The striations do not cross grain boundaries, and are approximately parallel to each other within a given grain. This pattern is probably a manifestation of preferential crystallographic dissolution which comes about when certain grain aspects are presented to the electrolyte.

A less-frequently observed, but typical, feature seen on Reynode®II specimens, is shown in Figure 83; a protuberance, similar to that occasionally seen on Galvalum®I, extends from the surface of the forty-eight-hour immersion specimen. Upon close examination it appears that the projection was extruded from below the surface of the metal, i.e., from a "true" pit. Notice the cracked crust around the base of the protuberance. Again, the mechanism of formation of these features is considered to be similar to that described by Kano in his "Gaseous Arch Theory" [56].

Figures 86,87 and 88 illustrate an attempt to characterize the chemical makeup of the surface corrosion product on Reynode®II. Figure 87 is an x-ray distribution image (dot map) of aluminum. It illustrates that there is a distinct difference between the aluminum concentration in the base metal and the corrosion product. Figure 88 is the x-ray spectrum of the field seen in Figure 86, and the predominate peaks are (from the left) aluminum, sulfur and chlorine.

In summary, the predominant features of the corrosion morphology of Reynode®II reflect a preferred crystallographic etching, with shapes resulting from the various dissolution rates of close-packed and non-close-packed crystal planes. The commonality between Galvalum®I and Reynode®II is that both materials exhibit initial pitting which then expands into local dissolution sites. However, the attack on Galvalum®I concentrates initially at the edges of the specimens, while Reynode®II was attacked primarily on the broad face surfaces. Also, both Galvalum®I and Reynode®II expand their dissolution sites by undermining the general oxide layer on the surface of the specimens.

4. Chronology and Trends of the Corrosion Mechanism of the KA-90® Aluminum Sacrificial Anode Alloy

Figures 90 through 106 are representative photographs of specimens used in the timed-immersion studies of KA-90®. Predominate features of the corrosive attack of KA-90®include:

(1) rapid, general, true pitting distributed over the

entire anode surface, formed not only at the beginning of the immersions, but during the entire immersion cycle,

(2) intergranular corrosion, and

(3) the presence of a heavy deposit of corrosion product on the specimen surface.

Pitting features, seen in Figures 91,93,96 and 100, may be correlated to the alloy's high initial galvanic current. The high starting current breaks down the oxide film and allows pitting to begin [50]. The attainment of transpassive polarization behavior by KA-90® after relatively low polarization (See polarization curves, Figures 31 and 32.) creates a situation that allows the cathodic branch of the HY-80 polarization curve to intersect the transpassive region of the KA-90® anodic polarization curve at relatively high current density. Thus, when KA-90® is coupled to HY-80 steel and immersed in artificial seawater, the KA-90® will pit.

Another item of interest is: Why does KA-90® pit at a given location? It is hypothesized (after Keir, et. al. [51]) that KA-90® pits where there is a concentration of tin, which breaks down the resistance of the aluminum oxide film. If the tin concentrations were located at grain boundaries, the pit formed at this location could be the beginning of intergranular corrosion. A sketch of the KA-90® microstructure as seen under the optical microscope is shown in Figure 106.

The patterns seen in Figure 106 were noticed over the surface of the specimen. There appeared to be a subtle (not photographable) precipitate-free zone adjacent to many grain

boundaries and inclusion particles distributed throughout the grains, particularly along the grain boundaries and at "triple" points. Also, there were many fine precipitates distributed throughout the base metal.

The KA-90® miscrostructure shows remarkable correlation with microphotographs presented by Keir, et. al., in Ref. [51], for an Al- 0.08% tin alloy; KA-90 has a 0.1% tin content. It is reasoned that concentrations of tin, in conjunction with the high starting current and polarization behavior, create the necessary conditions for pitting of the KA-90® aluminum sacrificial anode alloy.

The pits seen in Figures 90 and 91 are approximately 25-30 μm in diameter after fifteen minutes of galvanic action. As the immersion time increases, pitting action continues, and more pits are generated (Figures 93,96 and 100). This nucleation of more pits is in contrast to the tendency of the two other alloys studied, which are mercury-bearing.

Figures 90,95 and 97 illustrate dissolution undermining of the unattacked surface of the anode. Figure 97 is particularly descriptive of this behavior, where the undermined surfaces of the anode can be seen hanging over the edges of a large pit. This mode of dissolution obviously avoids any problem of passivation created by a general surface oxide film.

Figures 92,94 and 104 show that significant amounts of corrosion product accumulate on KA-90® specimens within thirty minutes after immersion. It is believed that this corrosion product accumulation does not constitute passivation, i.e.,

does not impair the anode's ability to supply current and cathodically protect. It is reasoned that these specimen anodes become covered with corrosion product because they do not have to provide as much galvanic current as the Galvalum®I and Reynode®II anodes do to protect the cathodes. This formation of corrosion product on KA-90® anodes is due to the heavier-than-average calcareous deposits which form on cathodes coupled to KA-90® anodes. These calcareous deposits reduce the exposed cathode area requiring protection. In order to investigate further this hypothesis, it would be useful to study the behavior of KA-90® (and other alloys) as a function of cathode-to-anode area ratio. An investigation of this type would allow the researcher to observe the extent of corrosion product buildup on the anodes.

Figures 101,102 and 103 illustrate intergranular corrosion of KA-90® alloy. In the bottom right corner of Figure 101 and in the center of Figure 102 are large openings formed at base metal triple points. These dissolved openings sometimes progress completely between and around grains, and sometimes grains become covered by smooth, egg-shell-like capsules, as in Figure 103.

A grain dissolution pattern in KA-90® anodes is seen in Figures 101,102 and 103. As argued earlier, it is reasoned that the channels and grooves seen on the exposed dissolution surfaces of grains are created by a preferential etch of the non-close-packed planes of the aluminum FCC crystal lattice [51,53-55,58,59].

Another feature is seen in Figures 98 and 99, which illustrate curious and perfectly hemispherical "pods". These pods are much more prevalent on KA-90® than the protuberances found on Galvalum®I and Reynode®II specimens, to which they are the equivalent feature for KA-90®. The hemispheres are on the order of 50 μm in diameter, are semi-transparent, and appear to be fragile and easily fractured (Figure 99). The geometry of the "pods" appears to coincide more closely with Kano's "Gaseous Arch Theory" [56] than the protuberances on Galvalum®I and Reynode®II. The perfect hemispherical dome shape indicates that they clearly have been "blown up" by gas pressures from within pits.

Figure 105 is an x-ray spectrum of the corrosion product on the seventy-two-hour immersion specimen. From the left, the elemental peaks of the spectrum are oxygen, zinc, aluminum, sulfur, chlorine and zinc. The zinc peaks are prevalent because the KA-90® alloy contans 6.0-7.4% zinc. A dot mapping of the zinc indicates that its location is predominately in the base metal and not in the corrosion product.

VI. SUMMARY

The following is an itemized summary of the results and conclusions of this research.

(1) The commercial aluminum sacrificial anode alloys, Galvalum®I, Reynode®II and KA-90®, show similar galvanic current characteristics as a function of time. In these experiments, it was seen that each alloy initially exhibits a relatively high current density (8.4 mA per cm^2 for KA-90®, 4.5 mA per cm^2 for Galvalum®I, and 7.4 mA per cm^2 for Reynode®II) which then falls to a stable level of approximately 0.8 mA per cm^2 for each alloy. The current density is reduced to this stable level because the calcareous deposits which form on the protected cathodes effectively reduce the surface area of the cathodes and, therefore, reduce the anodic current output required for adequate cathodic protection.

The cathode protected by KA-90® had the greatest amount of calcareous deposit on it, and the KA-90® anodes became covered with a corrosion product (Galvalum®I and Reynode®II did not.). It is believed that the corrosion product on the KA-90® anodes does not constitute passivation, i.e., does not impair the anode's ability to supply galvanic current and cathodically protect. In order to investigate further this hypothesis, it would be useful to study the behavior of KA-90® (and other alloys) as a function of cathode-to-anode area ratio, and observe the extent to which the anodes become encrusted with corrosion product.

(2) It is obvious that each anode material adequately protected the HY-80 steel to which it was coupled for the duration of the synthetic seawater immersion tests used in this research. This protection is evidenced by the continuing provision of galvanic current and by the calcareous deposits formed on the HY-80 cathodes [47].

(3) Macroscopic corrosion patterns exhibited by each alloy are different, related to compositional and thermal history variables of the alloys. For Galvalum®I, which was chill-cast and not heat-treated, the distribution of dissolution sites over the samples shows greater attack at the edges of the specimens, i.e., there is greater sensitivity to geometric effects on potential distribution for this alloy. Reynode®II, which is cast, heat-treated, and then slow cooled [52], shows somewhat more general corrosive attack, in that more local dissolution sites are formed on the broad surfaces of the anode. Although Reynode®II does have more local dissolution sites than Galvalum®I, Reynode®II's heat treatment apparently does not really homogenize the alloy constituents because the dissolution sites are not as numerous as those on KA-90®and do not cover a significant area of the anode specimen's surface. Also, the microstructure of Reynode®II indicates that the alloy is still segregated. KA-90® is heat-treated to approximately 900°F in order to resolution tin and zinc and then water quenched [38]. It typically shows rapid pitting. The pits eventually expand to cover the entire specimen surfaces. It has been concluded that alloy composition relates to the pitting

mechanism exhibited by the KA-90® anode specimens. The presence of tin-precipitates in the base metal of this alloy creates favorable sites for the start of the pits.

(4) The small specimen coupons used in this study have been shown to represent fairly large anode samples, based on the fact that the same general corrosion patterns are seen over the surface of the small coupons as seen on full-size anodes [44]. This is considered important because it proves that small scale, inexpensive, laboratory tests are reliable for comparing aluminum anode alloys. It is also acknowledged that field tests, run over a lengthy period of time (one to two years), are essential to verify laboratory findings and predictions of the better alloys. Critical measurements such as weight loss and efficiency must be accurately known prior to full-scale production and marketing.

(5) It is this author's conclusion that the mercury-bearing anodes could be improved by establishing new alloying and heat-treating procedures so that they would exhibit a more even corrosive attack over their entire surface and, therefore, avoid the possibility of large sections falling off. It is logical to assume (and apparent from the behavior of KA-90®) that solution heat-treating does increase the uniformity of macroscopic corrosion patterns. However, it still cannot be stated exactly what factors may lead to severe localized corrosion attack of mercury-bearing alloys. Also, if localized attack is significantly accelerated by velocity effects (not yet researched), an anode might easily corrode around its support bars and fall from the structure it is protecting.

(6) It has been shown that the experimental procedures used in this research (galvanic current vs. time immersions, polarization data, scanning electron microscopy) provide correlative results with which a researcher can establish an anode alloy's corrosion behavior. For instance, KA-90®'s high initial galvanic current density and polarization behavior provide evidence that the alloy will exhibit a pitting attack. Photographs taken with the scanning electron microscope and macrophotographs of KA-90® provide physical evidence of pitting on KA-90® anodes. Polarization and galvanic current data obtained from Reynode® II anode specimens provide evidence that Reynode® II will exhibit more general dissolution than Galvalum® I and less general dissolution than KA-90®. Once again, the microphotography showed this to be the case.

(7) Scanning electron microscope examinations of the corroded surfaces of aluminum sacrificial anode specimens show that a combination of corrosion mechanisms is responsible for the dissolution morphology. Each type of alloy investigated evidences its own particular microscopic dissolution pattern, with certain distinct morphological features. The dissolution morphologies exhibited are all quite obviously crystallographic, related to the FCC crystal structure common to all the aluminum sacrificial anode alloys; but specific appearances are different.

(a) Galvalum® I exhibits a unique "herringbone" pattern. Even dissolution of each grain is apparent, with relatively small amounts of corrosion product present on the

spine of each herringbone, giving direct and convincing evidence that Galvalum®I alloy is not likely to passivate.

(b) Reynode®II shows a completely different dissolution morphology than Galvalum®I. This was not anticipated since these two alloys are almost identical in nominal composition. There are two general features of the dissolution patterns of the Reynode®II alloy: (1) the appearance of peaks formed by preferential etching (dissolution) of the FCC crystal structure, and (2) varied dissolution rates of different grains within a single dissolution cavity.

As with Galvalum®I, Reynode®II samples show only small amounts of corrosion product (macroscopically and microscopically) so that a passivation problem would not be anticipated for this alloy.

(c) KA-90® alloy specimens do not show microscopic dissolution patterns which are as distinct as the herringbones and peaks associated with Galvalum®I and Reynode®II alloys, respectively. There is, however, convincing evidence of intergranular corrosion on the microscopic scale; also physical attributes of the specimens (crumbling of the surface) indicate intergranular corrosion.

(8) Corrosion rates calculated from galvanic current data show quite good correlation with weight loss measurements. Also, the galvanic current data and potentiodynamic polarization data are reproducible and can be used to predict the relative corrosion rates of aluminum anode alloys when galvanically coupled to other metals.

(9) In the course of this research, effective procedures have been developed to acquire reproducible potentiodynamic polarization curves for aluminum sacrificial anode alloys.

(10) X-ray diffraction analyses of corrosion products carried out in this research were inconclusive. X-ray powder patterns were obtained in an attempt to identify the adherent corrosion product on the KA-90® anodes, calcareous deposits on the cathodes of galvanic couples, and a white flocculent precipitate which accumulated in the artificial seawater electrolyte.

X-ray diffraction patterns of the KA-90® corrosion product and the precipitate in the electrolyte were inconclusive, probably because these products were amorphous or of very fine particle size. X-ray diffraction patterns of the calcareous deposits on the cathodes produced peaks corresponding to calcium carbonate and a dihydrous calcium sulphate ($CaSO_4 \cdot 2H_2O$). The diffraction patterns produced from deposits on all cathodes were identical, irrespective of anode alloy.

(11) Microscopic pit features (hemispherical "pods" and protuberances) were evidenced. The hemispherical pods on the KA-90® anode specimens were more prevalent than the protuberances on the Galvalum®I and Reynode®II specimens. It is theorized that the pods are created when a thin layer of corrosion product (or possibly an oxide film) is deposited over a pit, and the hydrogen gas that is being generated within the pit creates sufficient pressure to "balloon" the

layer of corrosion product. The surface of the pods is not very thick (evidenced in Figure 99), and, therefore, it should not take significant pressure to cause the expansion of the pods. These pods relate to and confirm contemporary theories of pitting. The protuberances on Galvalum® I and Reynode® II specimens appear to begin within localized pits and are then extruded from the pits like toothpaste being forced out of a tube.

(12) Galvalum® I and Reynode® II have similar alloy constituency but very different microscopic corrosion dissolution patterns. The reasons for this difference was not established during this research. It can only be conjectured that the heat treatment of Reynode® II and its additional quantity of zinc are the prime factors creating the different microscopic dissolution characteristics. This contrast in behavior between two compositionally similar commercial anode alloys serves to point out that factors other than alloy composition can be of great importance in aluminum sacrificial anode alloys.

VII. RECOMMENDATIONS

The results of this study constitute the initial research on aluminum sacrificial anode alloys at the Naval Postgraduate School. It is firmly believed that additional research is warranted. It is recommended that future research concentrate on the following points:

1. It would be interesting to carry out velocity studies of the aluminum anodes that would closely simulate shipboard conditions. This study is justified because it will be three to four more years before all the surface ships have impressed-current cathodic protection systems, and it may be that some of the older ships will never receive the system.

2. It is currently planned to use aluminum sacrificial anodes to protect the internal areas of surface ships, i.e., bilges, tanks, voids, etc. A number of tests should be designed to simulate shipboard galvanic conditions; for example, anodes might be allowed to corrode under stagnant conditions. These tests should take into consideration that bilges and tanks are periodically drained, thereby removing the galvanic couple. In this regard, it would be important to establish the "restart" characteristics of all the mercury-bearing anodes.

3. An experimental program should be started to investigate the potentiodynamic polarization behavior of various aluminum anode alloys in conjunction with the variety of common shipboard materials. Some of the materials of

interest would be copper-nickel, nickel-copper, stainless steel and structural aluminum. From this type of research it could be seen if the aluminum anodes have any deleterious effect on these metals.

4. As previously concluded in this thesis, it appeared that heat-treated anode alloys had a more generally distributed corrosion pattern than a non-heat-treated alloy. It is suggested that further research be conducted to develop understanding of heat treatment effects on the corrosion behavior of aluminum sacrificial anode alloys.

5. All of the anode materials that were used for this thesis research are proprietary. The proposed military specification establishes compositional percentages for the alloy constituents. Therefore, it is believed that a continuing research project that could be accomplished at the Naval Postgraduate School would be related to alloy development of new and improved aluminum sacrificial anodes. These alloys could be manufactured and then tested on a small scale, such as in this thesis project, to determine if larger tests were necessary.

6. Baseline studies should be conducted on materials not thoroughly studied during the present thesis research and on new materials as they come on the market. Continued liaison with producers such as Dow Chemical, Kaiser Magnesium and Reynolds Metals is recommended.

7. Although it is a general problem in inorganic chemistry today, it is recommended that some investigation be

done in conjunction with the above recommendations to identify better the aluminum anode corrosion products. Identification of the products may be possible with a combination of x-ray diffraction and other spectroscopic instruments available at the Naval Postgraduate School.

TABLE I

Potentiodynamic Polarization Data for Freely Corroding Aluminum Sacrificial Anode Alloys.

Material		I_{corr} (μA)	i_{corr} (μA/cm^2)	E_{corr} (V-SCE)	R_{mpy}	R_{mmpy}	R_{mdd}
Galvalum® I:		32.5	7.97	-1.36	3.39	0.086	6.36
		35.0	8.58	-1.38	3.65	0.093	6.85
		33.0	8.09	-1.36	3.44	0.087	6.45
		36.0	8.83	-1.38	3.75	0.095	7.04
	$\bar{x}$	34.1	8.37	-1.37	3.56	0.090	6.68
	σ	1.65	0.41	0.01	0.17	0.004	0.32
Reynode® II:		18.0	4.42	-1.18	1.84	0.046	3.51
		17.0	4.17	-1.16	1.74	0.044	3.32
		15.0	3.68	-1.14	1.54	0.039	2.94
(Note 1)		78.0	19.13	-0.94	7.99	0.203	15.26
	$\bar{x}$	16.7	4.09	-1.16	1.71	0.043	3.26
	σ	1.5	0.38	0.02	0.15	0.004	0.29
KA-90®:		15.0	3.68	-1.24	1.49	0.038	2.93
		14.0	3.43	-1.19	1.39	0.035	2.74
		14.0	3.43	-1.19	1.39	0.035	2.74
		17.0	4.17	-1.15	1.69	0.043	3.33
	$\bar{x}$	15.0	3.68	-1.19	1.49	0.038	2.94
	σ	1.4	0.35	0.04	0.14	0.004	0.28

Note 1: The data obtained from the fourth potentiodynamic polarization run of Reynode® II was not included in the averages.

TABLE II

Predicted Corrosion Rates of Aluminum Sacrificial Anode Alloys Coupled to HY-80 Steel for Cathode to Anode Area Ratio of 5:4.

Material		I_{couple} (μA)	i_{couple} (μA/cm^2)	E_{couple} (V-SCE)	R_{mpy}	R_{mmpy}	R_{mdd}
Galvalum® I:		127.0	31.2	-0.93	13.5	0.34	25.3
		240.0	58.9	-0.94	25.5	0.65	47.8
		265.0	65.0	-0.95	28.2	0.72	52.9
		265.0	65.0	-0.95	28.2	0.72	52.9
	$\bar{x}$	224.0	55.0	-0.94	23.8	0.61	44.7
	σ	66.0	16.1	0.01	7.0	0.18	13.2
Reynode® II:		200.0	49.1	-0.94	20.9	0.53	39.9
		300.0	73.6	-0.96	31.3	0.80	59.8
		130.0	31.9	-0.93	13.6	0.35	26.0
	$\bar{x}$	210.0	51.5	-0.94	21.9	0.56	41.9
	σ	85.0	21.0	0.02	8.9	0.23	17.0
KA-90®:		1220.0	299.2	-1.00	123.5	3.14	243.4
		1700.0	416.9	-1.20	172.1	4.37	339.2
		960.0	235.5	-0.99	97.2	2.47	191.6
		2500.0	613.2	-1.40	253.1	6.43	498.9
	$\bar{x}$	1595.0	391.2	-1.20	161.5	4.10	318.3
	σ	680.0	166.0	0.20	68.5	1.74	135.1

TABLE III

Predicted Corrosion Rates of Aluminum Sacrificial Anode Alloys Coupled to HY-80 Steel for Cathode to Anode Area Ratio of 27:1

Material		I_{couple} (μA)	I_{couple} (μA/cm²)	E_{couple} (V-SCE)	R_{mpy}	R_{mmpy}	R_{mdd}
Galvalum® I:		1000.0	245.3	-0.92	106.4	2.7	199.6
		1000.0	245.3	-0.92	106.4	2.7	199.6
		600.0	147.2	-0.86	63.8	1.6	119.7
		700.0	171.7	-0.90	74.5	1.9	139.8
	$\bar{x}$	825.0	202.4	-0.90	87.8	2.2	164.7
	σ	206.1	50.6	0.02	21.9	0.6	41.2
Reynode® II:		800.0	196.2	-0.91	83.6	2.1	159.7
		1400.0	343.4	-0.92	146.3	3.7	279.4
		700.0	171.7	-0.91	73.2	1.9	139.8
	$\bar{x}$	966.7	237.1	-0.91	101.0	2.6	193.0
	σ	378.6	92.8	0.01	39.5	1.0	75.5
KA-90®:		9000.0	2207.5	-0.96	911.3	23.1	1796.2
		22500.0	5518.8	-1.00	2278.3	57.9	4490.7
		9000.0	2207.5	-0.95	911.3	23.1	1796.2
		17000.0	4169.7	-0.98	1721.4	43.7	3393.0
	$\bar{x}$	14375.0	3525.9	-0.97	1455.6	36.9	2869.0
	σ	6600.2	1618.9	0.02	668.3	17.0	1317.4

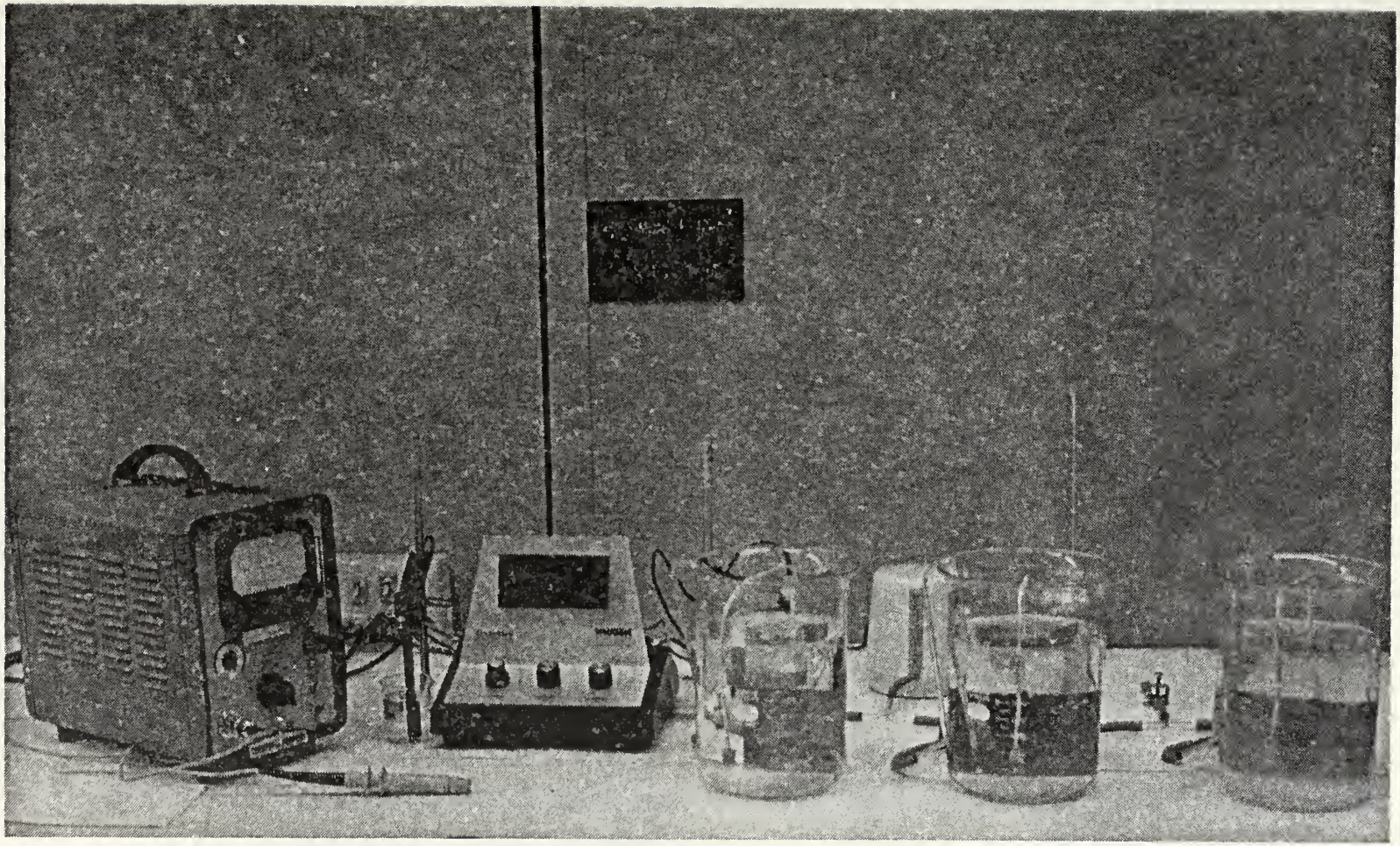

Figure 1

Apparatus used for galvanic current vs. time experiments

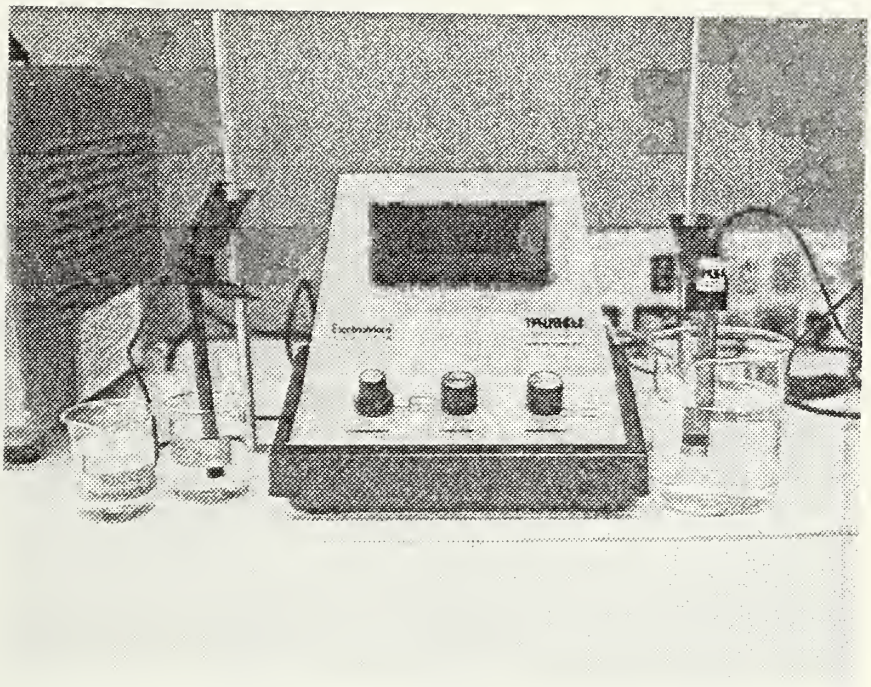

Figure 2

Markson Electromark® analyzer

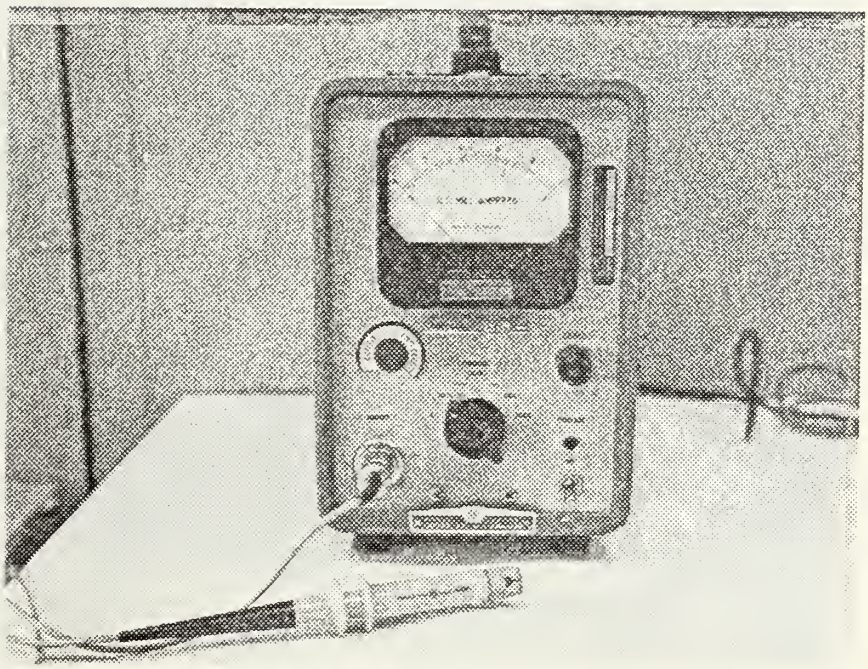

Figure 3

Hewlett-Packard Model 428-A
clip-on D.C. milliammeter

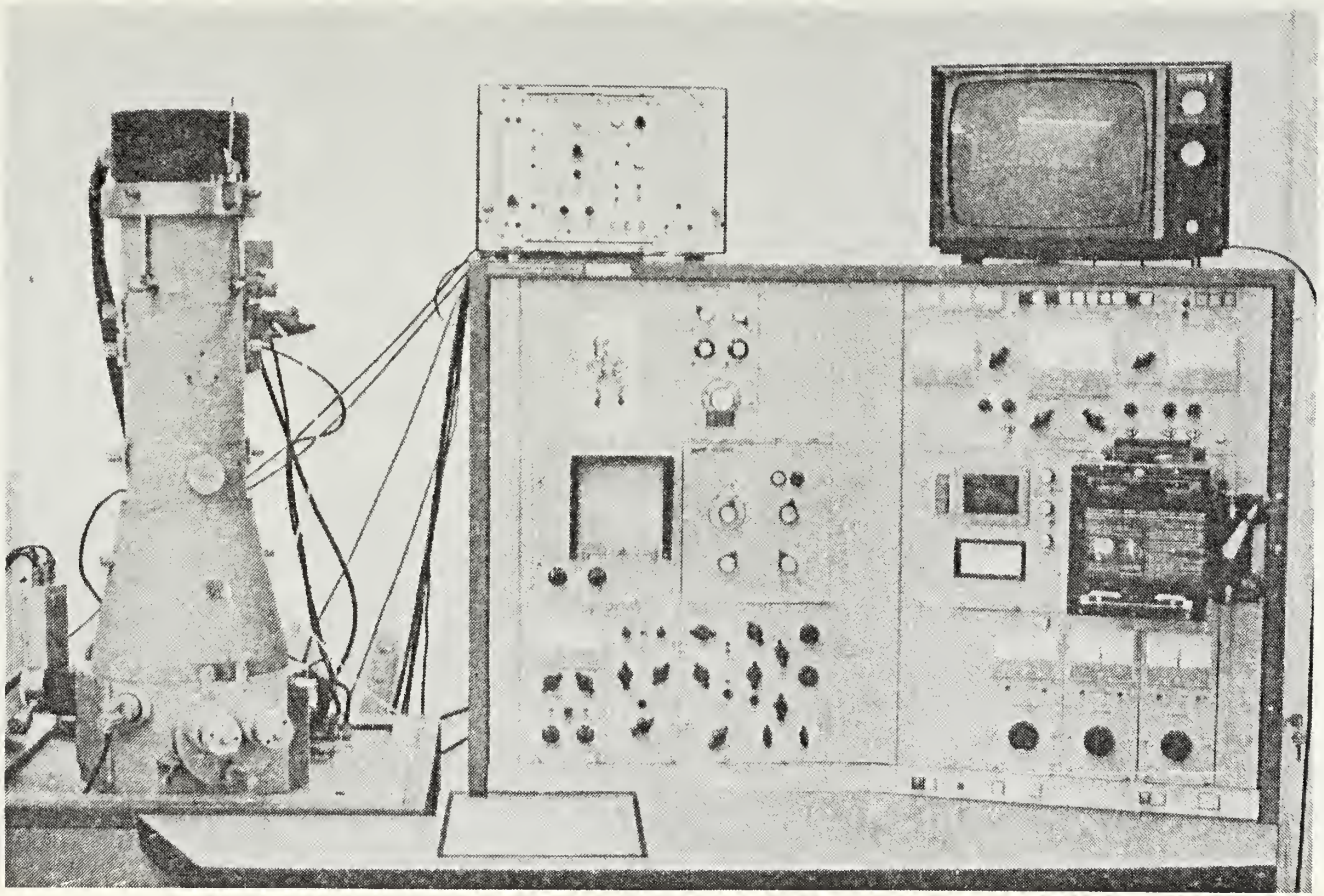

Figure 4

Cambridge Stereoscan S4-10 scanning electron microscope

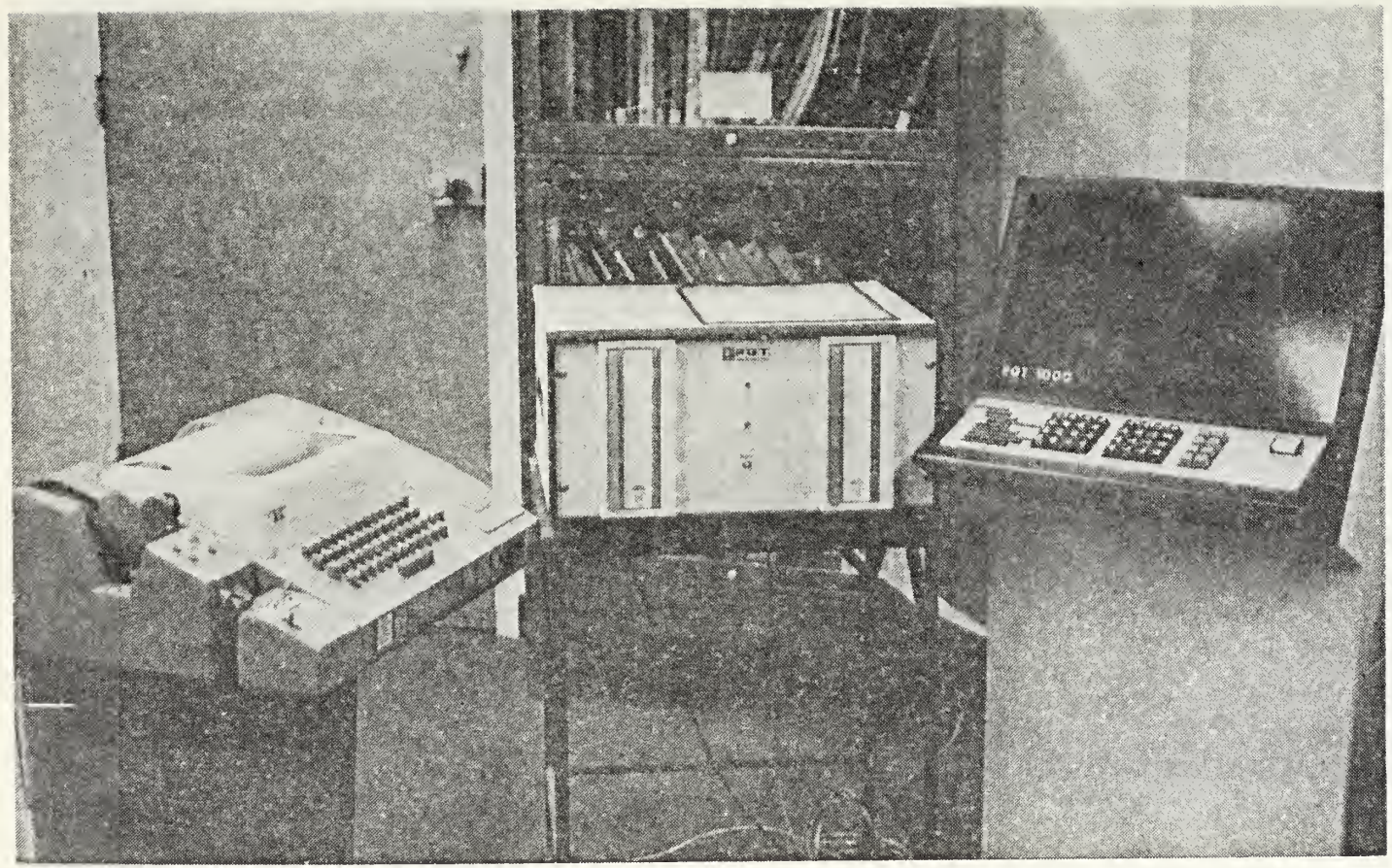

Figure 5

Princeton Gamma Tech (PGT-1000) X-ray fluorescence analyzer

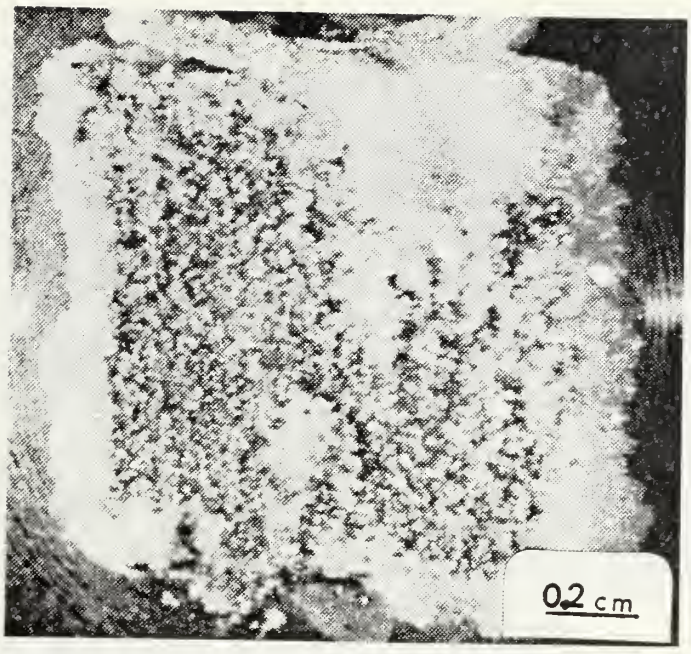

Figure 6

MIL-SPEC Zinc anode after fourteen-day immersion test

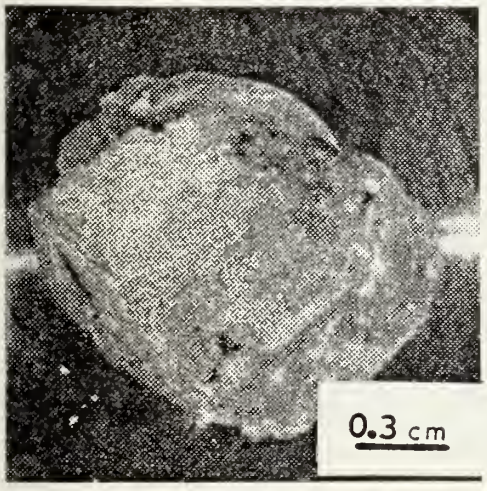

Figure 7

Galvalum® I anode after fourteen-day immersion test

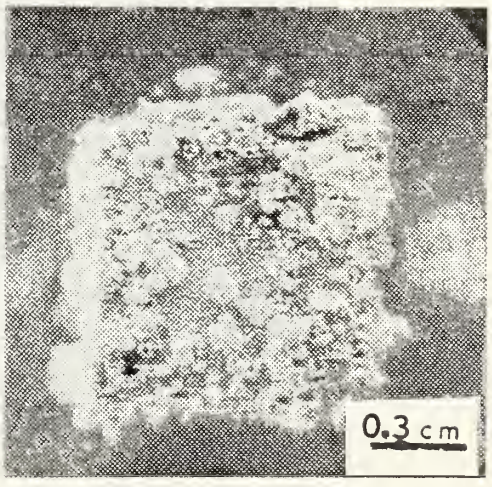

Figure 8

Galvalum® II anode after fourteen-day immersion test

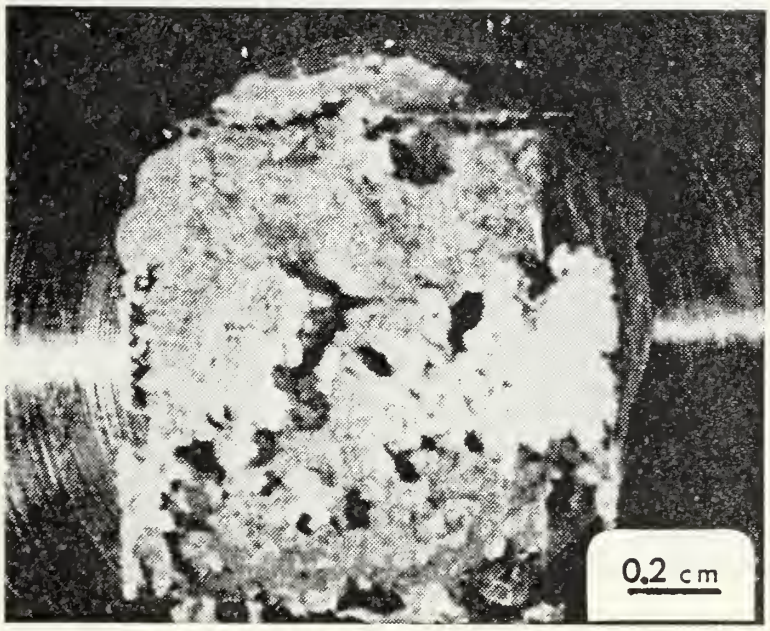

Figure 9

Galvalum® III anode after fourteen-day immersion test

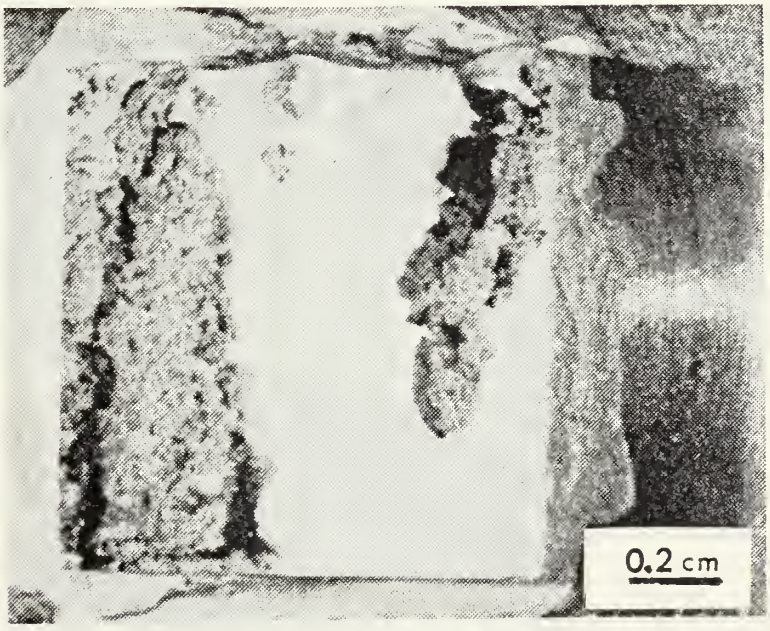

Figure 10

Reynode® II anode after fourteen-day immersion test

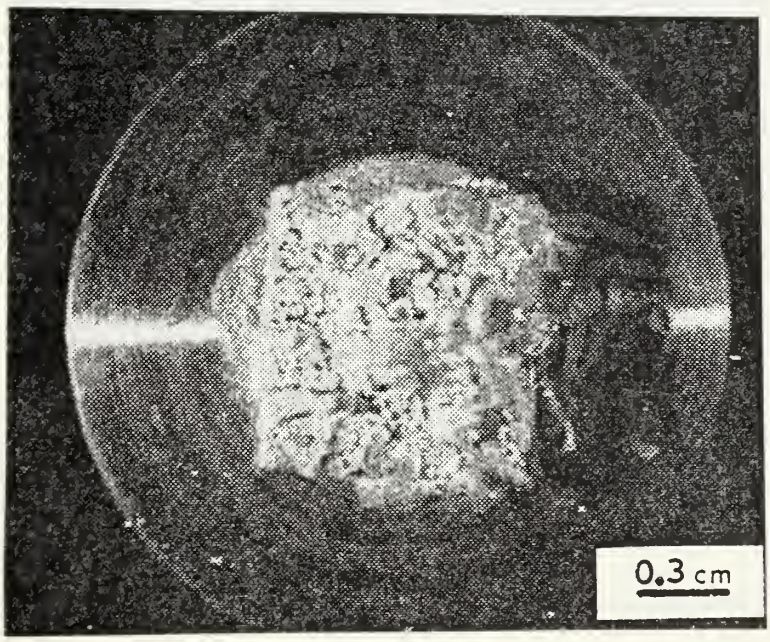

Figure 11

KA-90® anode after fourteen-day immersion test

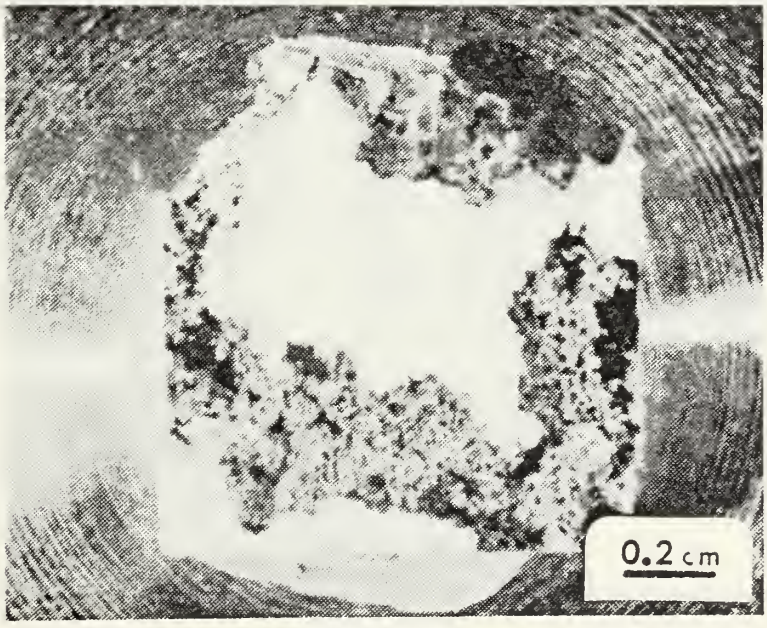

Figure 12

KA-95® anode after fourteen-day immersion test

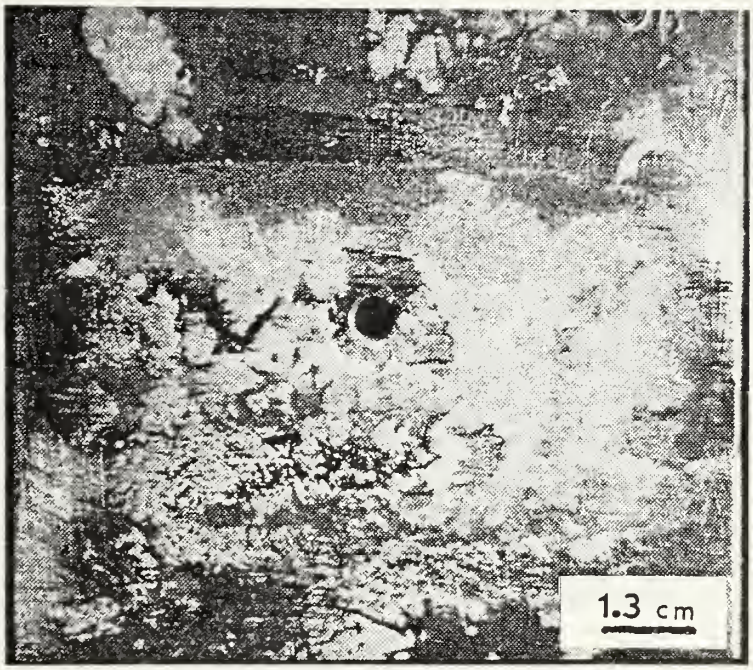

Figure 13

MIL-SPEC Zinc - protected cathode after fourteen-day immersion test

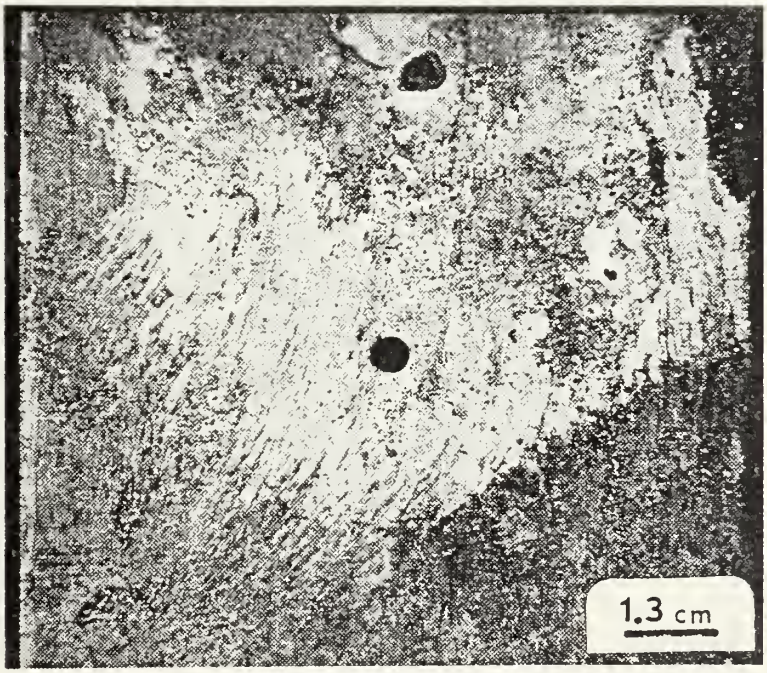

Figure 14

Galvalum®I - protected cathode after fourteen-day immersion test

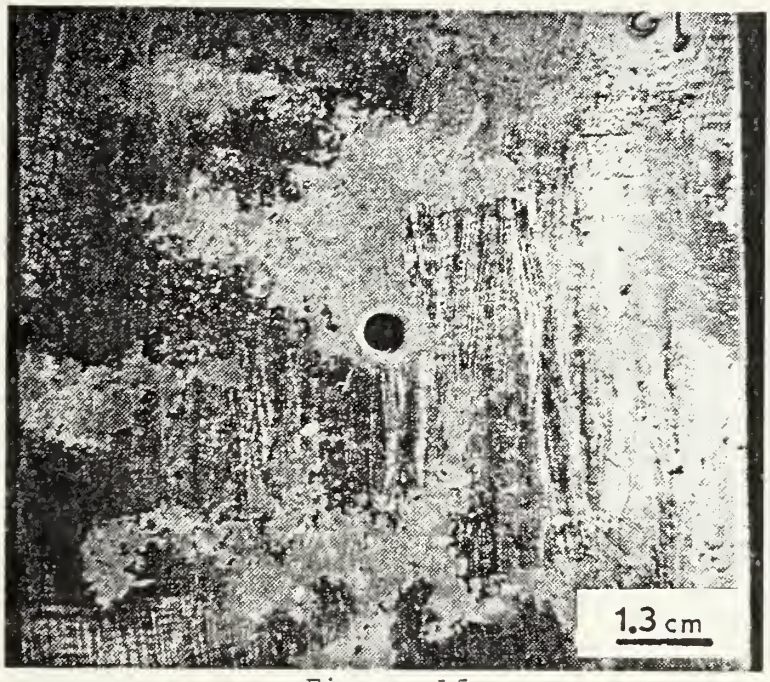

Figure 15

Galvalum® II - protected cathode after fourteen-day immersion test

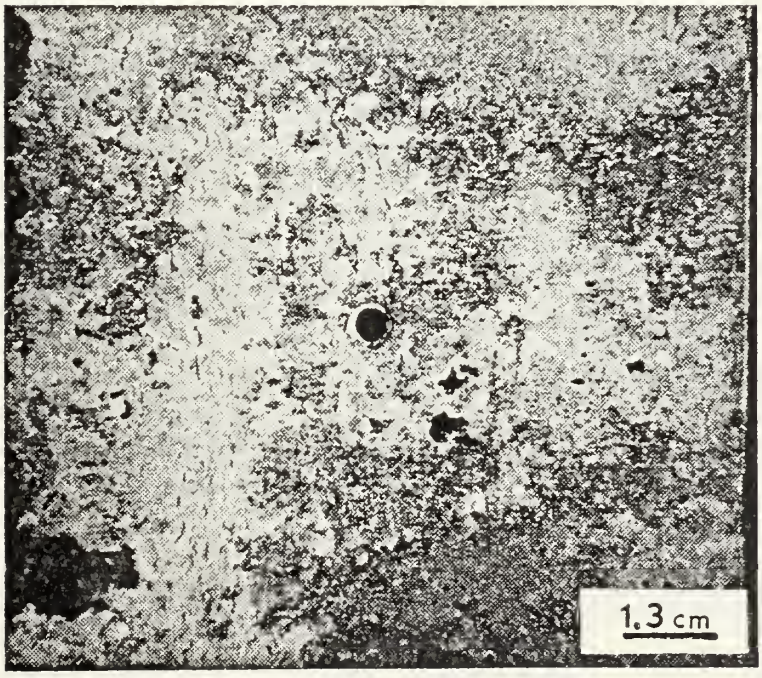

Figure 16

Galvalum® III - protected cathode after fourteen-day immersion test

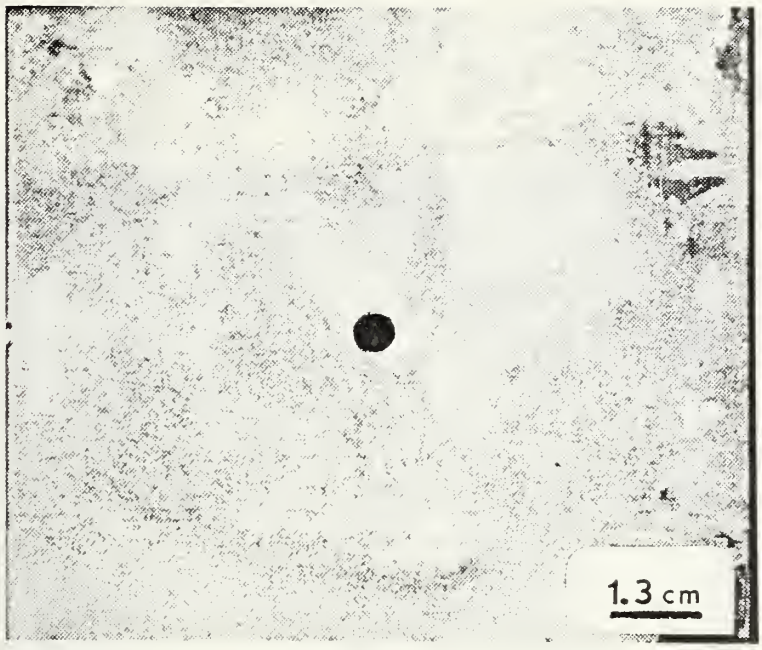

Figure 17

Reynode® II - protected cathode after fourteen-day immersion test

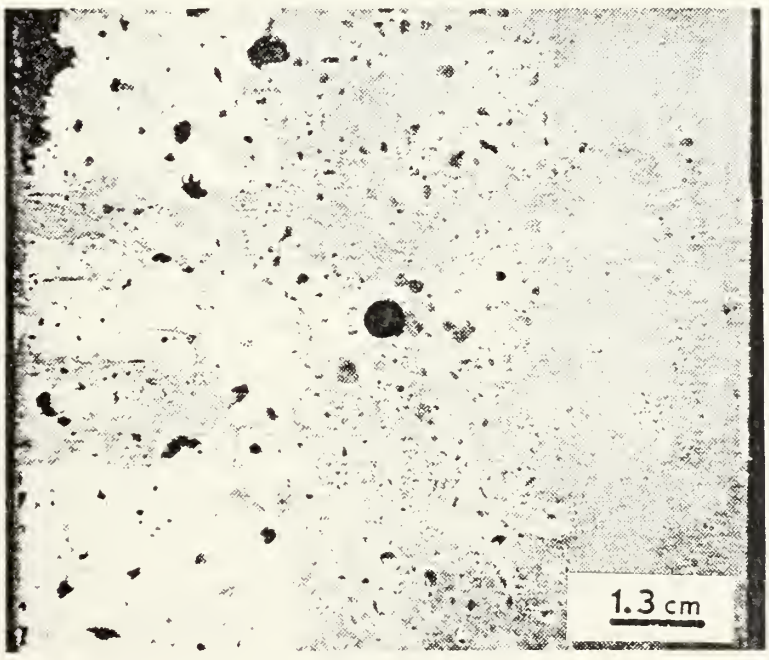

Figure 18

KA-90® - protected cathode after fourteen-day immersion test

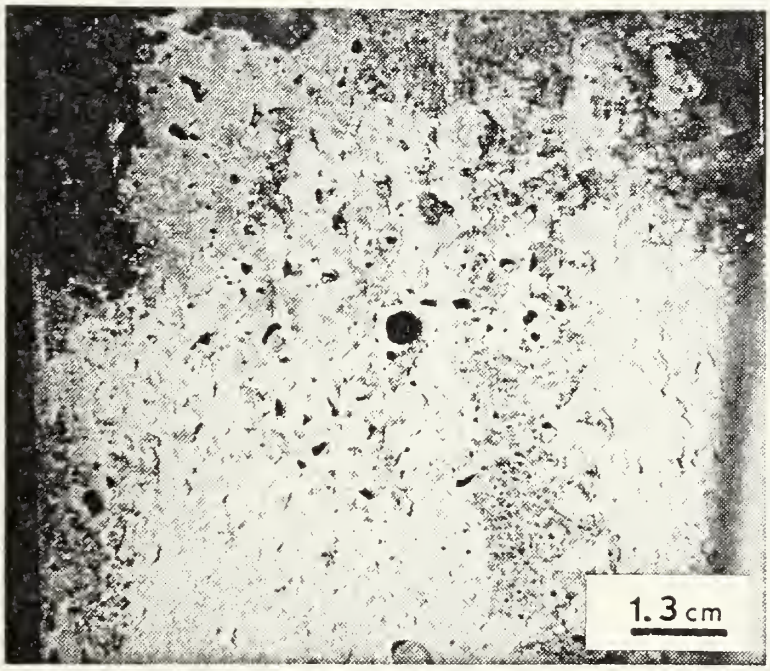

Figure 19

KA-95® - protected cathode after fourteen-day immersion test

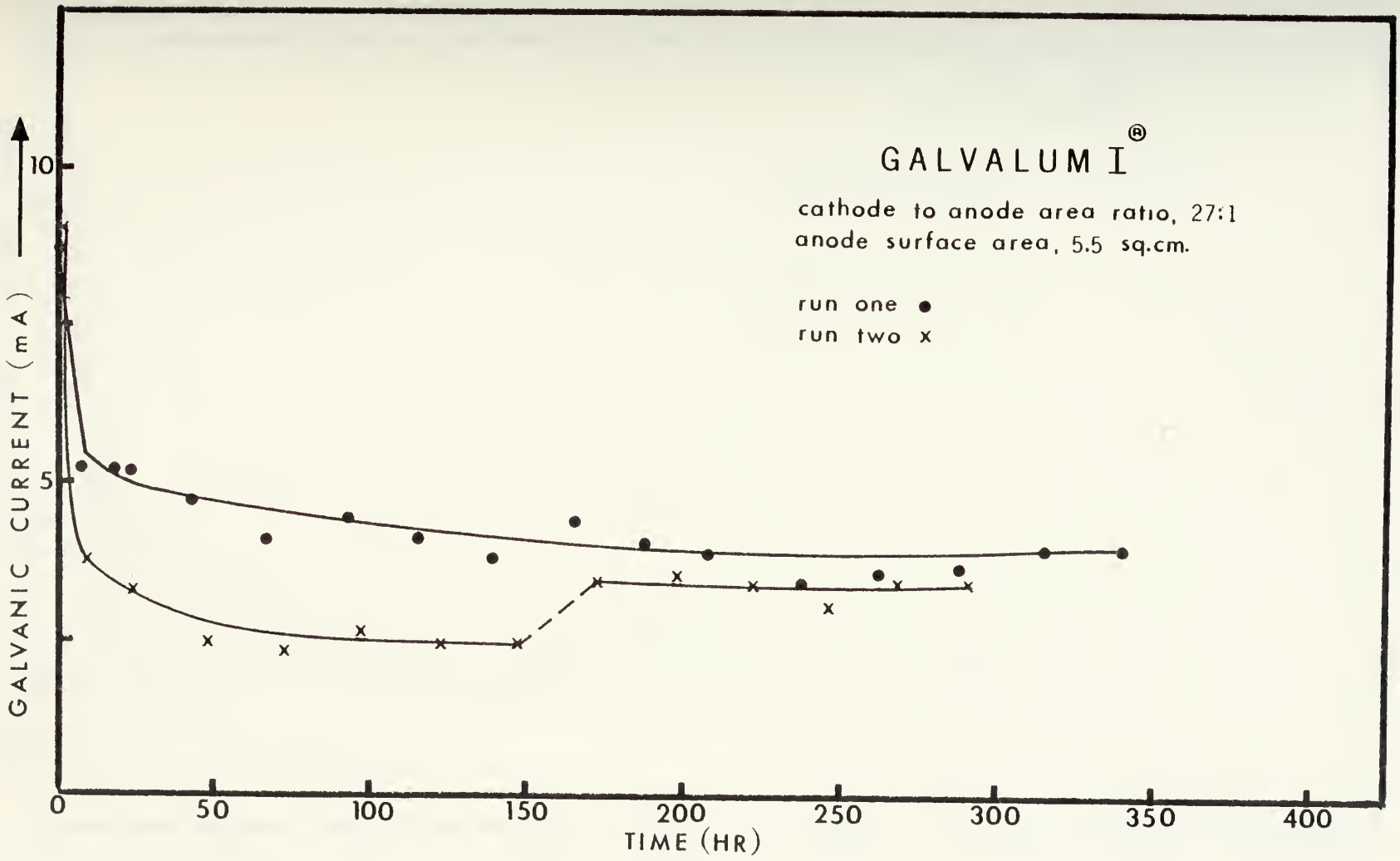

Figure 20

Galvanic current vs. time curves of the fourteen-day immersions of Galvalum®I

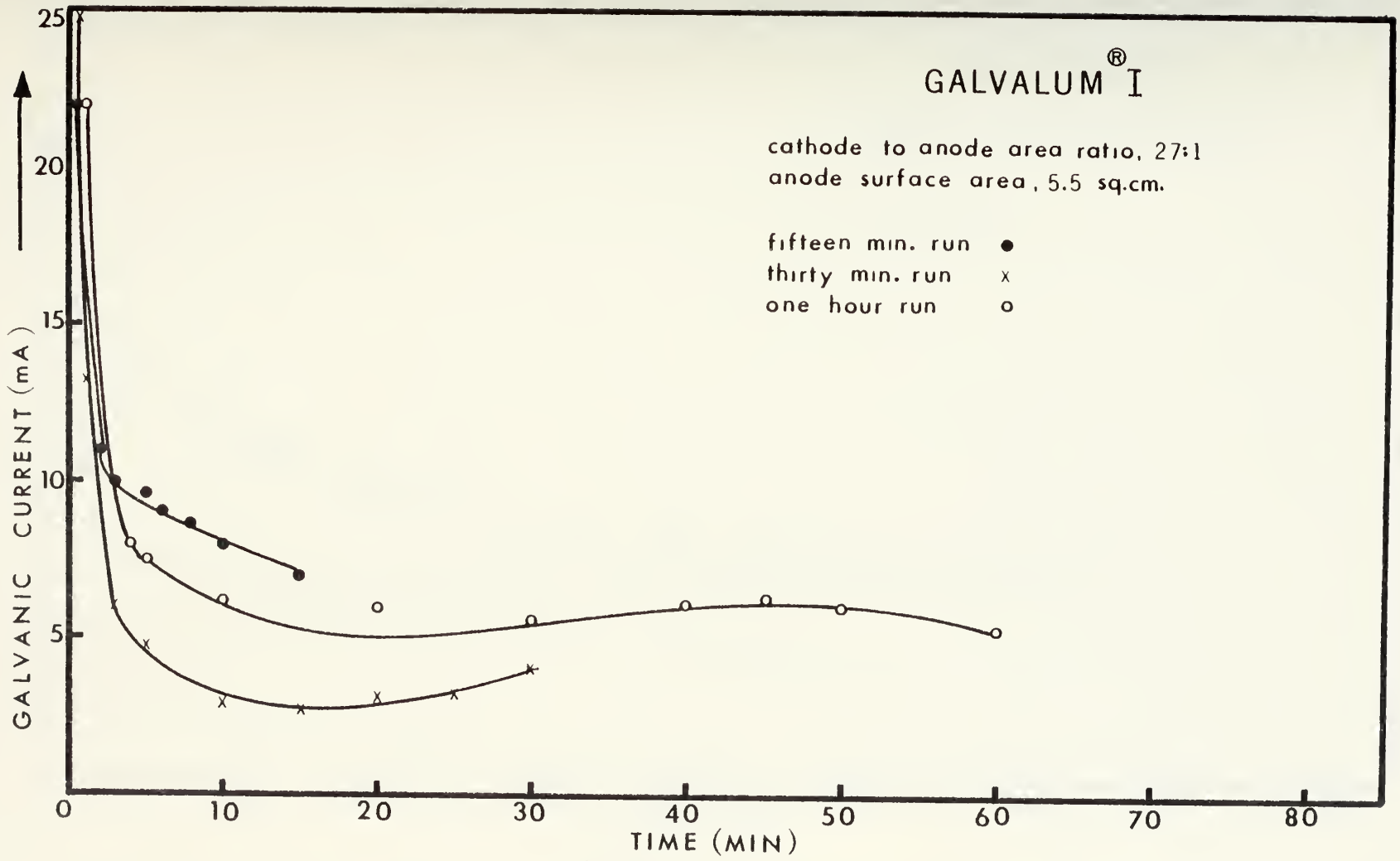

Figure 21

Galvanic current vs. time curves of the fifteen-minute, thirty-minute and one-hour immersions of Galvalum®I

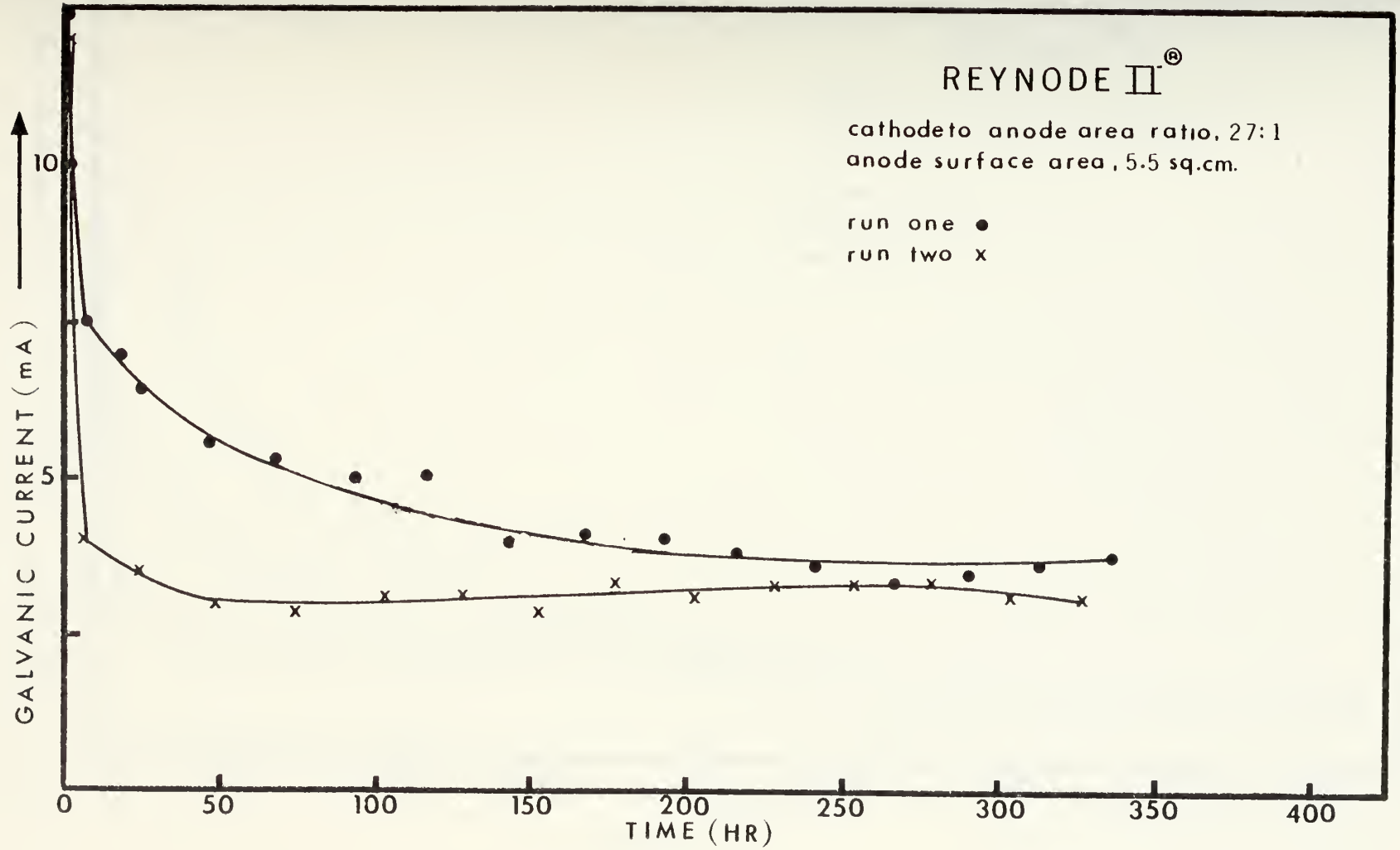

Figure 22

Galvanic current vs. time curves of the fourteen-day immersions of Reynode® II

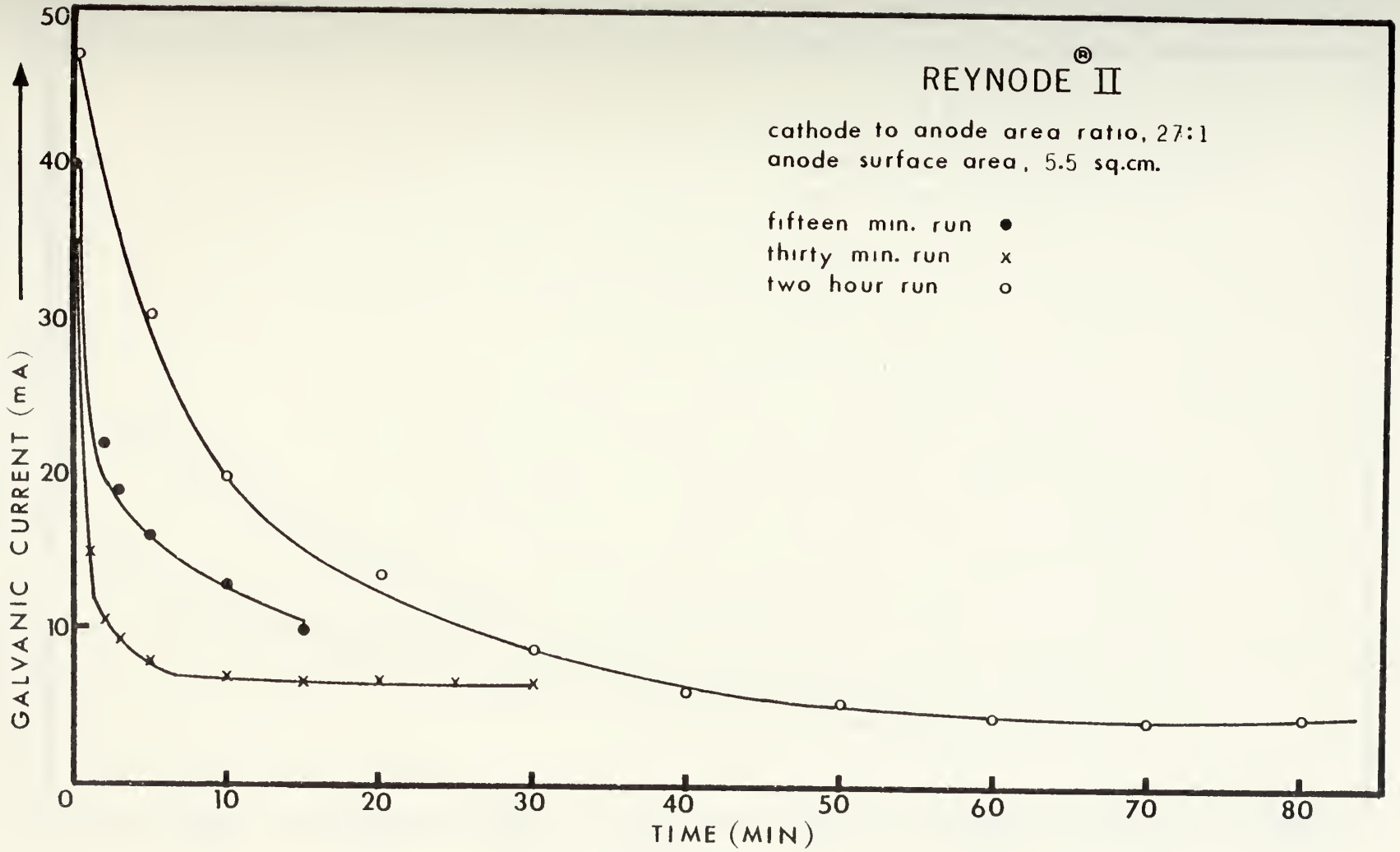

Figure 23

Galvanic current vs. time curves of the fifteen-minute, thirty-minute and two-hour immersions of Reynode®II

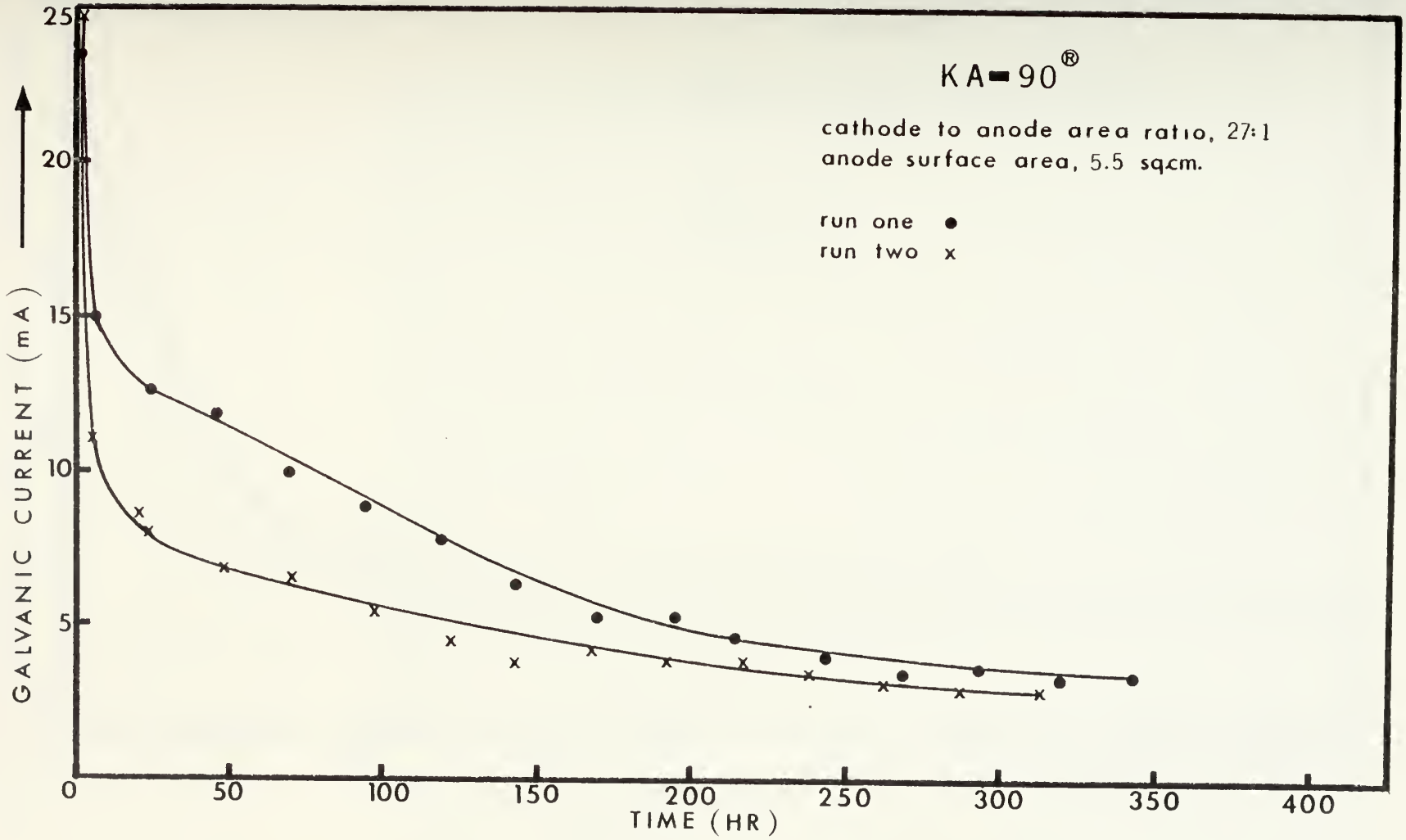

Figure 24

Galvanic current vs. time curves of the fourteen-day immersions of KA-90®

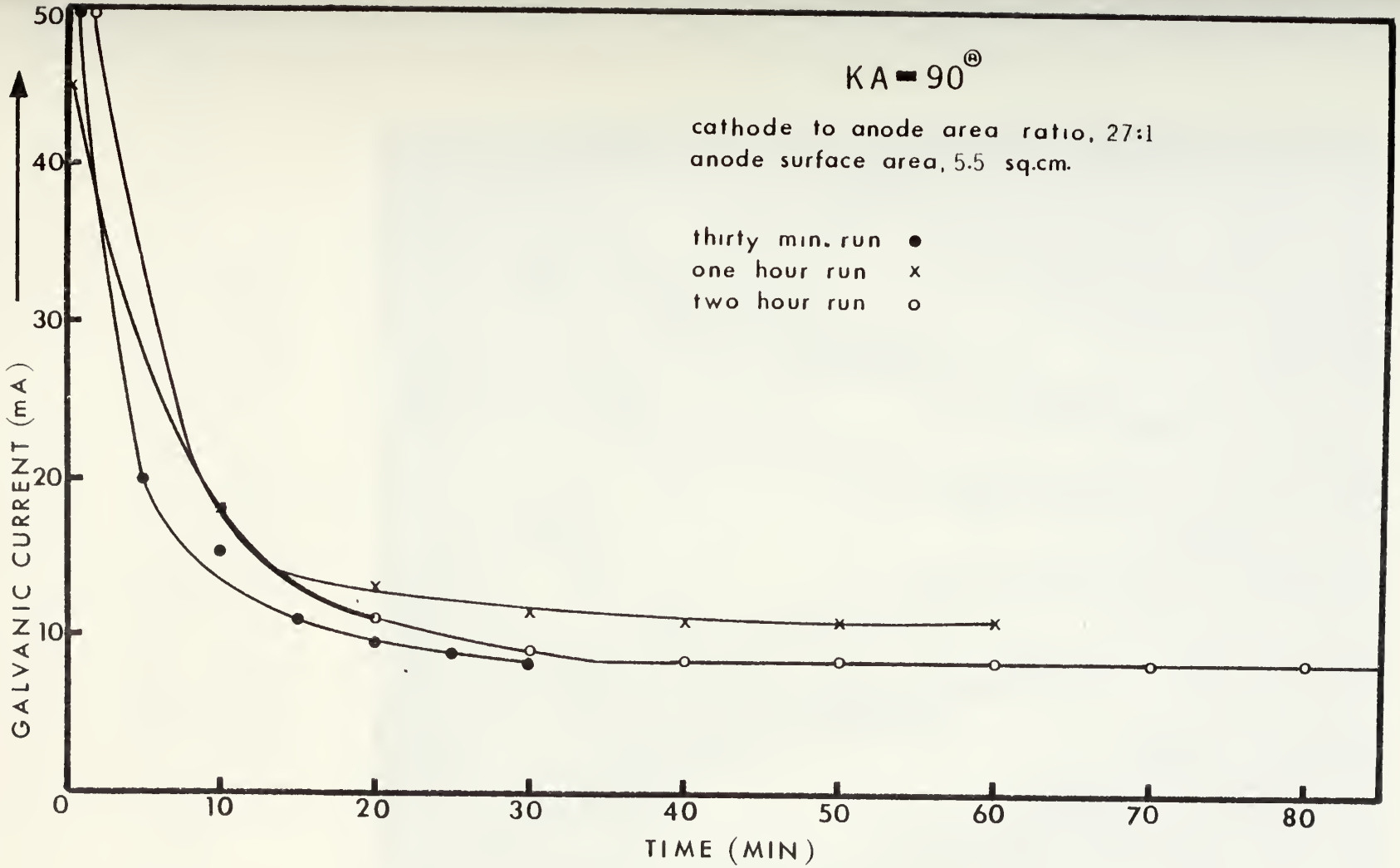

Figure 25

Galvanic current vs. time curves of the fifteen-minute, one-hour and two-hour immersions of KA-90®

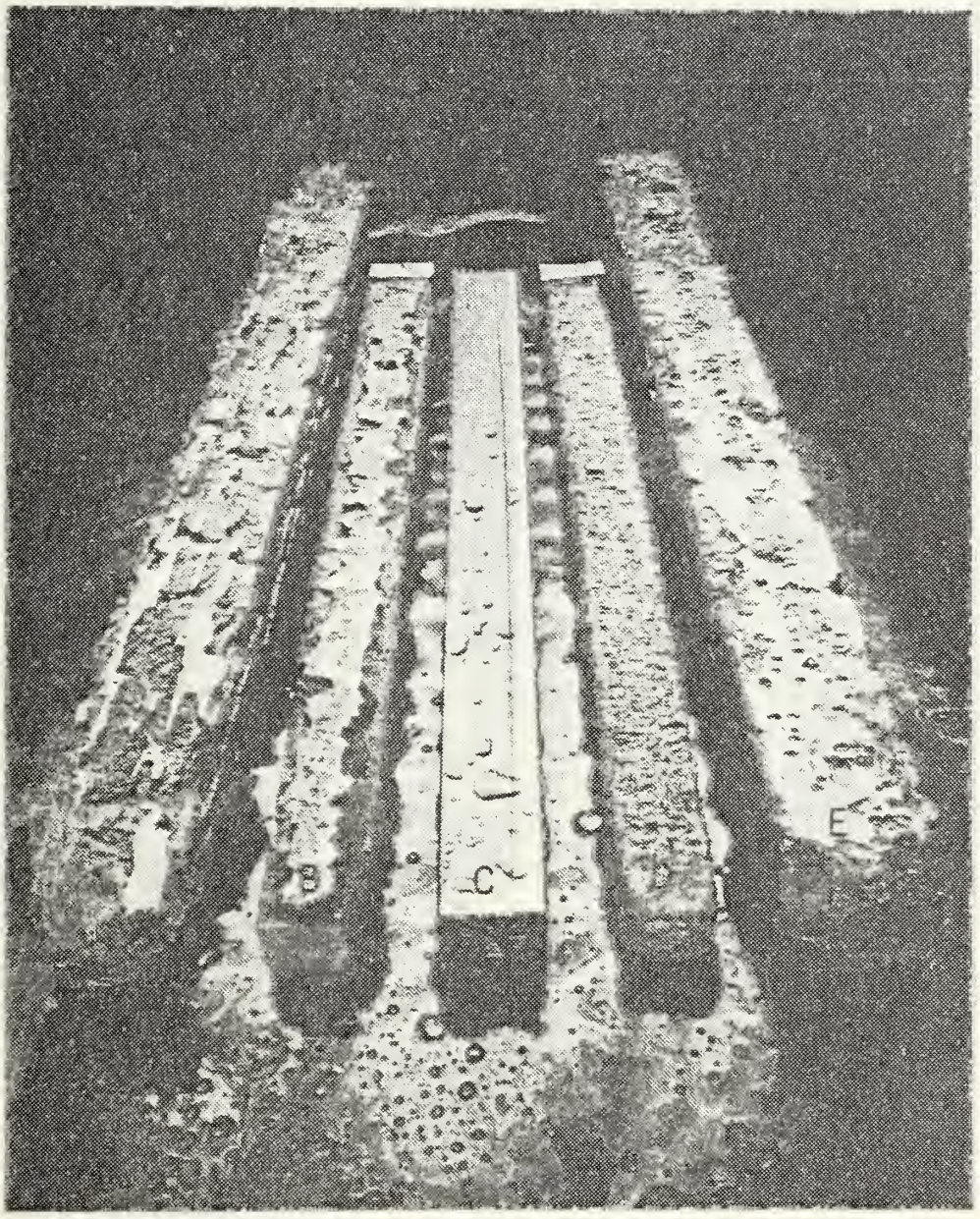

Figure 26

Illustration of macroscopic corrosion patterns on large-scale aluminum sacrificial anode alloy specimens (1.5 in. x 1.5 in. x 15 in. (3.8 cm x 3.8 cm x 38 cm), Ref. 44. From the left the anodes are believed to be: (a) Reynode®II, (b) KA-95®, (c) unexposed anode, (d) KA-90® and (e) Galvalum®I.)

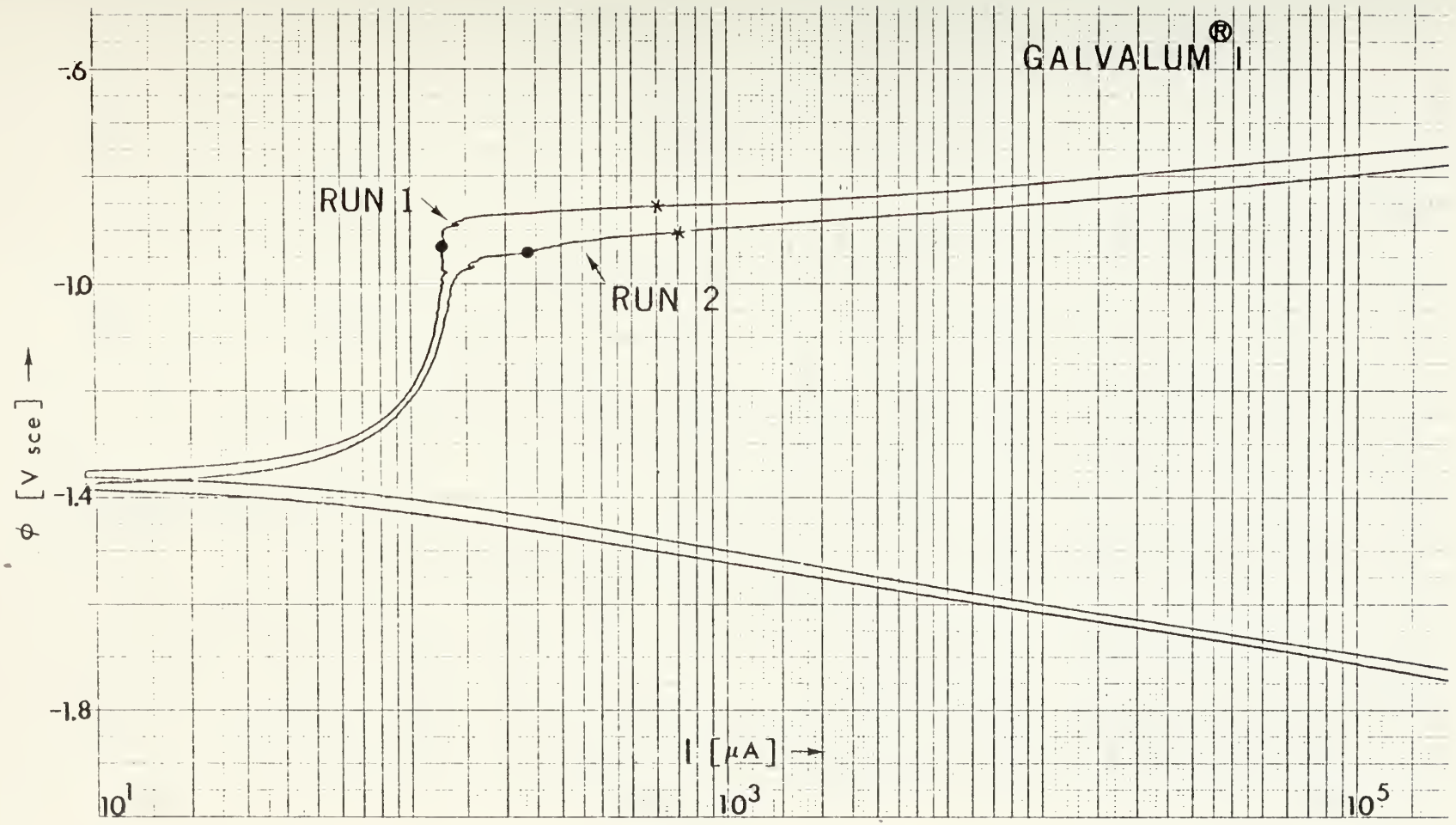

Figure 27

Potentiodynamic polarization plots of Galvalum® I, runs 1 and 2

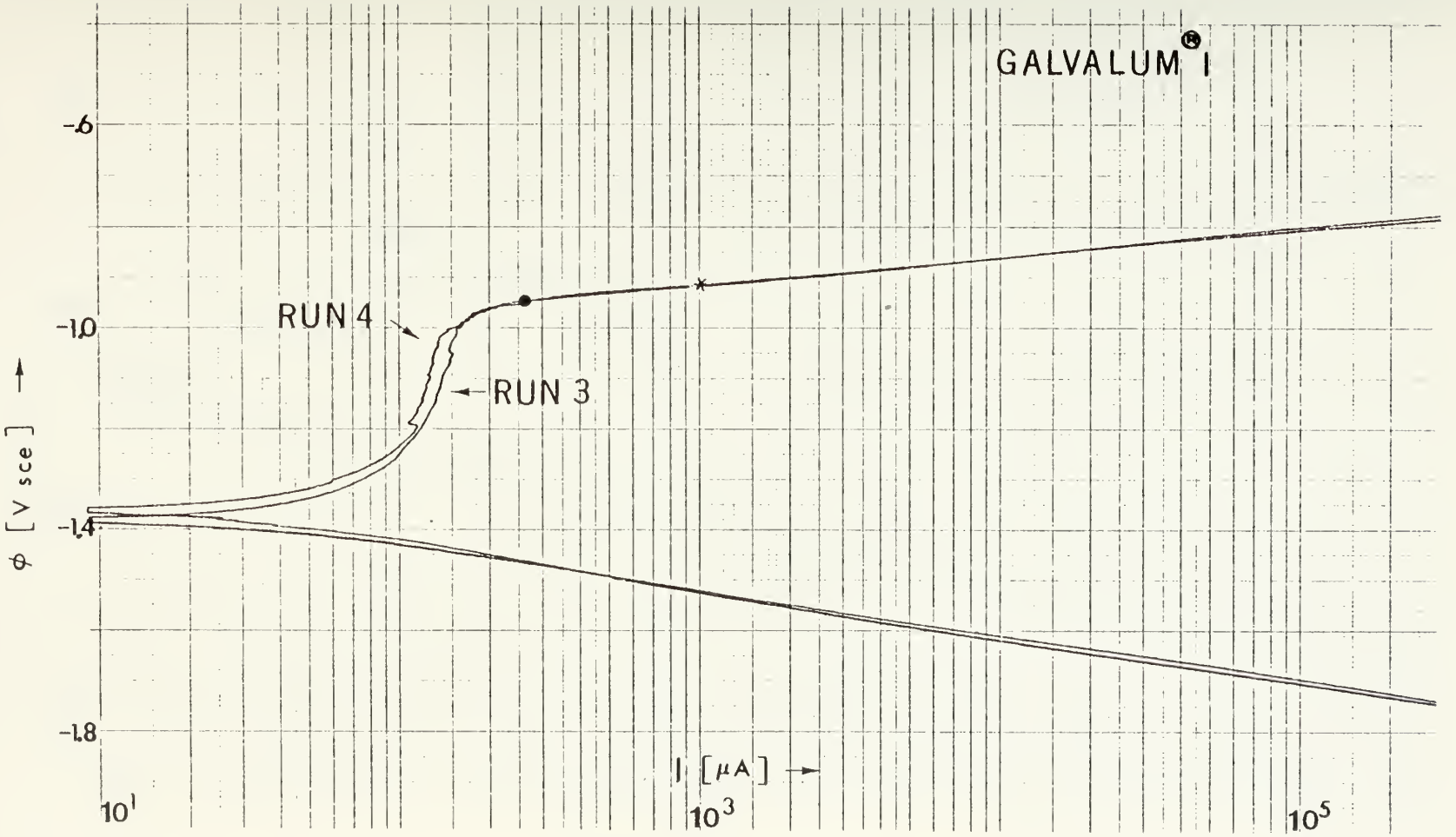

Figure 28

Potentiodynamic polarization plots of Galvalum® I, runs 3 and 4

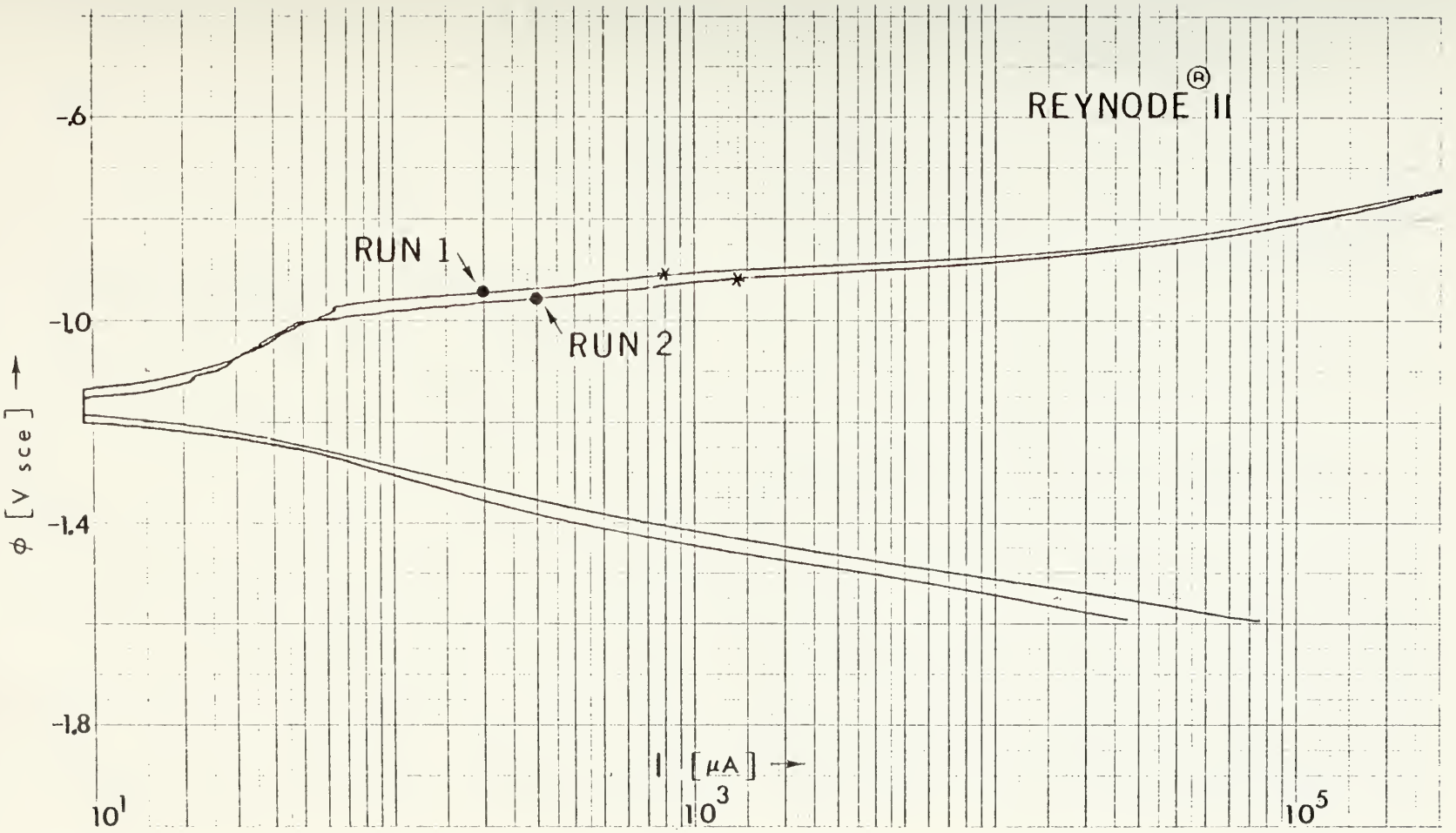

Figure 29

Potentiodynamic polarization plots of Reynode® II, runs 1 and 2

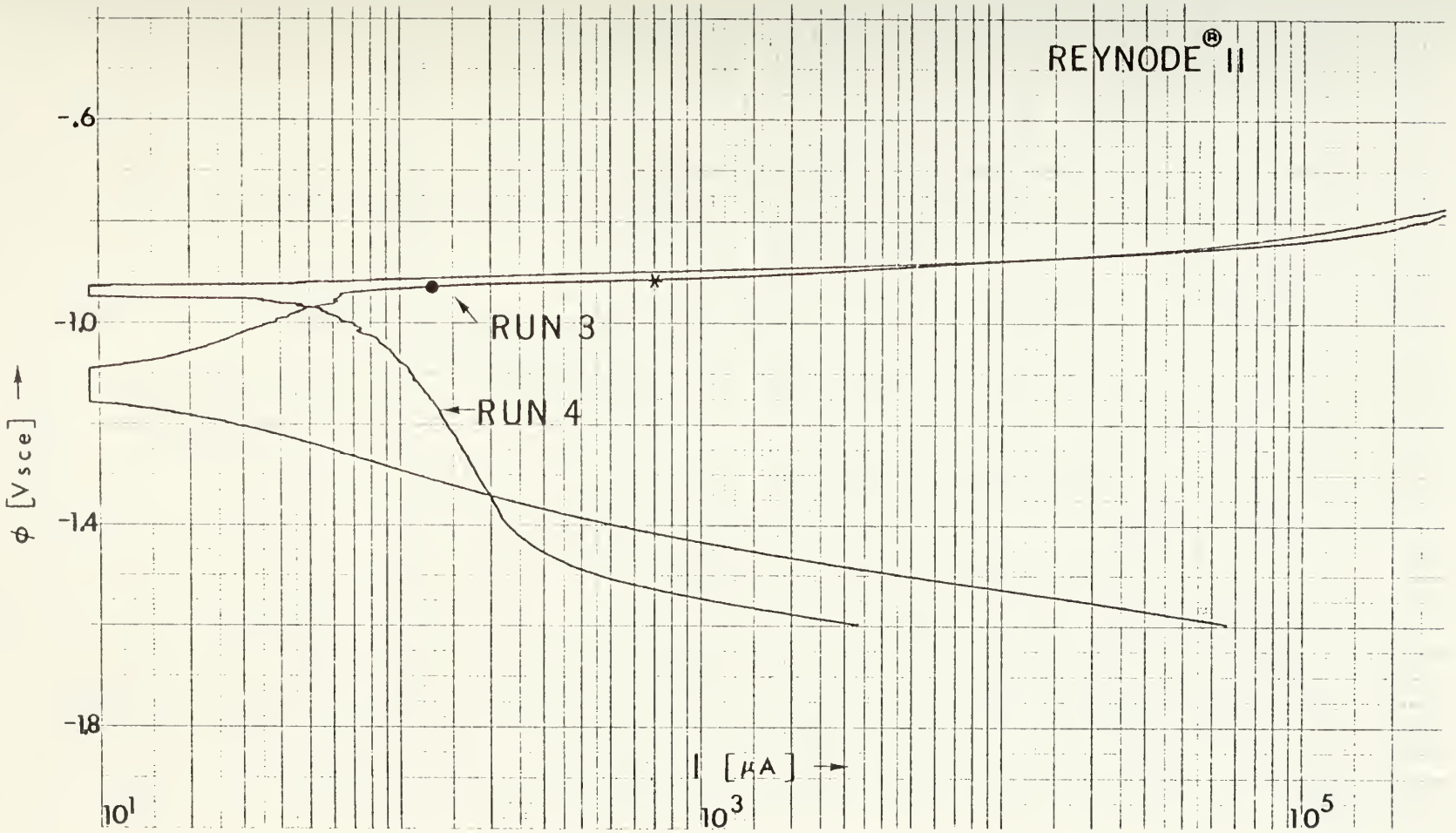

Figure 30

Potentiodynamic polarization plots of Reynode®II, runs 3 and 4

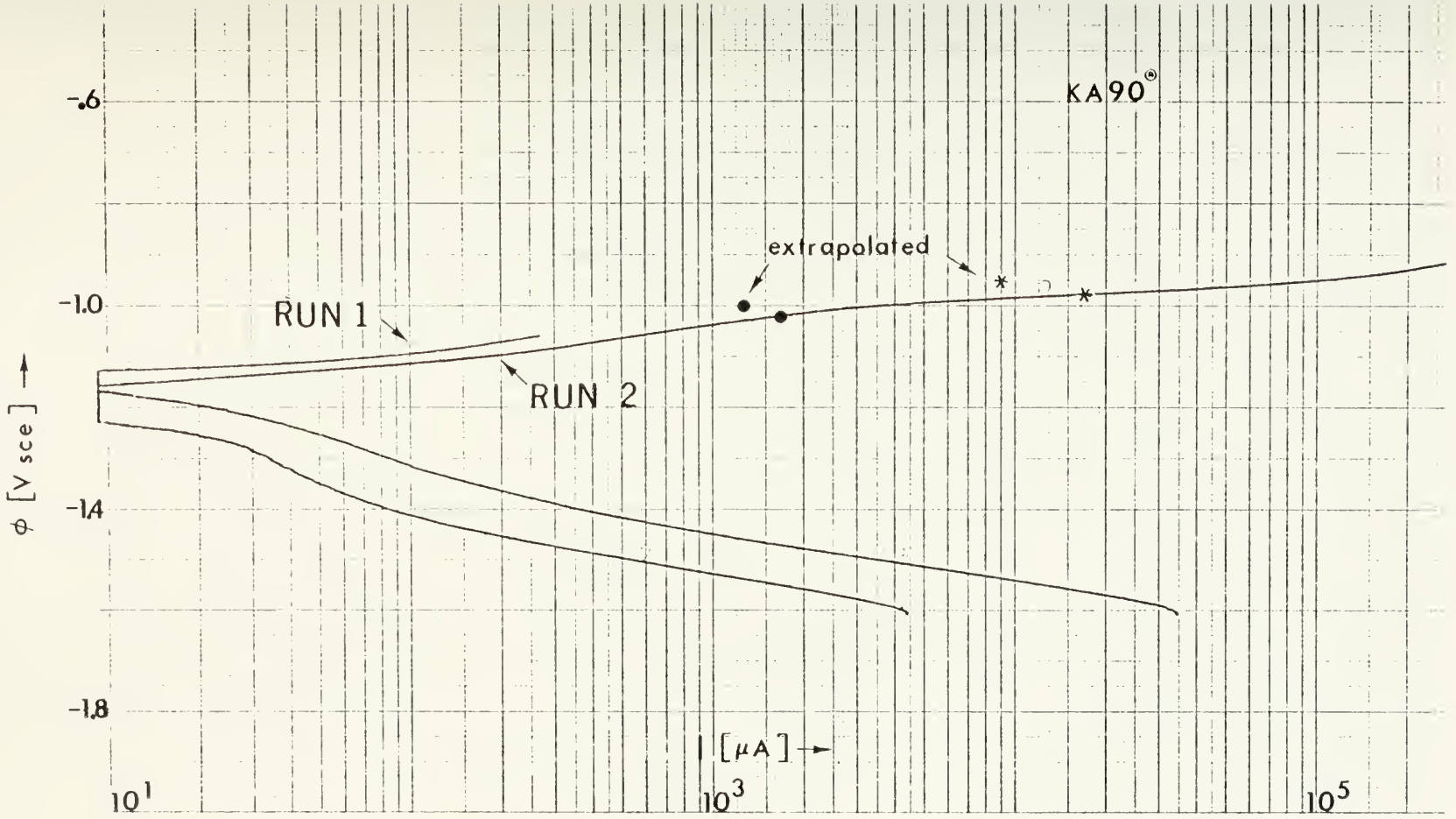

Figure 31

Potentiodynamic polarization plots of KA-90®, runs 1 and 2

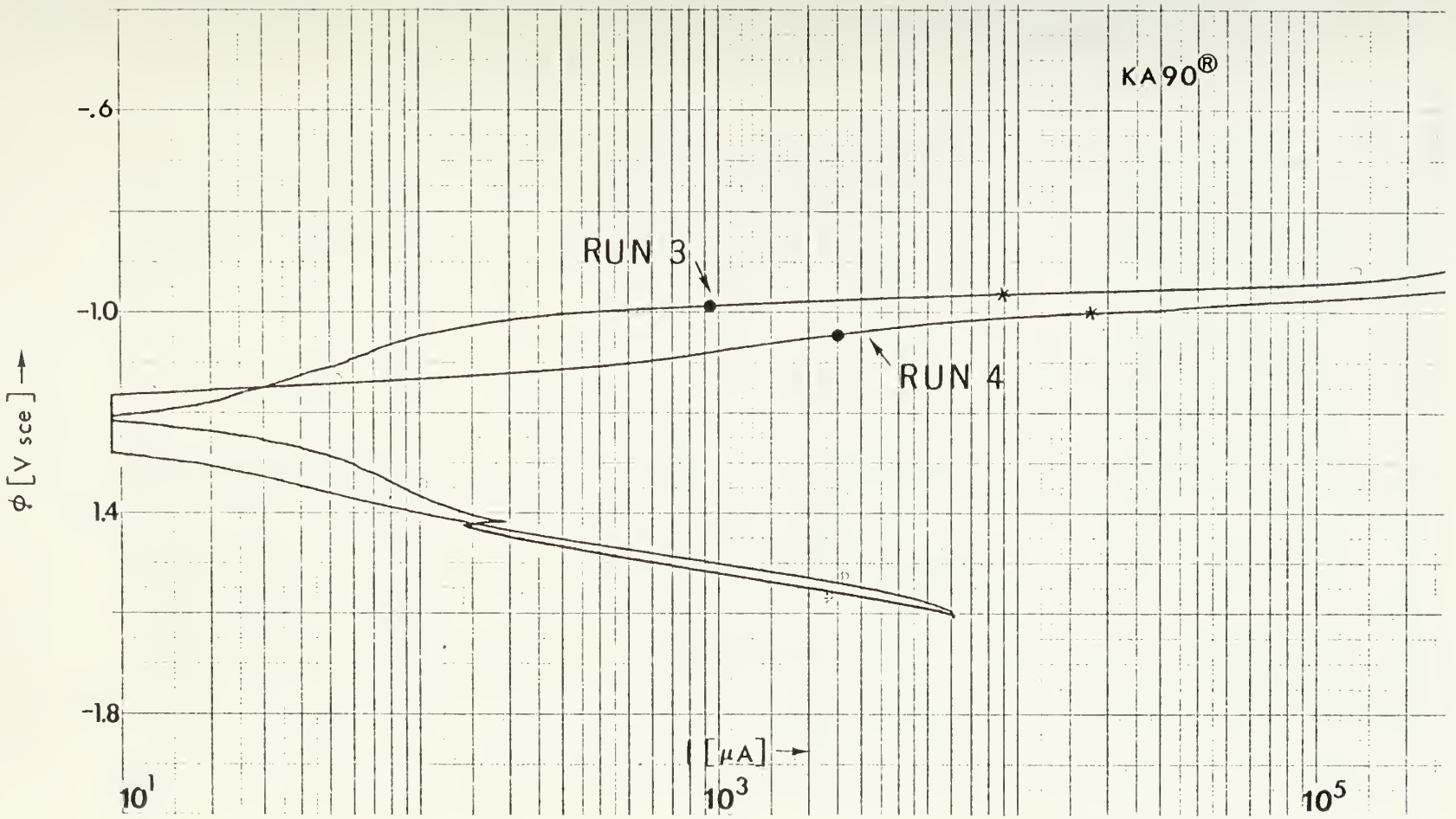

Figure 32

Potentiodynamic polarization plots of KA-90®, runs 3 and 4

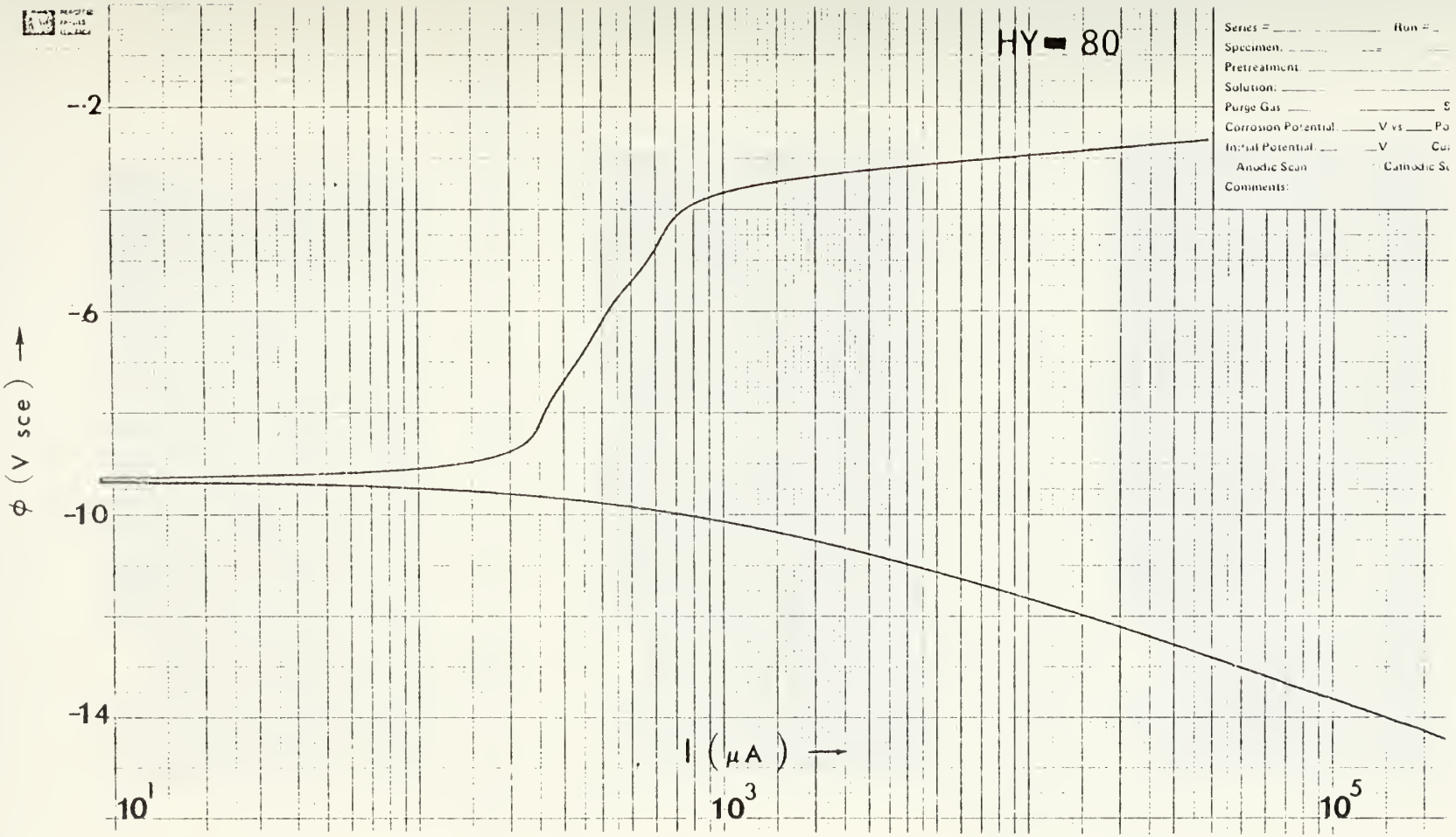

Figure 33

Potentiodynamic polarization plot of HY-80 steel

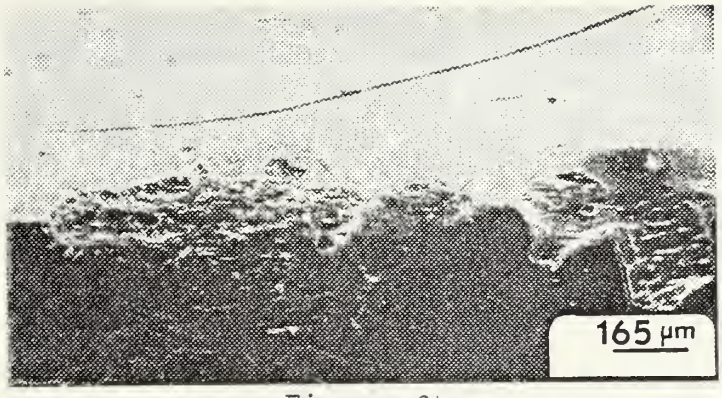

Figure 34

GI-0.25 (50X) Corroded area on the edge of a Galvalum®I specimen immersed for fifteen minutes

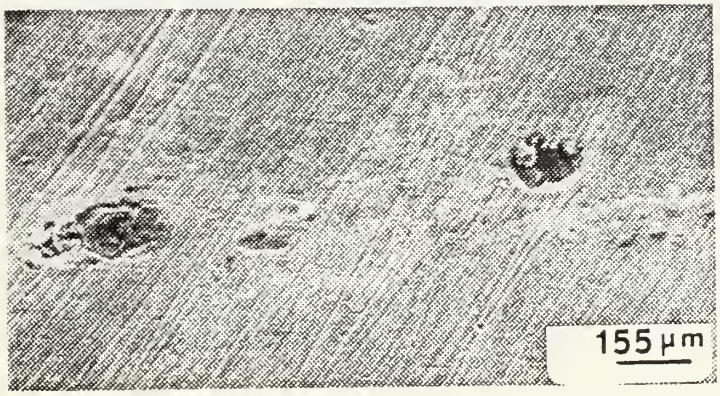

Figure 35

RII-0.25 (65X) Pitting on broad surface of Reynode®II specimen immersed for fifteen minutes

Figure 36

KA90-0.25 (60X) Generalized pitting attack on broad surface of KA-90® specimen immersed for fifteen minutes

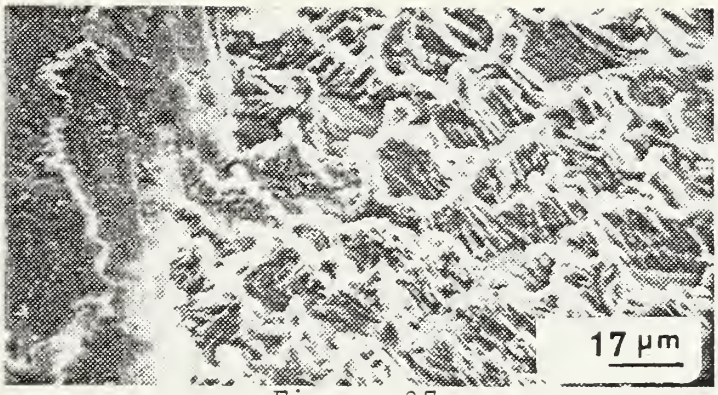

Figure 37

GI-24 (610X) Herringbone pattern on dissolution surface of Galvalum®I immersed for twenty-four hours

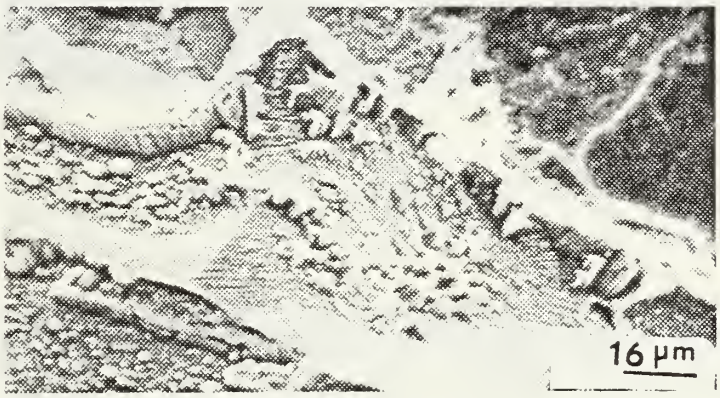

Figure 38

RII-24 (600X) Dissolution surface of pit on Reynode®II specimen immersed for twenty-four hours

Figure 39

KA90-24 (600X) Dissolution surface of KA-90® specimen immersed for twenty-four hours

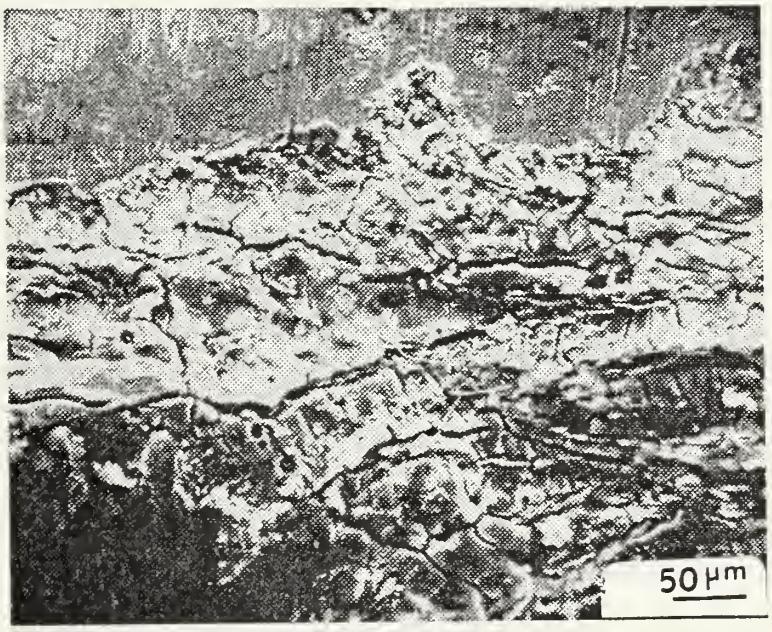

Figure 40

GI-0.25 (200X) Galvalum® I specimen immersed for fifteen minutes showing cracked crust formation on an edge of the anode

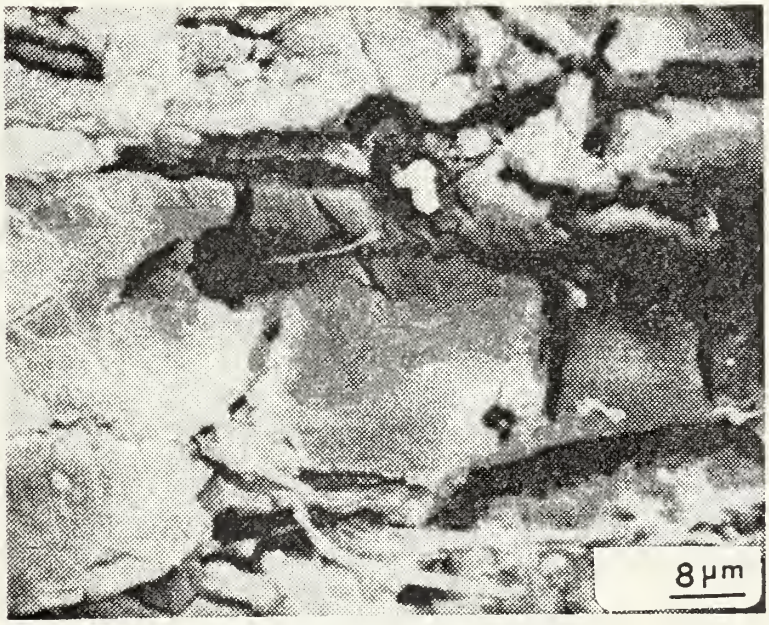

Figure 41

GI-0.25 (1250X) Magnified View of Figure 40, showing the unstructured cracked crust

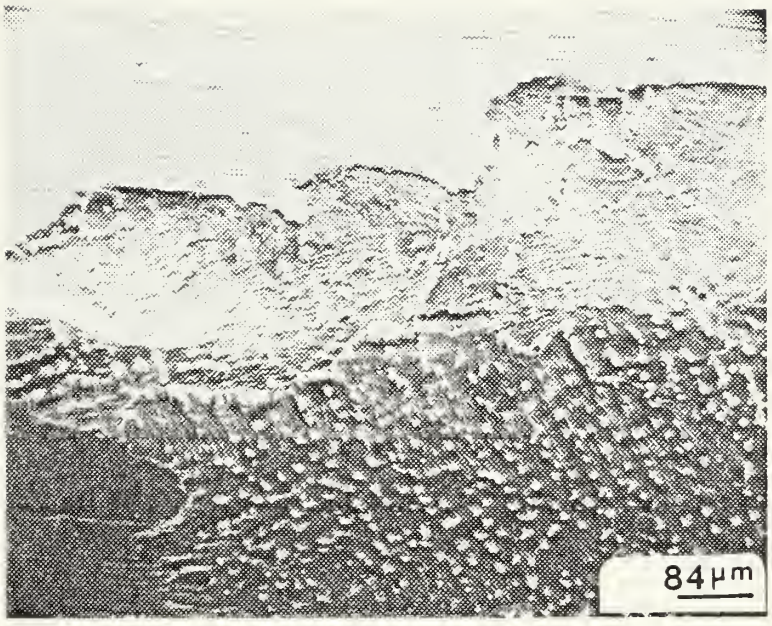

Figure 42

GI-1 (120X) Galvalum®I specimen after one-hour immersion showing regular patterns on dissolution surface

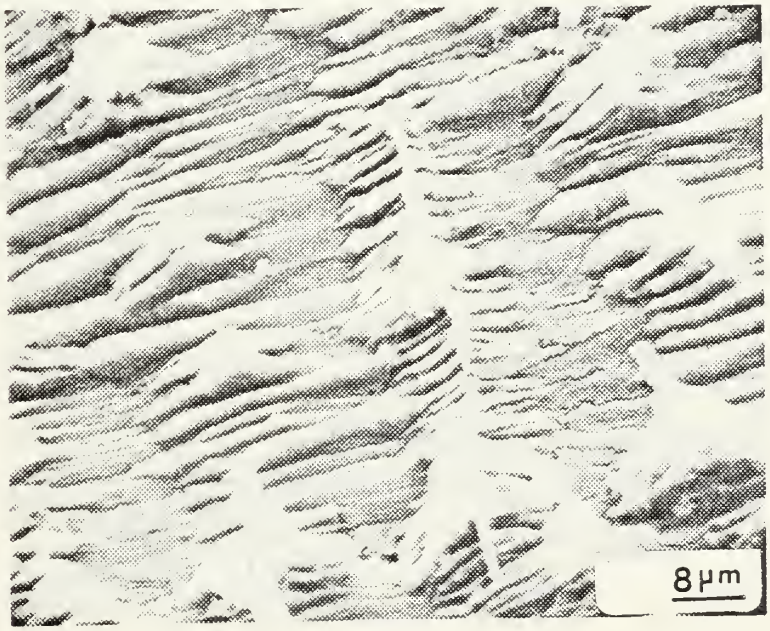

Figure 43

GI-1 (1220X) Magnified view of Figure 42, showing the "herringbone" dissolution pattern on one grain surface

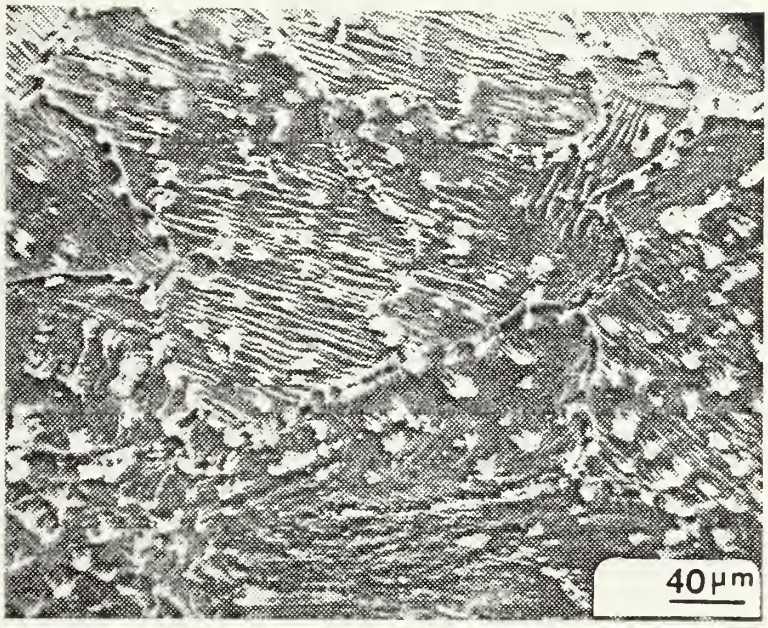

Figure 44

GI-2 (250X) Galvalum®I two-hour immersion specimen showing directionality of the herringbone dissolution patterns on different grains

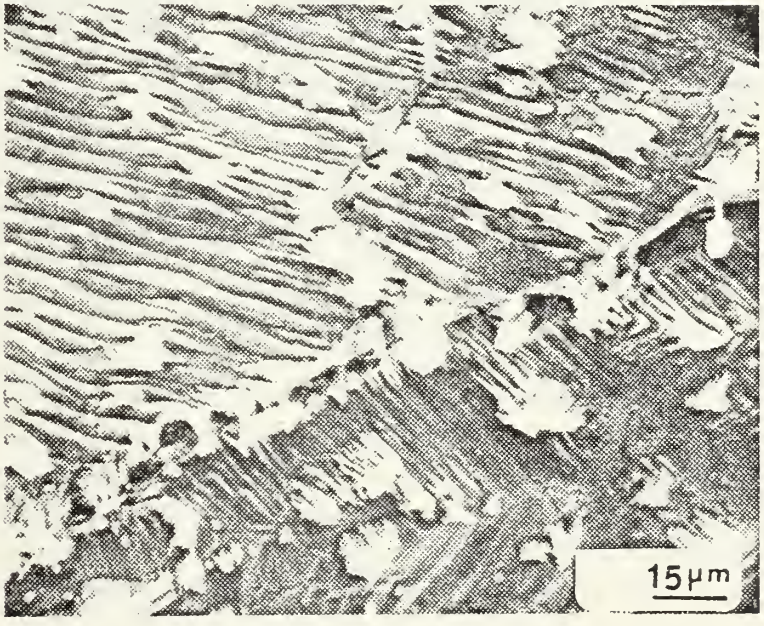

Figure 45

GI-2 (650X) Evidence of slight increase of corrosive attack between the grains on Galvalum®I two-hour immersion specimen

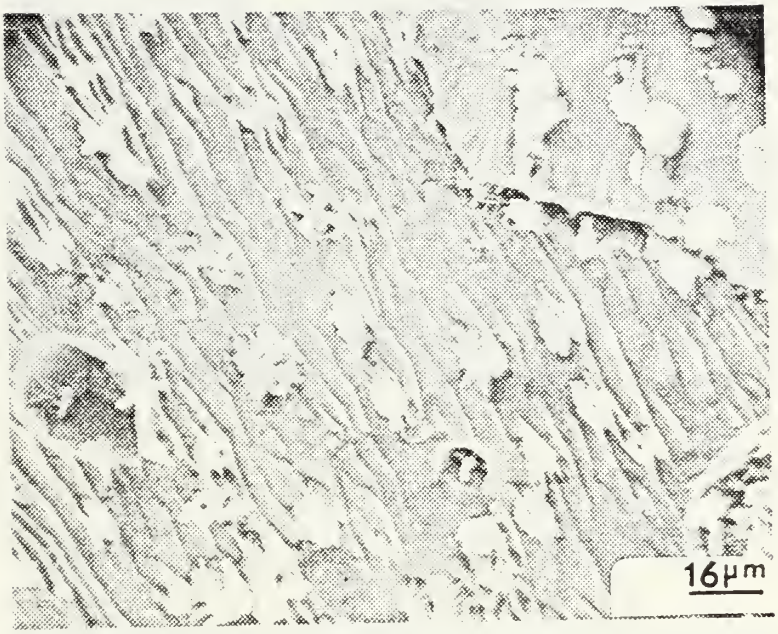

Figure 46

GI-1 (610X) Grain boundary (at upper right) clearly illustrates stepped structure formed by preferential etch of non-close-packed planes

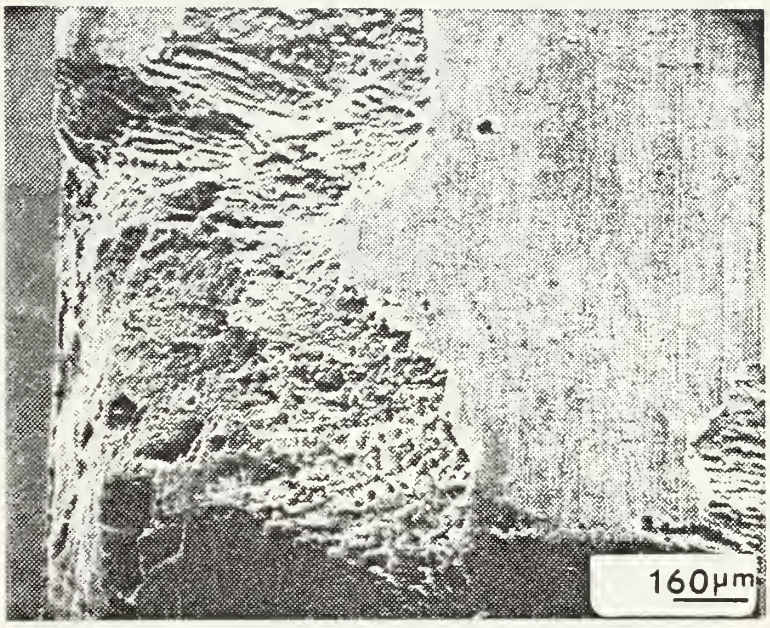

Figure 47

GI-4 (63X) Galvalum®I four-hour immersion specimen showing dissolution regions advancing from the edge of the specimen

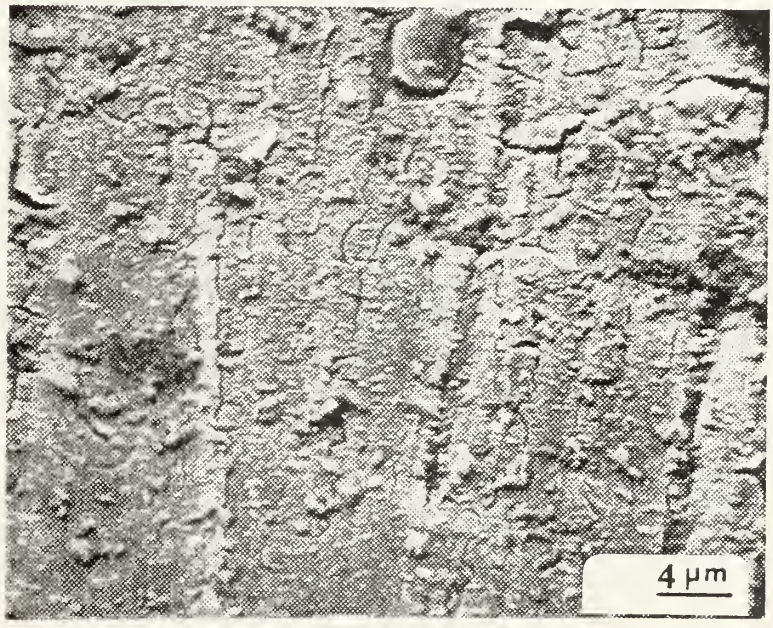

Figure 48

GI-4 (2300X) Galvalum®I four-hour immersion specimen showing cracked film on uncorroded surface

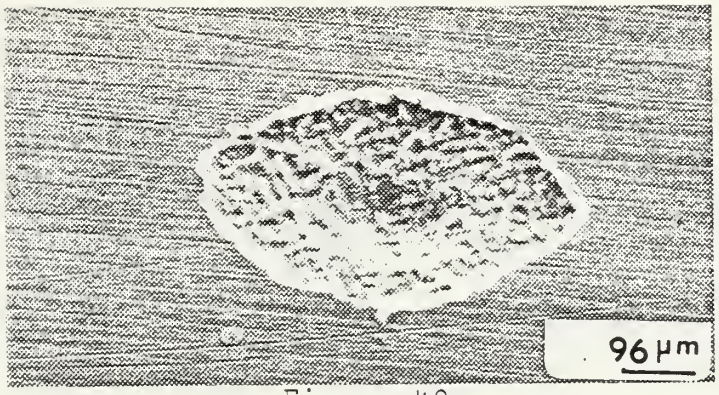

Figure 49

GI-12 (110X) Pit in center of Galvalum® I twelve-hour immersion specimen - one of very few dissolution cavities which initiated on the broad surface of a Galvalum® I specimen

Figure 50

GI-12 (530X) Magnified view of the center of the pit shown in Figure 49

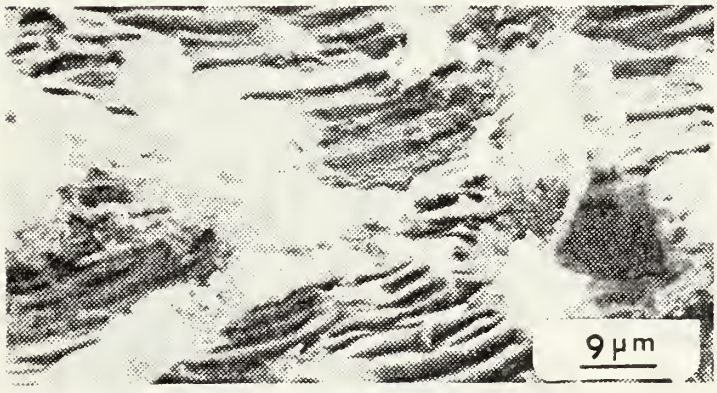

Figure 51

GI-12 (1100X) Magnified view of Figure 50 showing a buildup of corrosion product on the herringbone spine

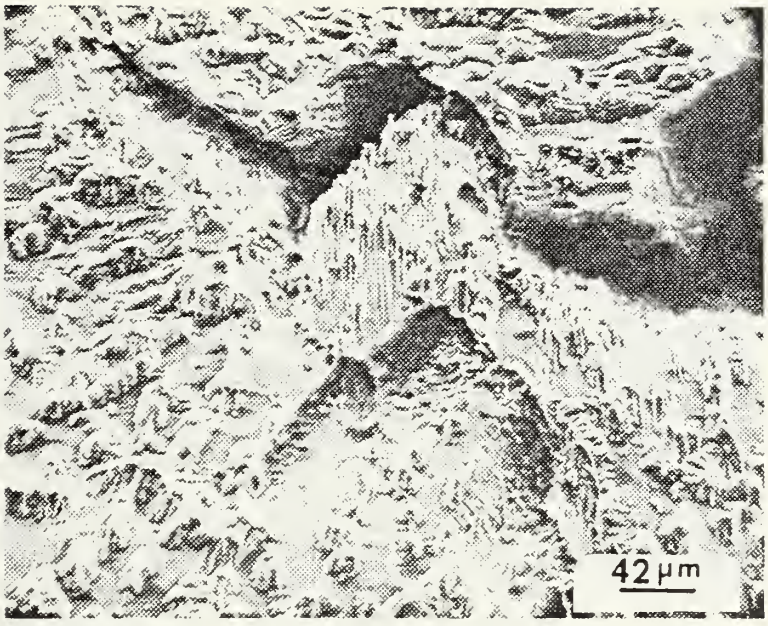

Figure 52

GI-12 (240X) Evidence of increased corrosive attack at grain boundary region of Galvalum®I twelve-hour immersion specimen

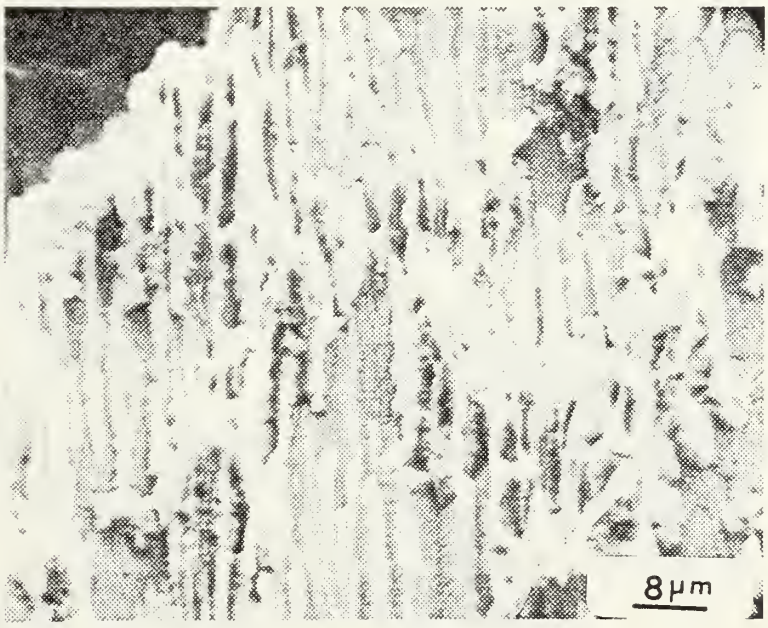

Figure 53

GI-12 (1200X) Galvalum®I twelve-hour immersion specimen showing buildup of corrosion product on spines of the herringbones

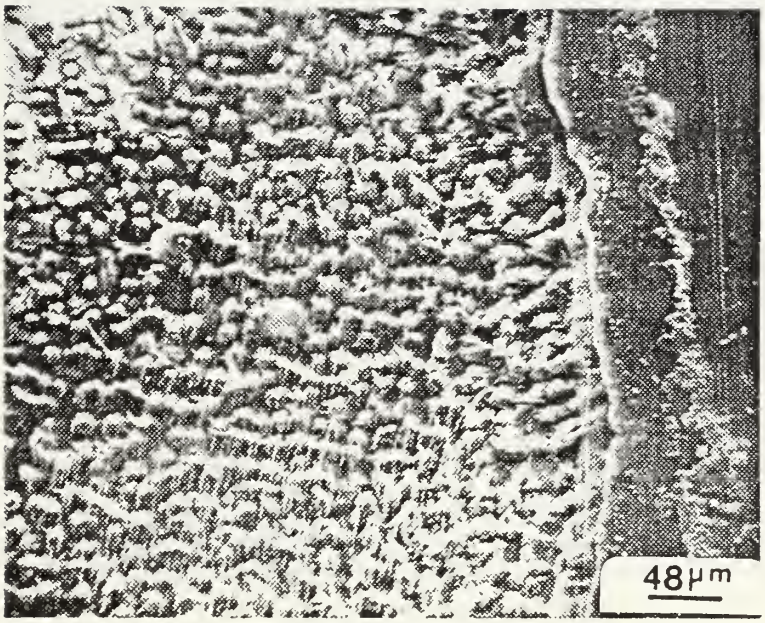

Figure 54

GI-24 (220X) Illustration of many symmetrical "herringbone" clusters and the undercutting of an uncorroded area of the Galvalum®I twenty-four-hour immersion specimen

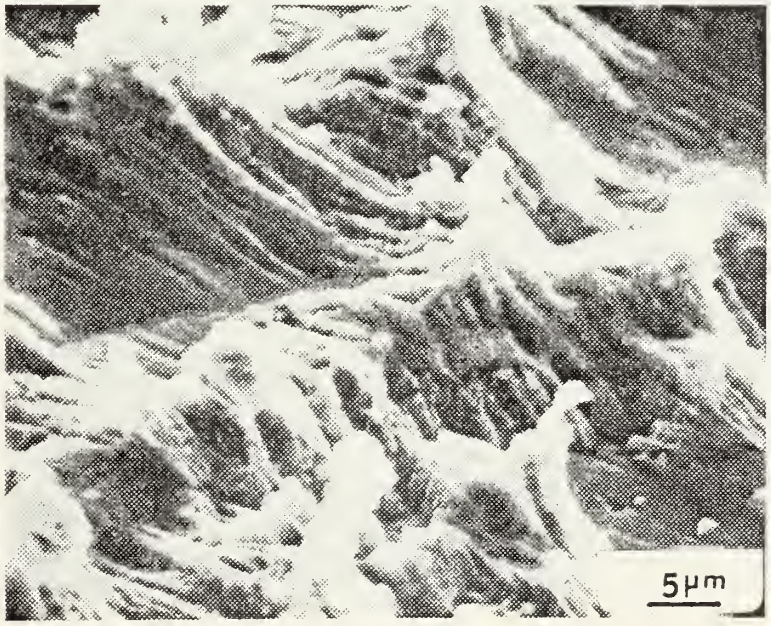

Figure 55

GI-24 (2000X) "Herringbone" pattern magnified

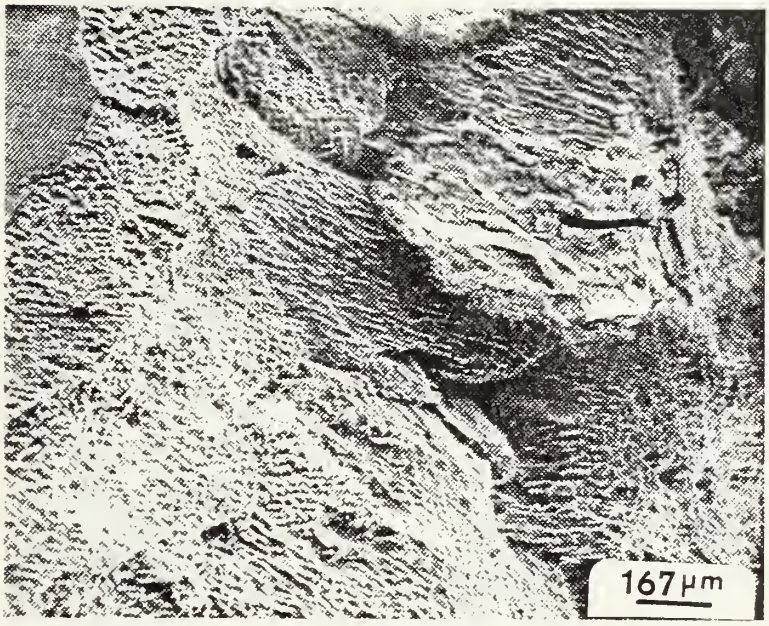

Figure 56

GI-48 (60X) Illustration of the Galvalum® I forty-eight-hour immersion specimen showing the continuing corrosion attack from the edge imward

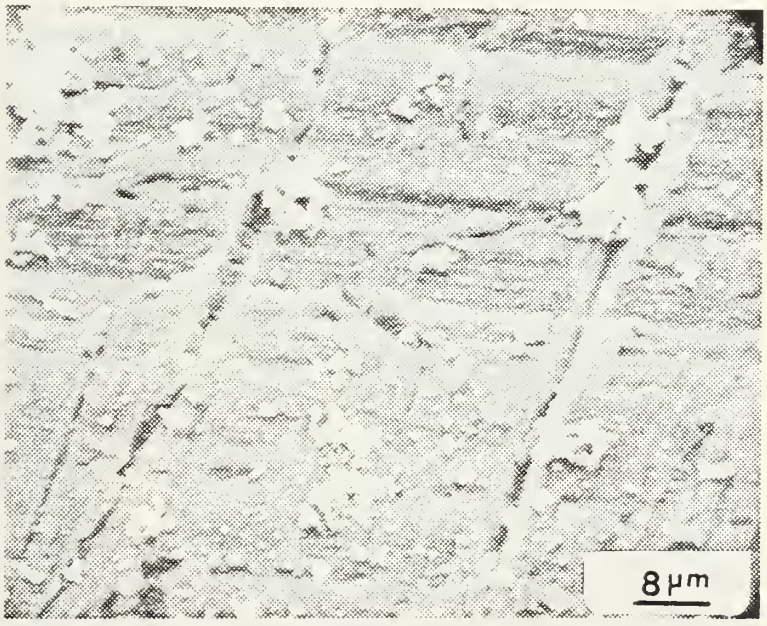

Figure 57

GI-48 (1220X) Unattacked area on the surface of Galvalum® I forty-eight-hour immersion specimen showing oxide film and flocculent corrosion product

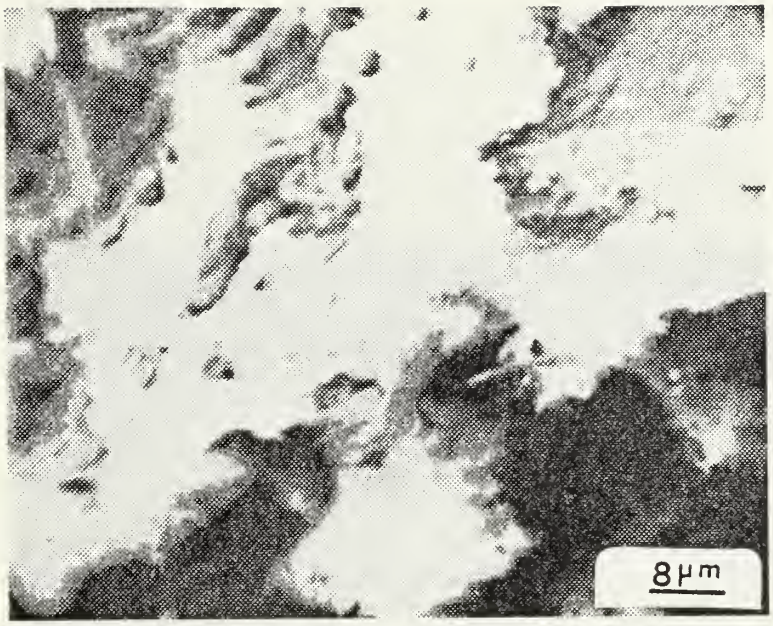

Figure 58

GI-72 (1200X) Concentration of corrosion product on top of "herringbone" spine on seventy-two-hour immersion specimen. This area was analyzed by x-ray fluorescence

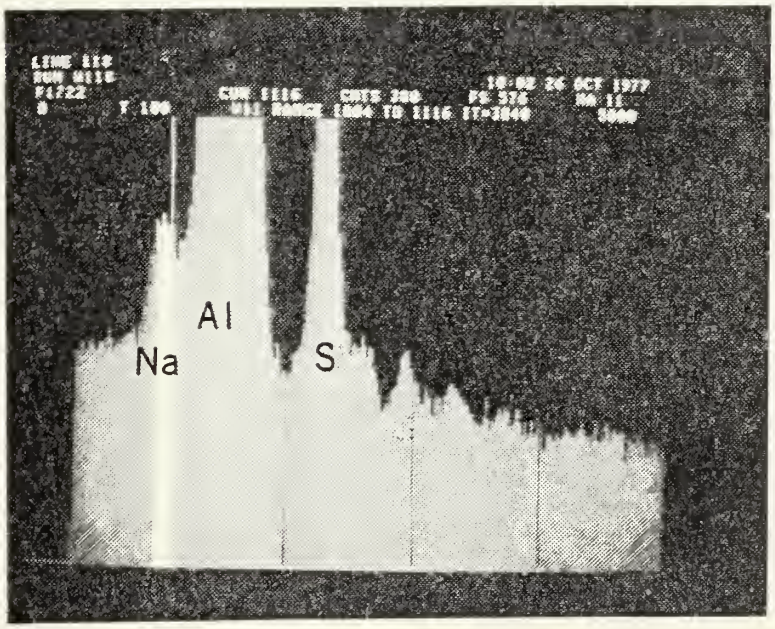

Figure 59

X-ray spectrum of the corrosion product on seventy-two-hour Galvalum®I immersion specimen shown in Figure 58

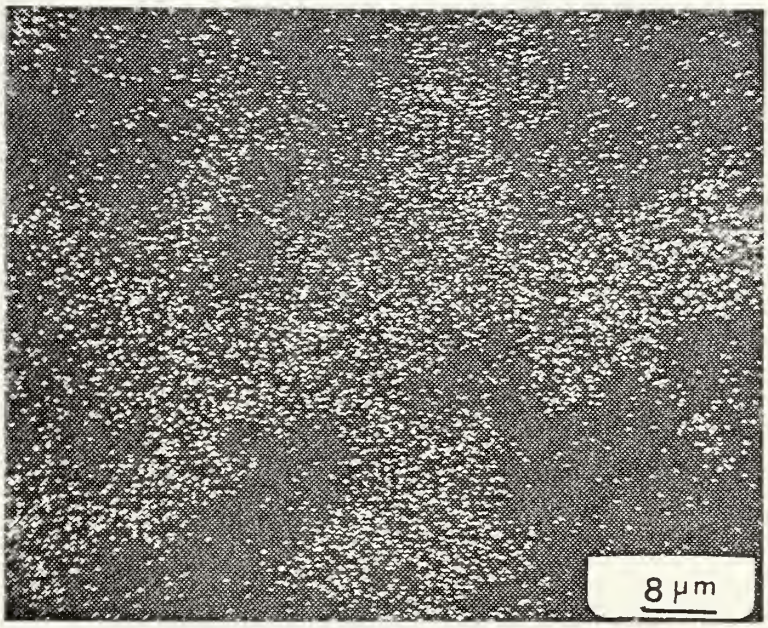

Figure 60

X-ray distribution image for sulfur, showing the presence of sulfur in the same areas as the corrosion product in Figure 58

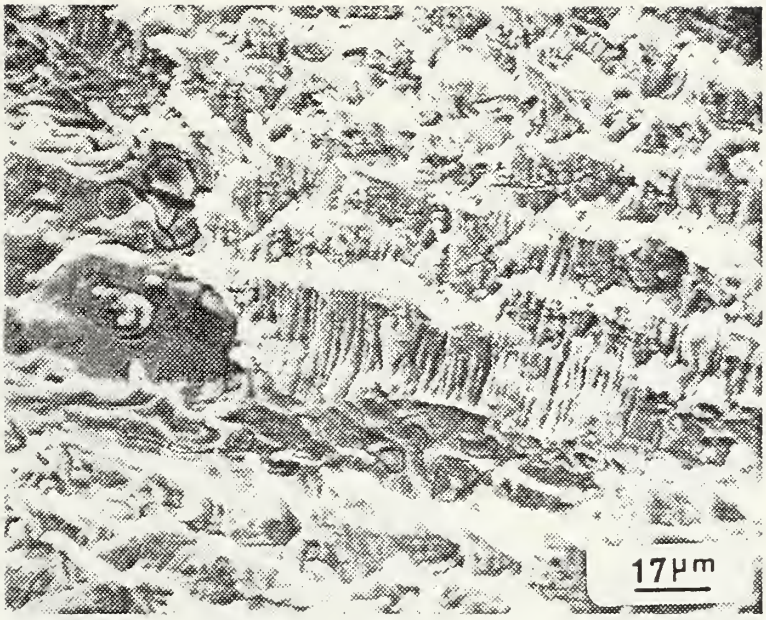

Figure 61

GI-96 (575X) Galvalum®I specimen after ninety-six-hour immersion showing "herringbone" structure and an area of cracked crust

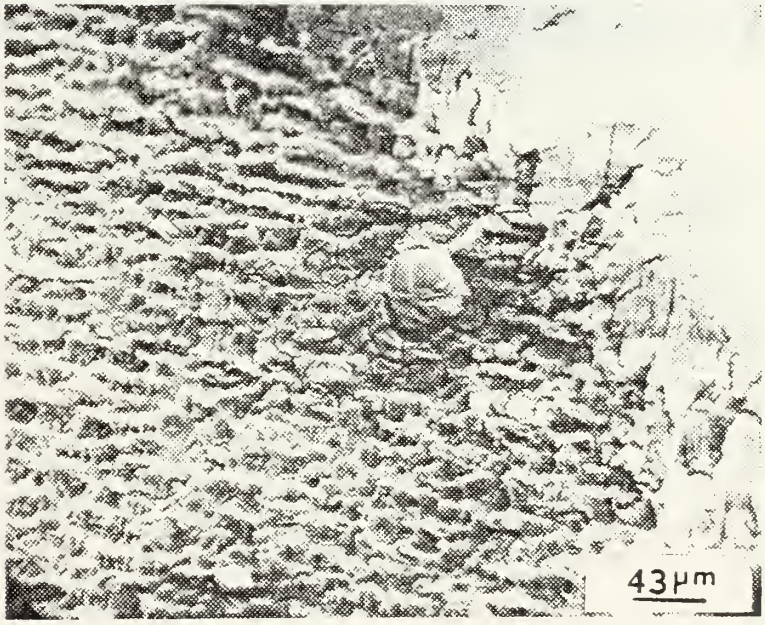

Figure 62

GI-96 (230X) Area of ninety-six-hour immersion specimen showing similar patterns as Figure 54 and evidence of the continued undercutting of the oxide film

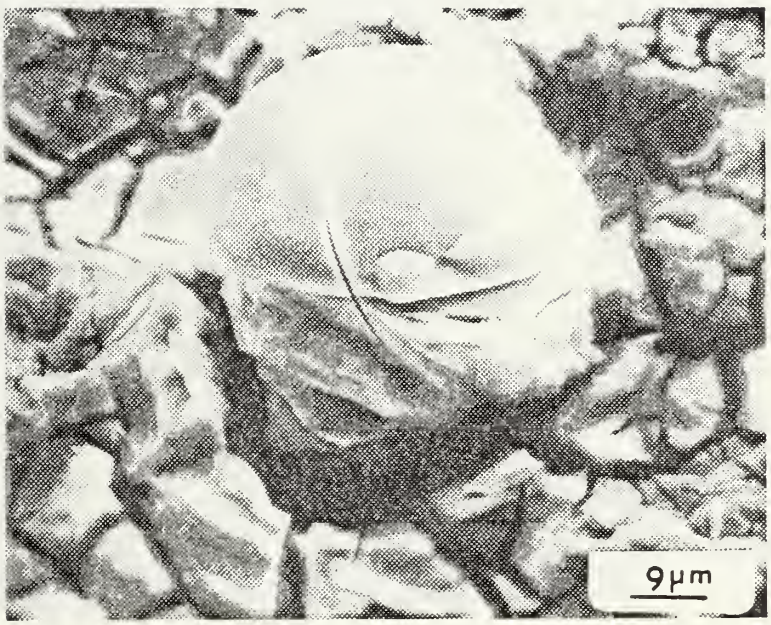

Figure 63

GI-96 (1150X) Corrosion product outcropping
on the Galvalum®I ninety-six-hour immersion specimen

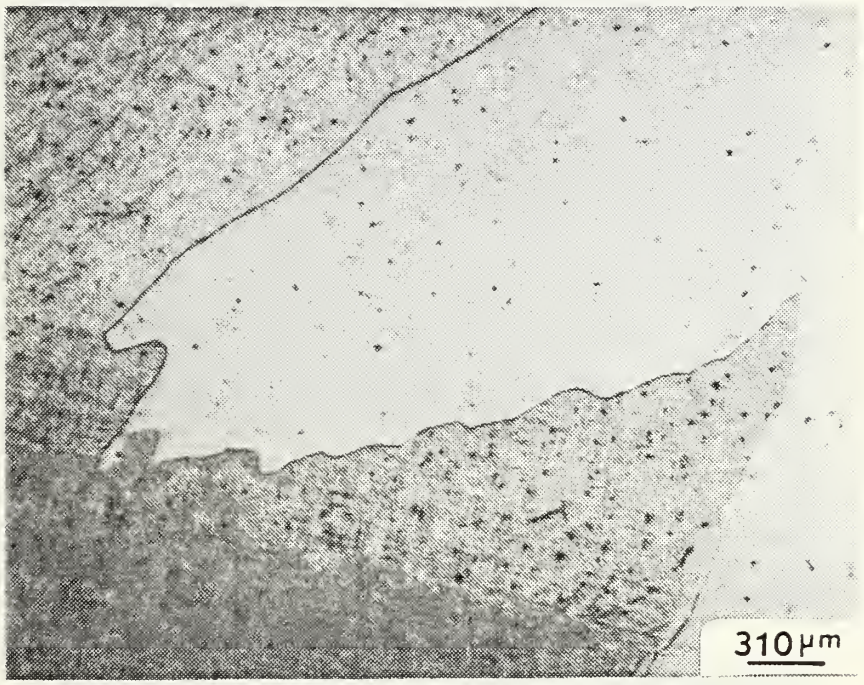

Figure 64

Galvalum®I specimen polished and etched
in 0.5% Hydrofluoric Acid

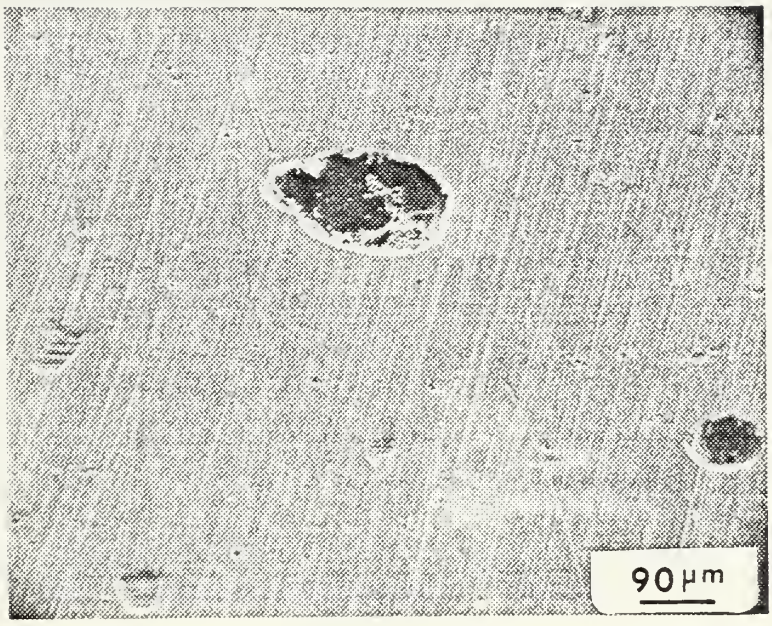

Figure 65

RII-0.25 (110X) Pitting on surface of Reynode® II aluminum anode specimen immersed for fifteen minutes

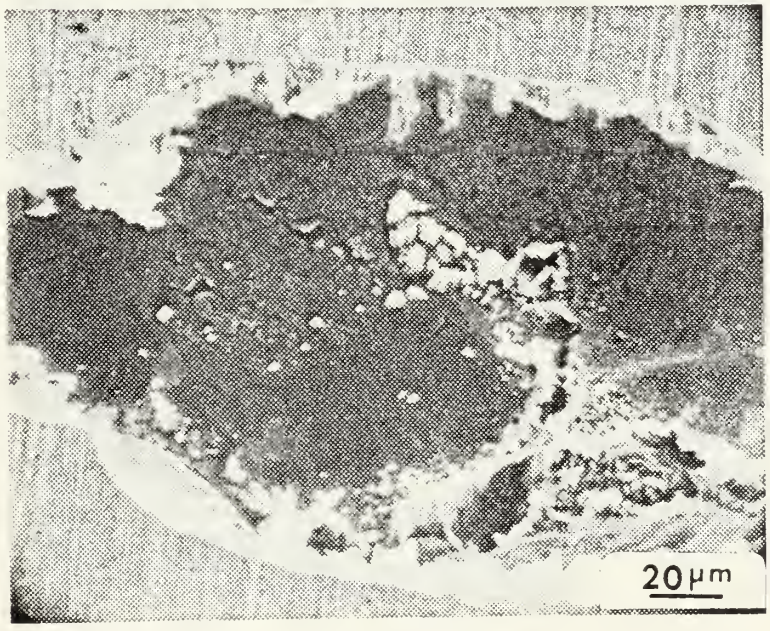

Figure 66

RII-0.25 (525X) Magnified view of pit in Figure 65

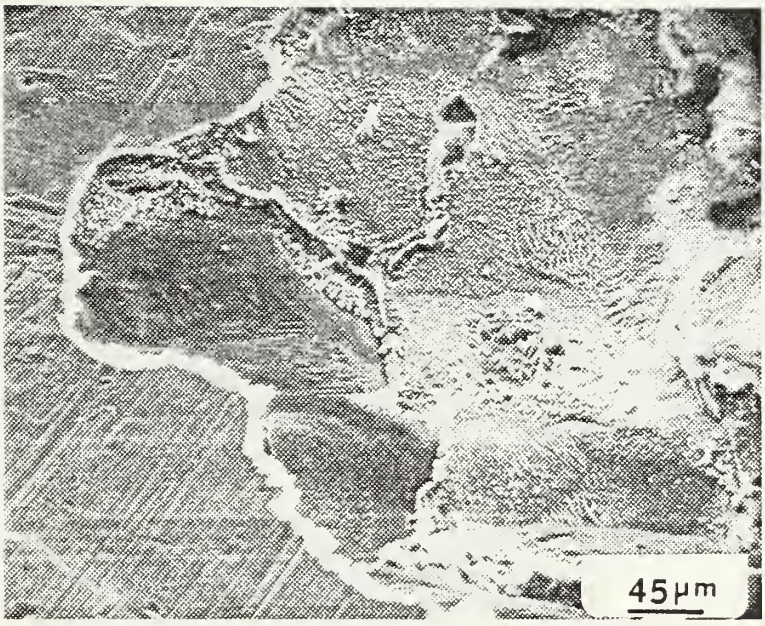

Figure 67

RII-0.5 (220X) Dissolution of Reynode®II aluminum sacrificial anode specimen that was galvanically coupled to HY-80 steel and immersed in artificial seawater for thirty minutes

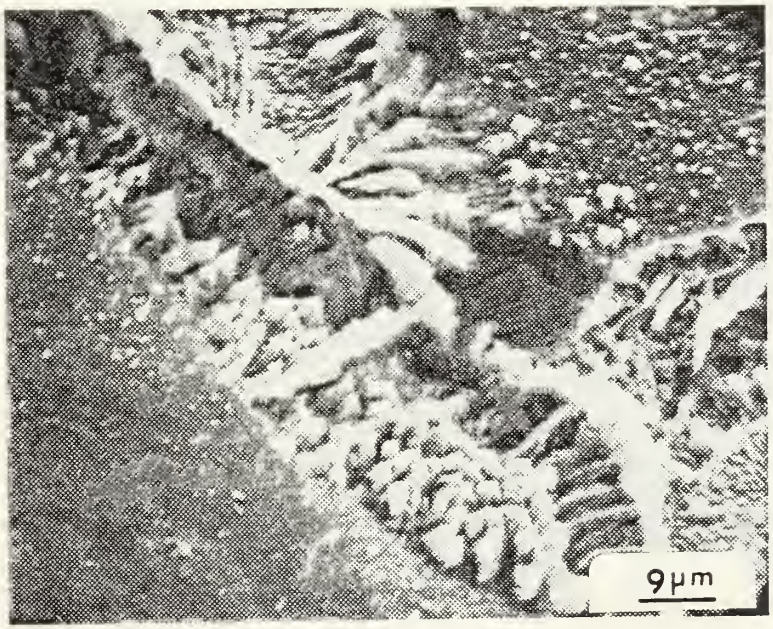

Figure 68

RII-0.5 (1100X) Magnified view of the grain boundary at left of center in Figure 67

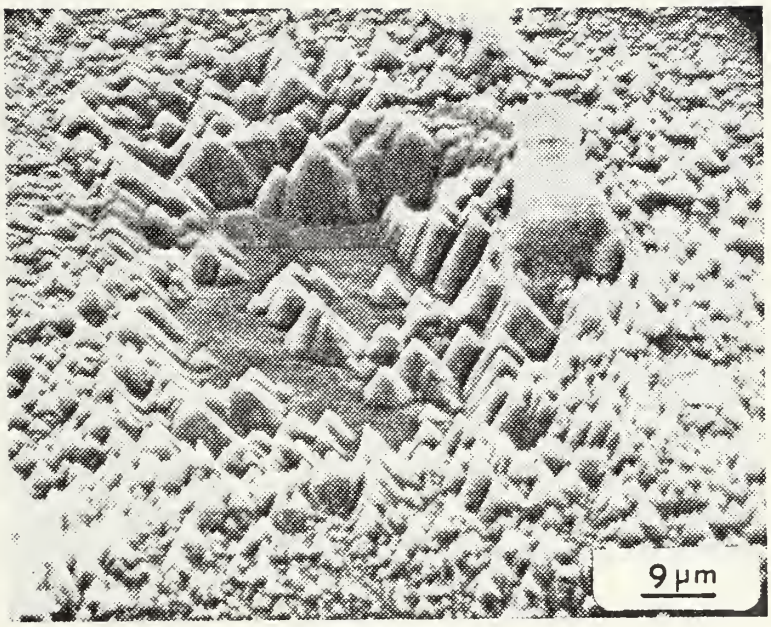

Figure 69

RII-0.5 (1100X) Magnified view of peaks in the grain to the right of center in Figure 67

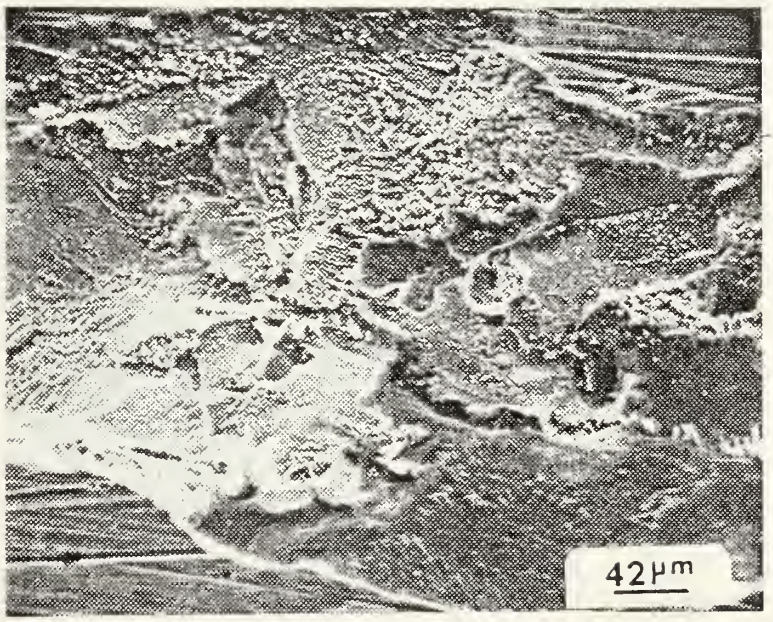

Figure 70

RII-1 (240X) Dissolution of Reynode®II aluminum sacrificial anode specimen that was galvanically coupled to HY-80 steel and immersed in artificial seawater for one hour

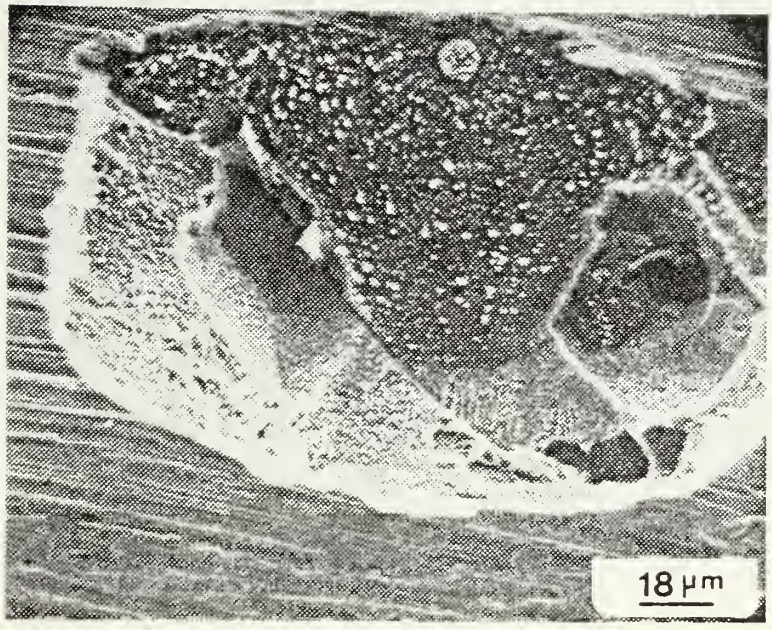

Figure 71

RII-1 (550X) Magnified view of dissolution cavity in the one-hour immersion specimen which illustrates varying rates of anodic dissolution of several grains

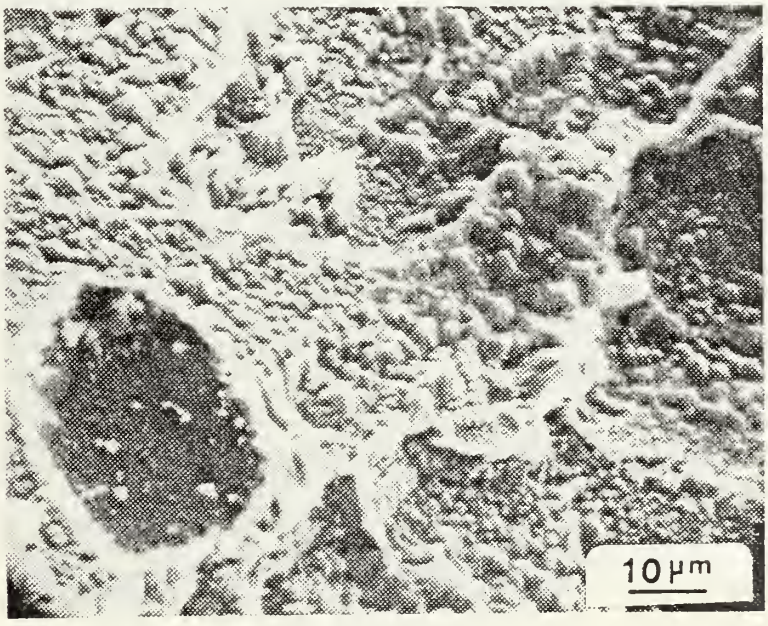

Figure 72

RII-1 (1100X) Dissolution cavity in the one-hour immersion specimen which illustrates the octahedral, or peak, formations, and variable dissolution rates of Reynode®II grains

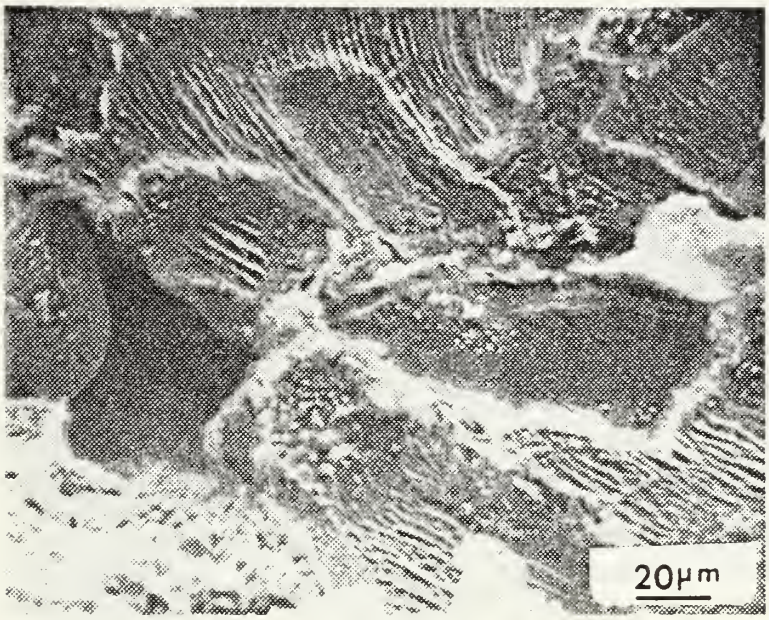

Figure 73

RII-2 (525X) Interior of dissolution cavity in two-hour immersion specimen of Reynode®II illustrating striations within separate grains

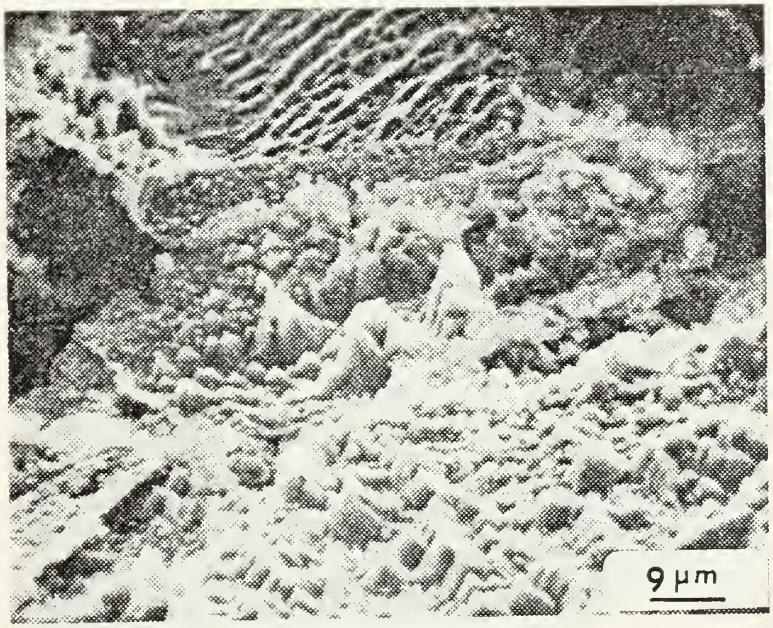

Figure 74

RII-2 (1100X) Peak formations on the two-hour immersion specimen of Reynode®II

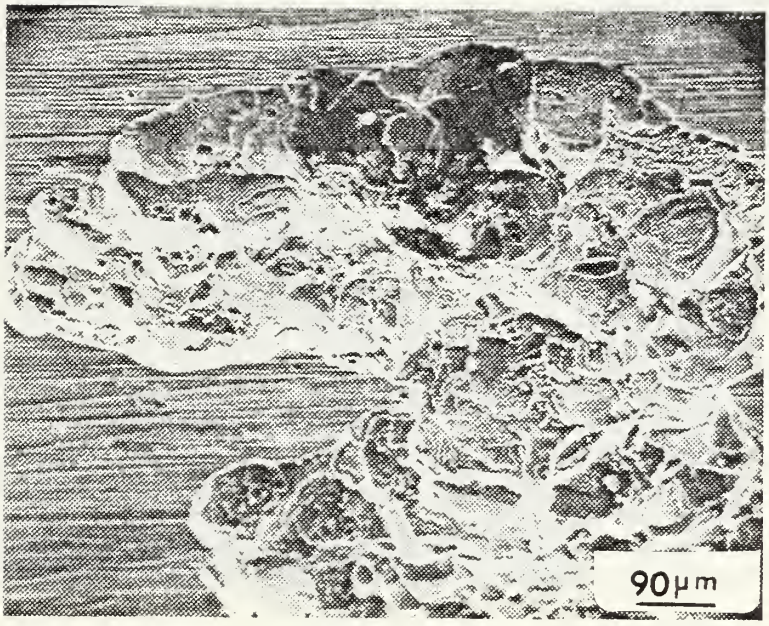

Figure 75

RII-4 (110X) Dissolution of Reynode®II aluminum sacrificial anode specimen that was galvanically coupled to HY-80 steel and immersed in artificial seawater for four hours

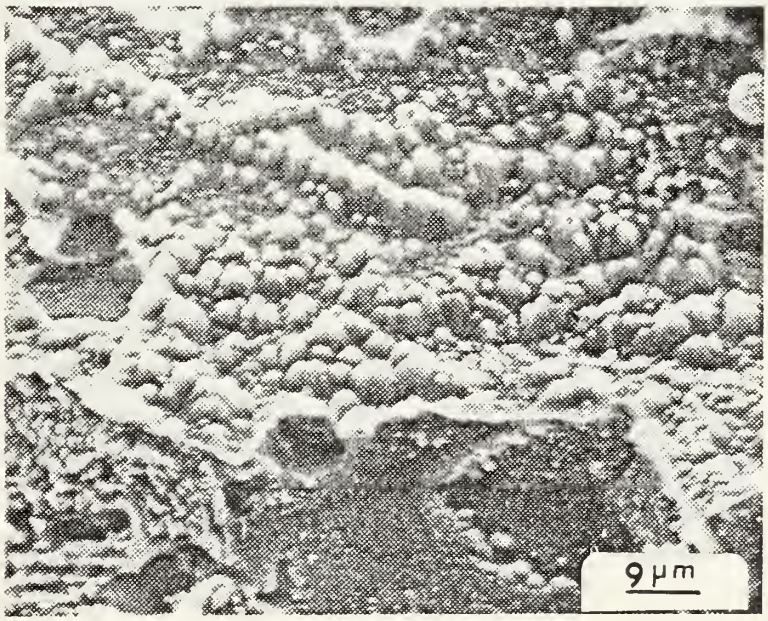

Figure 76

RII-4 (1050X) Magnified view of pit shown in Figure 75 illustrating more rounded octahedrons or peaks

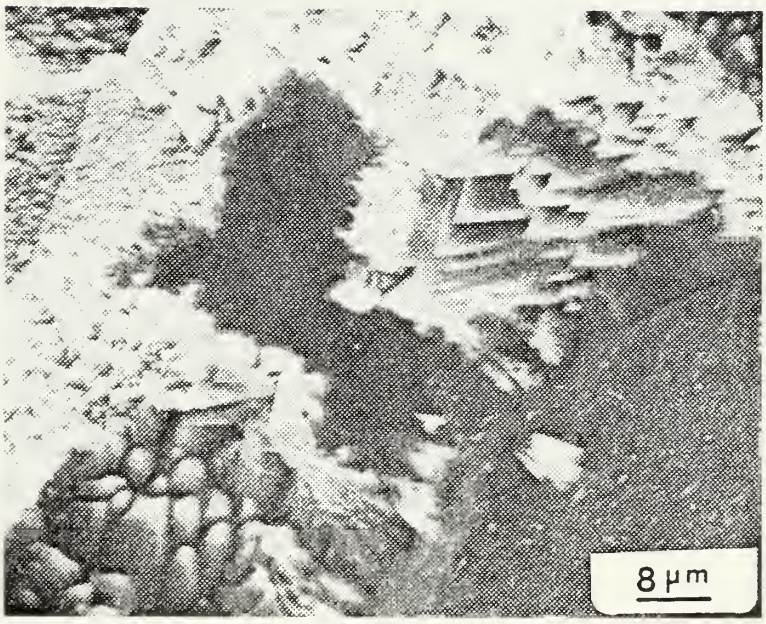

Figure 77

RII-4 (1200X) Four-hour immersion specimen illustrating varying anodic dissolution rates of separate grains and characteristic peaks

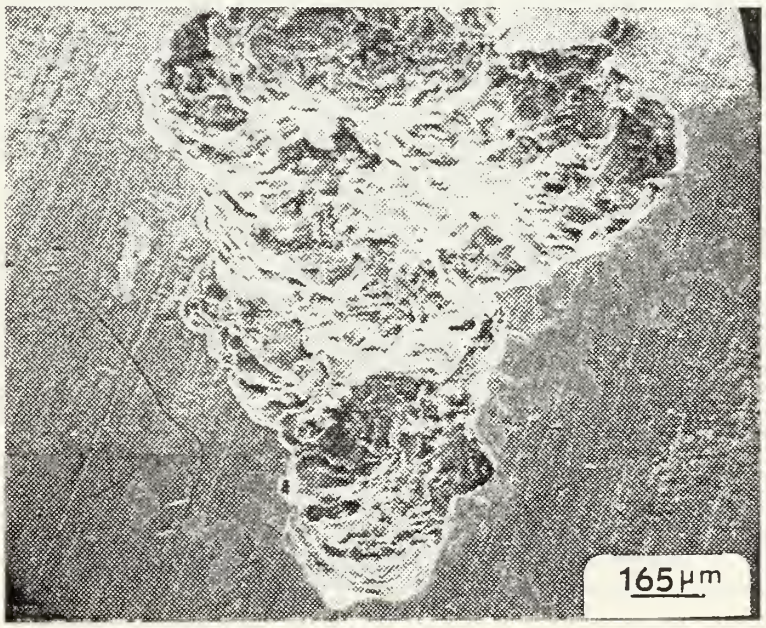

Figure 78

RII-8 (60X) Extensive dissolution cavity formation in an eight-hour immersion specimen of Reynode®II

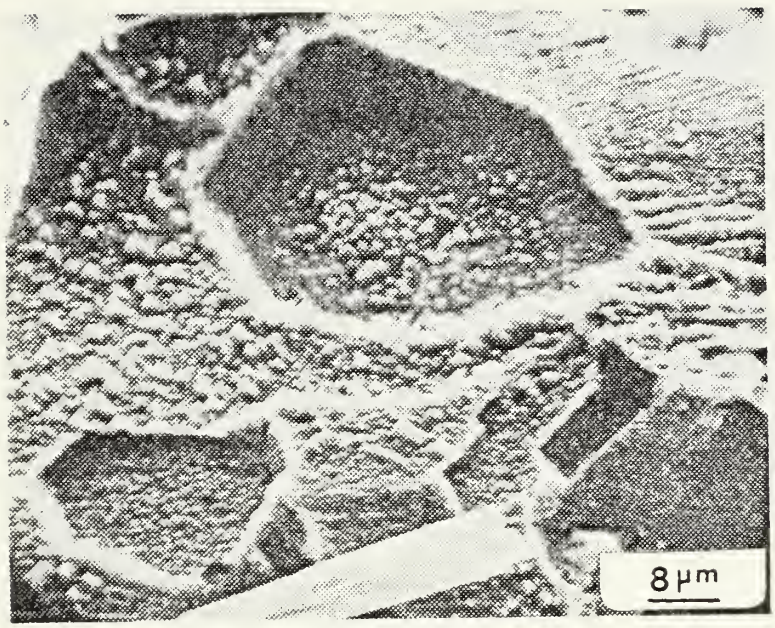

Figure 79

RII-8 (1150X) Evidence of different anodic dissolution rates of grains in Reynode®II eight-hour immersion specimen

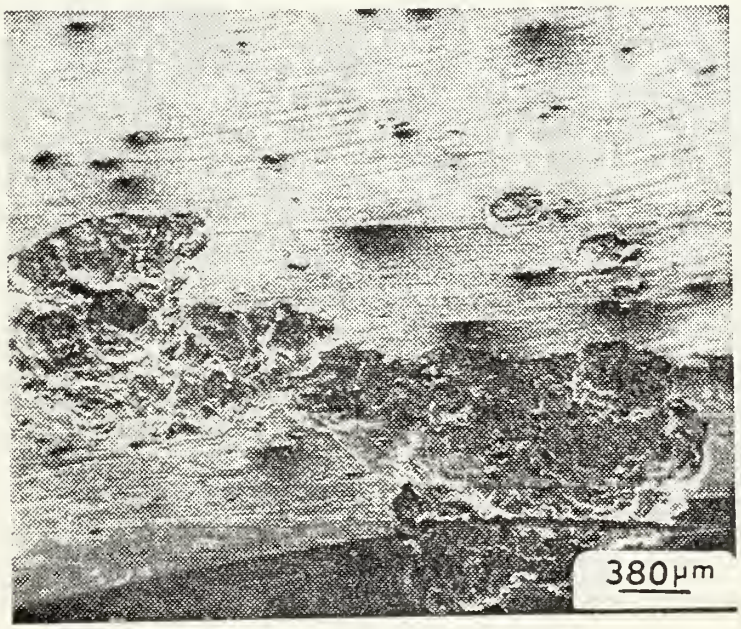

Figure 80

RII-24 (26X) Illustration of development of a dissolution region on the twenty-four-hour immersion specimen of Reynode®II

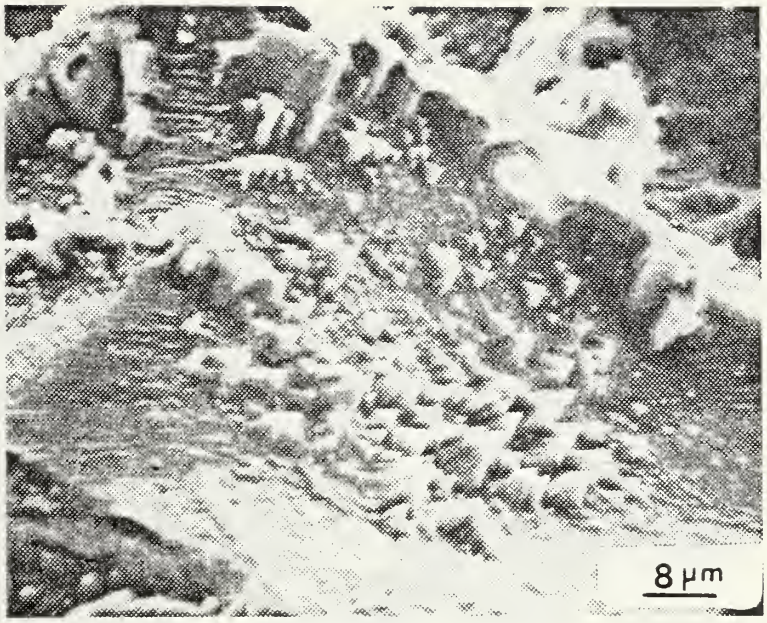

Figure 81

RII-24 (1200X) Characteristic peaks and grain boundary within dissolution cavity of twenty-four-hour immersion specimen of Reynode®II

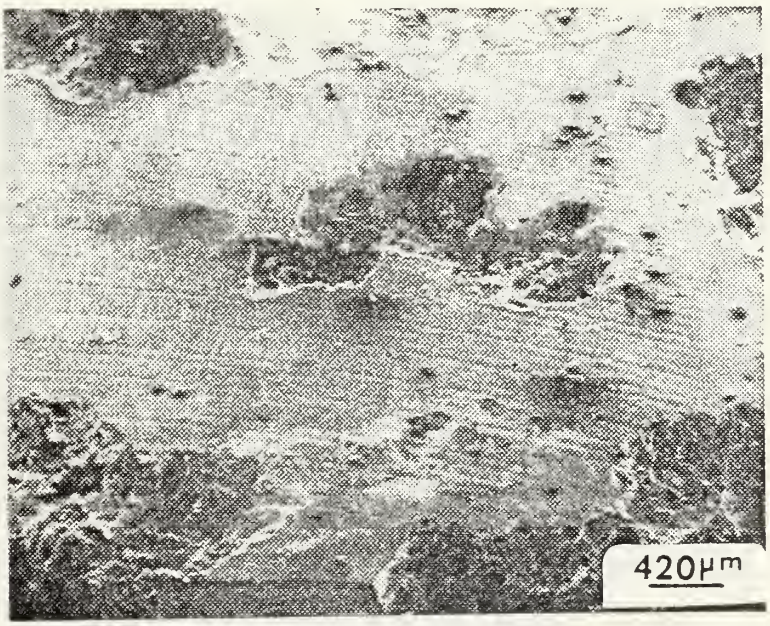

Figure 82

RII-48 (24X) Reynode®II specimen after forty-eight-hour immersion showing formation of dissolution cavities

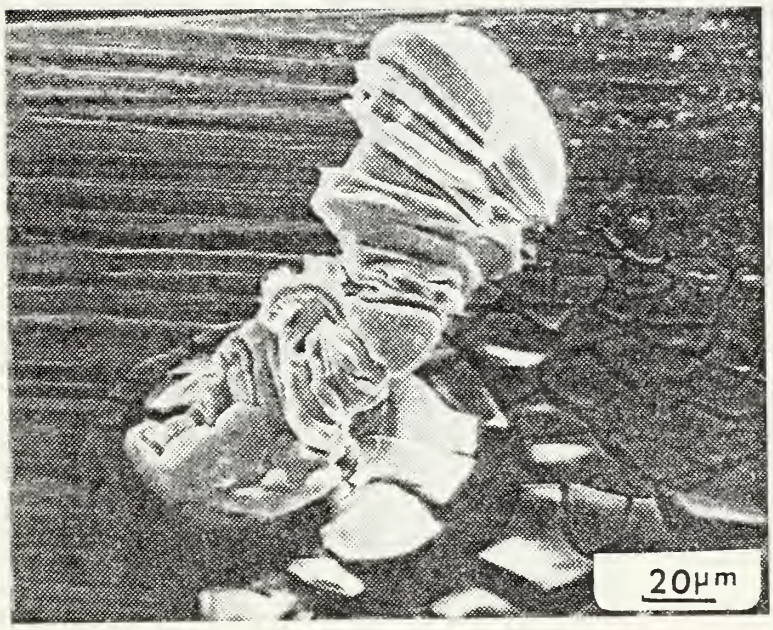

Figure 83

RII-48 (500X) Corrosion product tower emerging from pit on Reynode®II forty-eight-hour immersion specimen

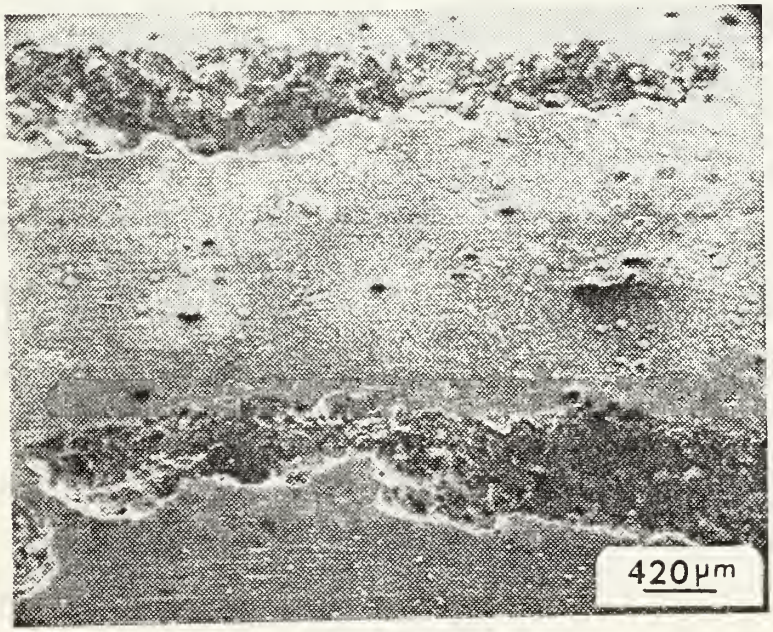

Figure 84

RII-72 (24X) Reynode®II specimen after seventy-two-hour immersion showing "wormpitting" vertically down the face of the specimen

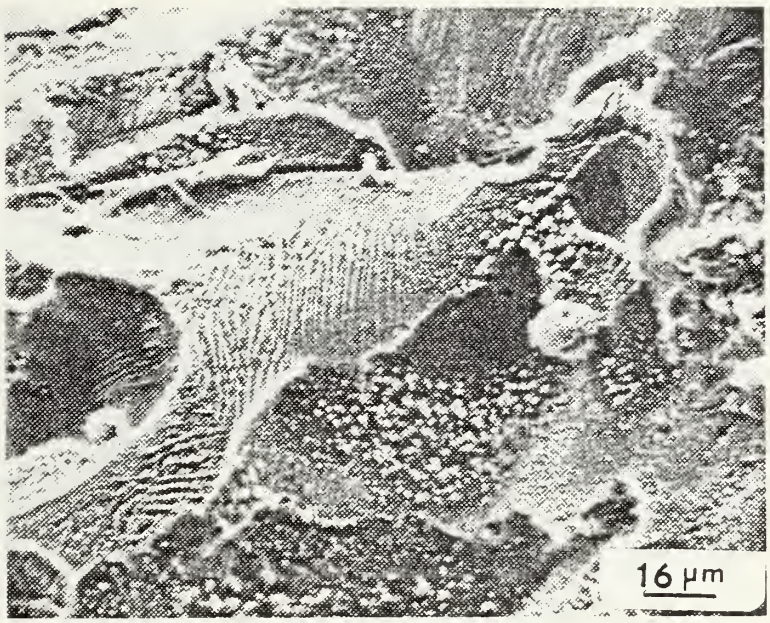

Figure 85

RII-72 (610X) Surface of dissolution region on Reynode®II seventy-two-hour immersion specimen showing striations and peaks in various grains

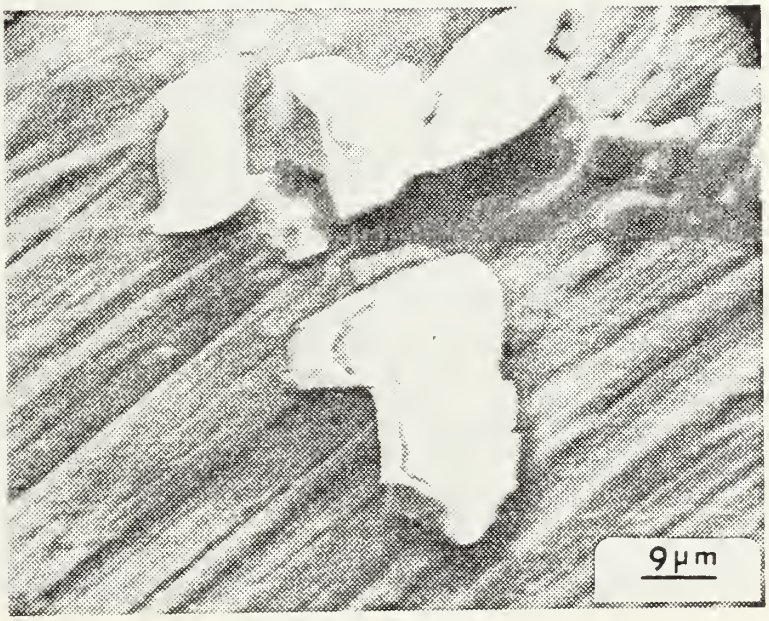

Figure 86

RII-96 (1100X) Corrosion product on surface of Reynode®II ninety-six-hour specimen which was analyzed with the X-ray spectrometer

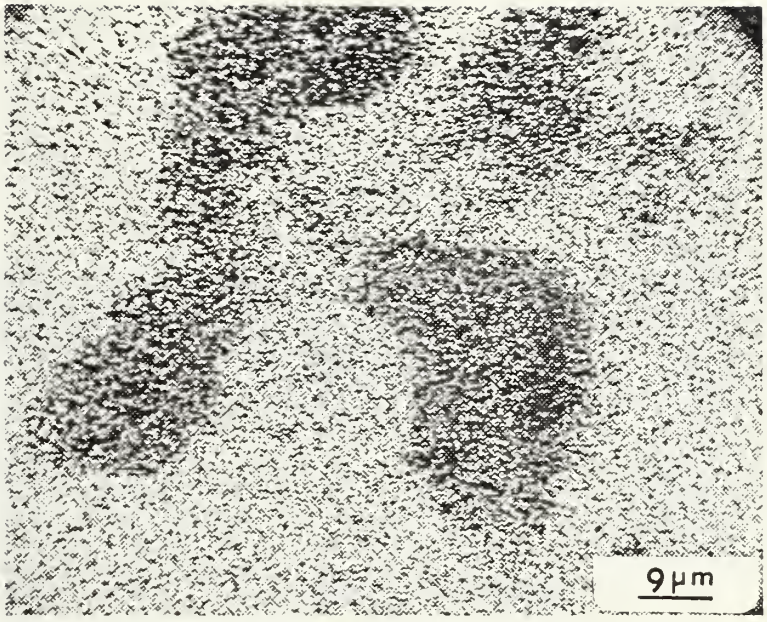

Figure 87

RII-96 (1100X) Aluminum dot map of corrosion product shown in Figure 86

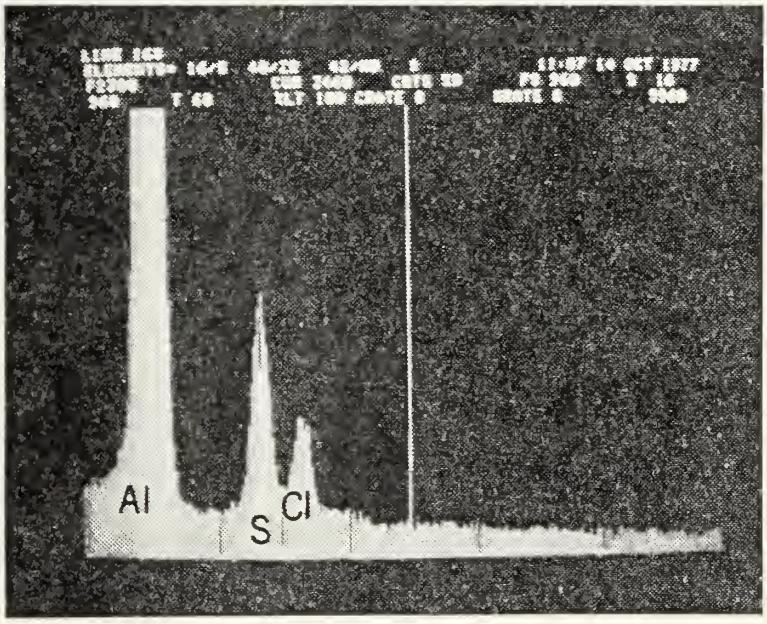

Figure 88

X-ray spectrum of corrosion product shown in Figure 86. The large peaks are (from the left) aluminum, sulfur and chlorine

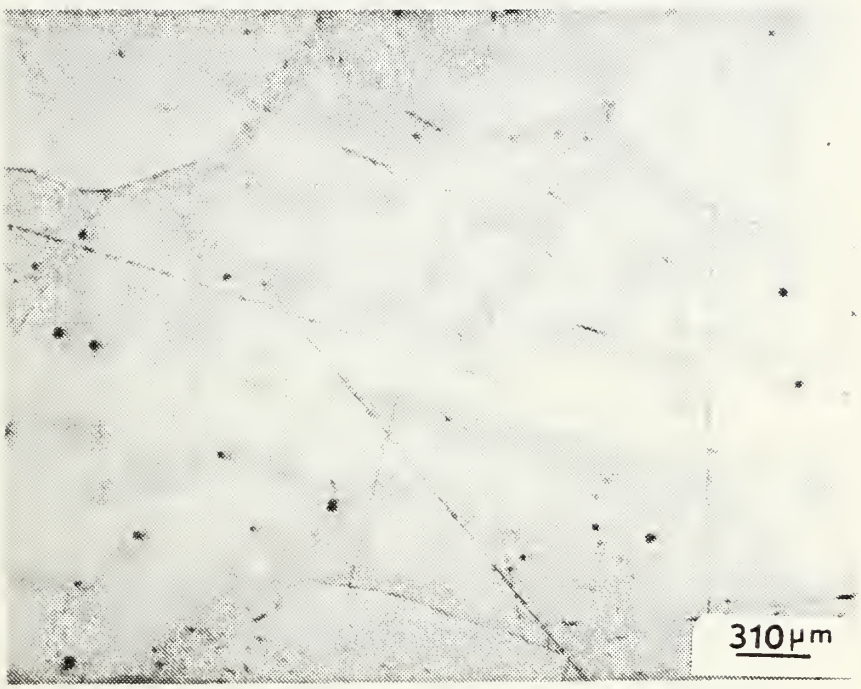

Figure 89

Base-metal microstructure of Reynode® II (32X), etched with 0.5% Hydrofluoric Acid. Note dendritic patterns in the grain.

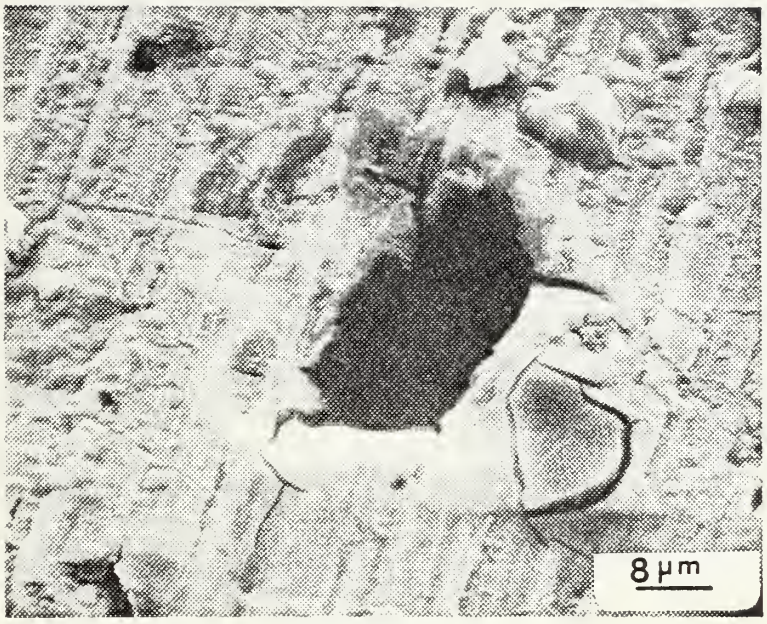

Figure 90

KA90-0.25 (1200X) Pit in the surface of KA-90® specimen immersed for fifteen minutes

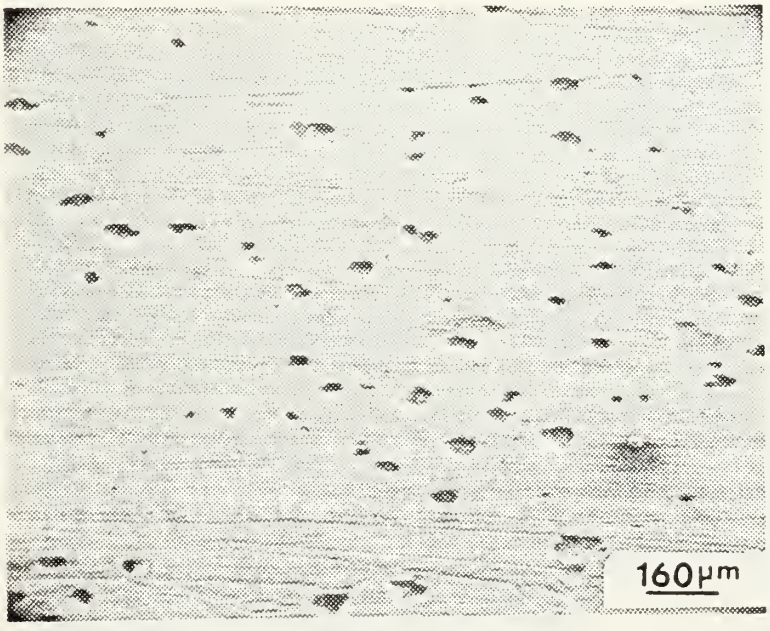

Figure 91

KA90-0.5 (60X) Pitting of a KA-90® aluminum sacrificial anode specimen that was galvanically coupled to HY-80 steel and immersed in artificial seawater for thirty minutes

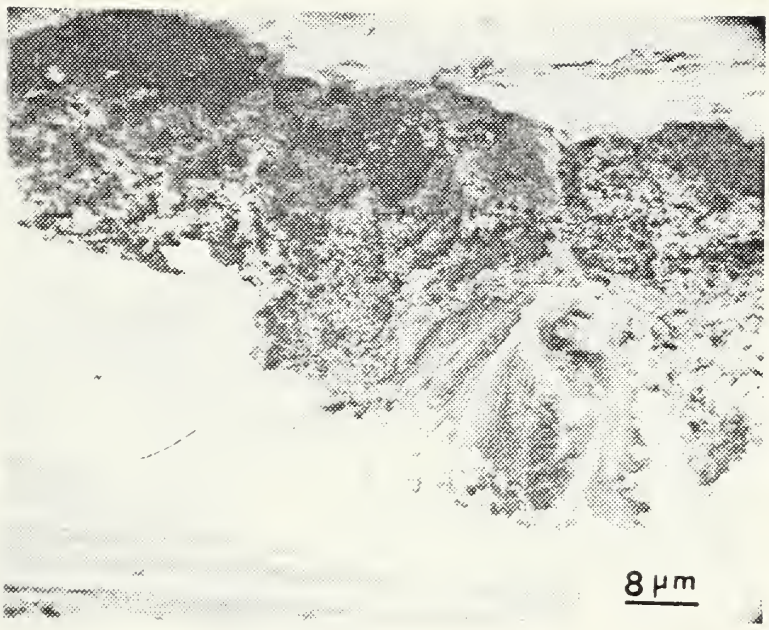

Figure 92

KA90-0.5 (1200X) Dissolution cavity in KA-90® thirty-minute specimen. Note evidence of surface undercutting and corrosion product buildup.

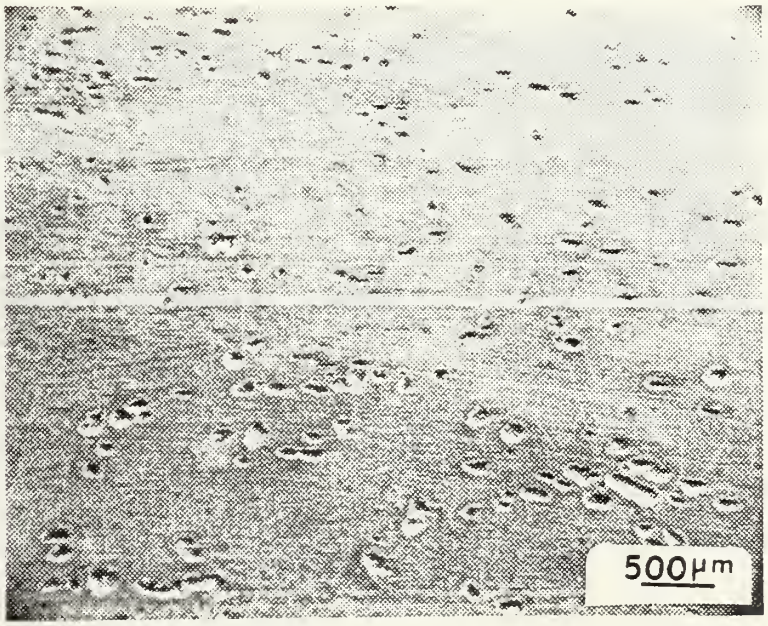

Figure 93

KA90-1 (20X) Pitting of KA-90® aluminum sacrificial anode specimen that was galvanically coupled to HY-80 steel and immersed in artificial seawater for one-hour

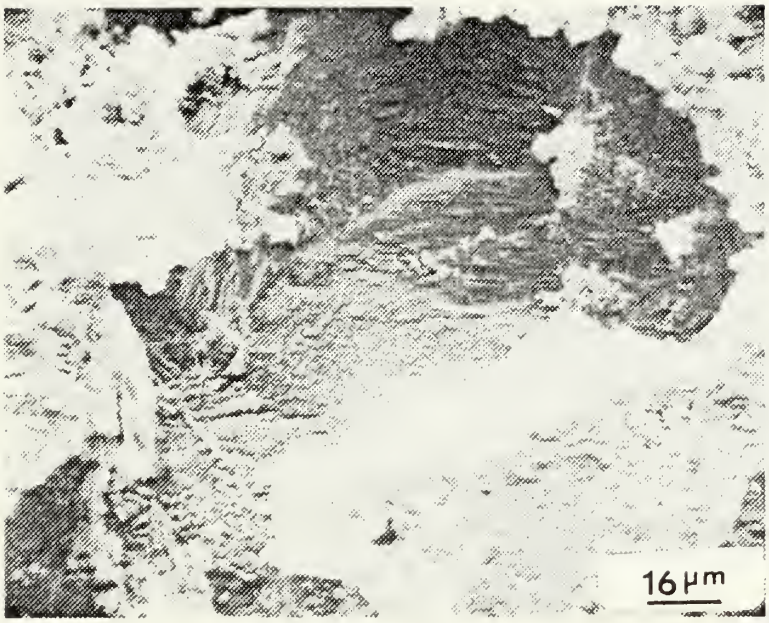

Figure 94

KA90-1 (610X) Magnified view of pit in surface of KA-90® one-hour immersion specimen

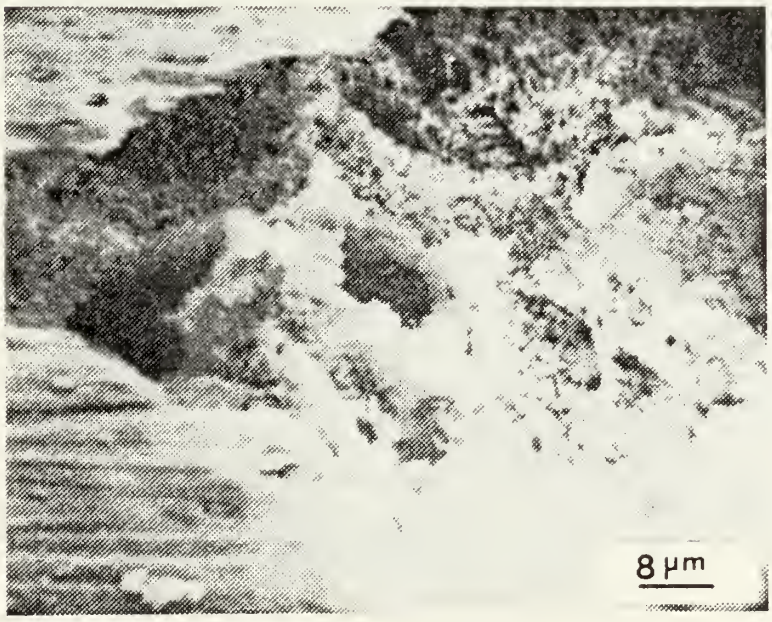

Figure 95

KA90-2 (1200X) Pit in surface of KA-90® two-hour immersion specimen evidencing corrosion product buildup

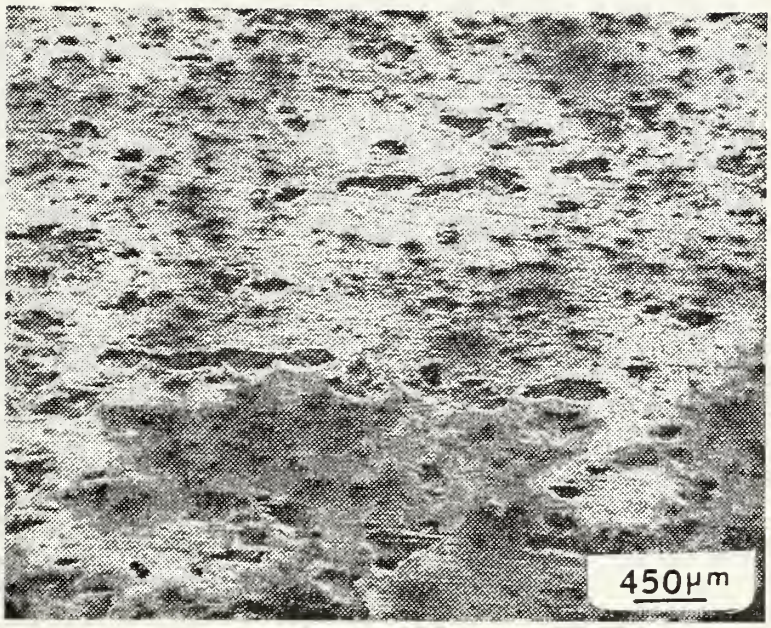

Figure 96

KA90-12 (22X) Distribution of pitting on KA-90® twelve-hour immersion specimen

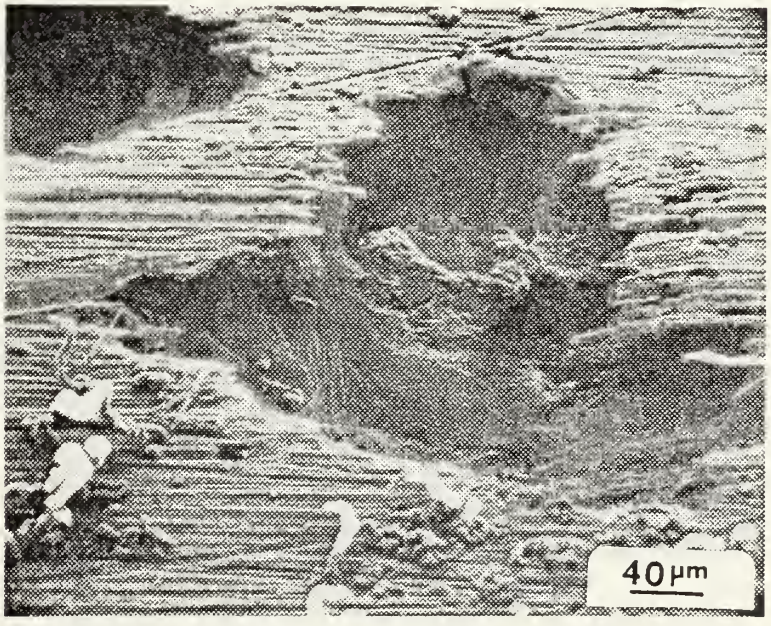

Figure 97

KA90-12 (240X) Evidence of pit growth and surface undercutting on KA-90® twelve-hour immersion specimen

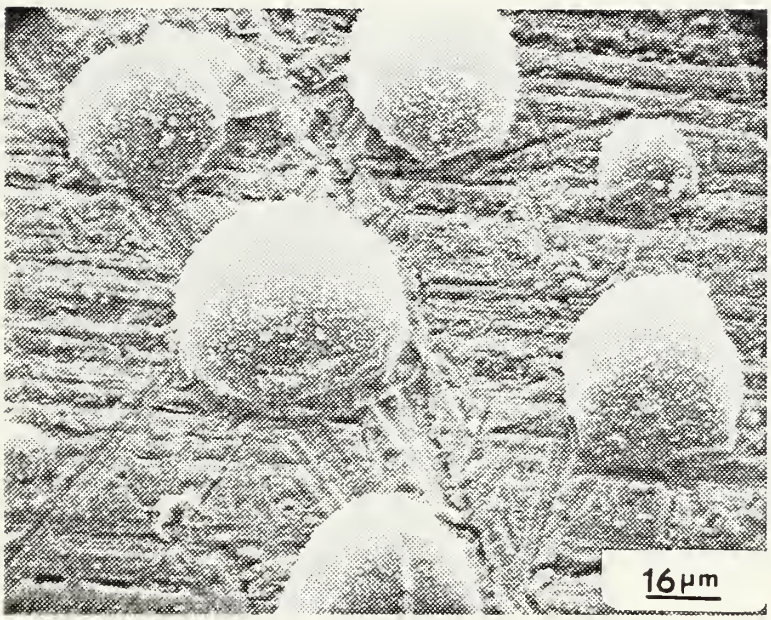

Figure 98

KA90-1 (610X) Hemispherical dome-like "pods" adhering to surface of KA-90® one-hour immersion specimen

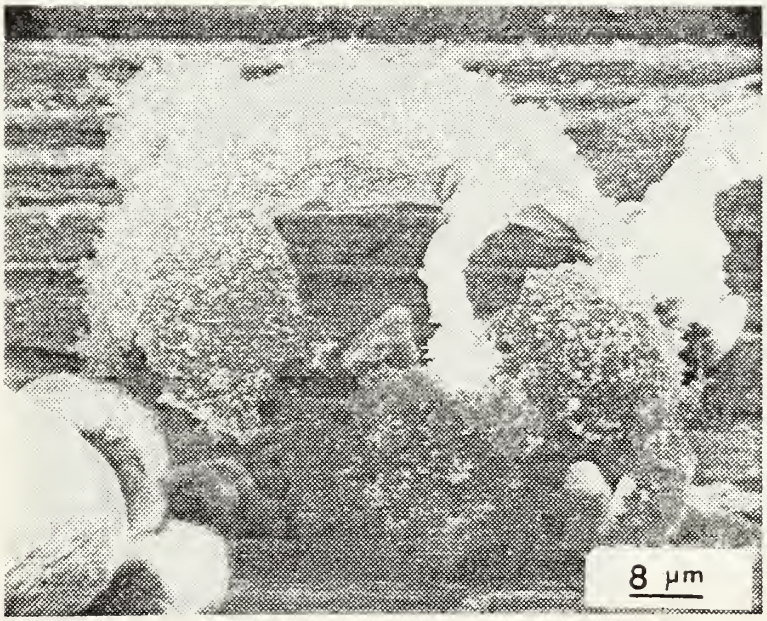

Figure 99

KA90-12 (1200X) Broken "pod" on surface of KA-90® twelve-hour immersion specimen

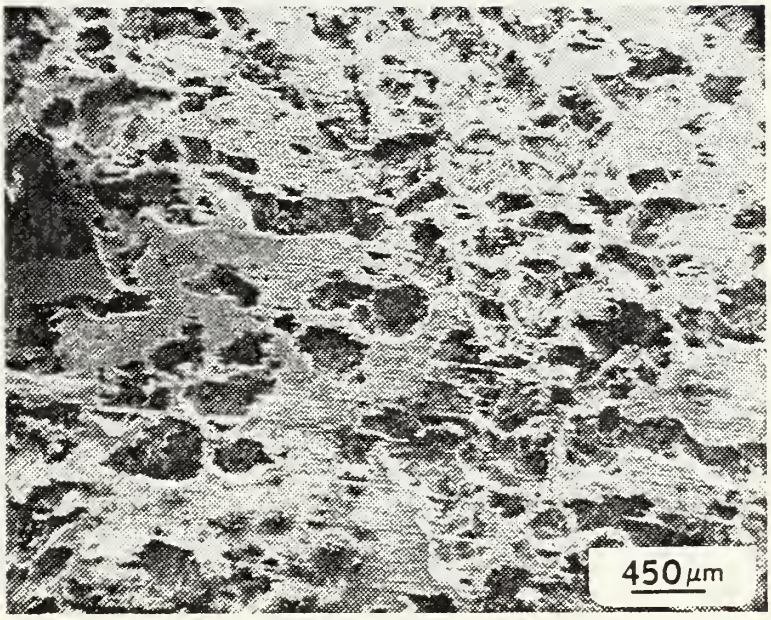

Figure 100

KA90-24 (22X) Pitting of KA-90®
twenty-four-hour immersion specimen

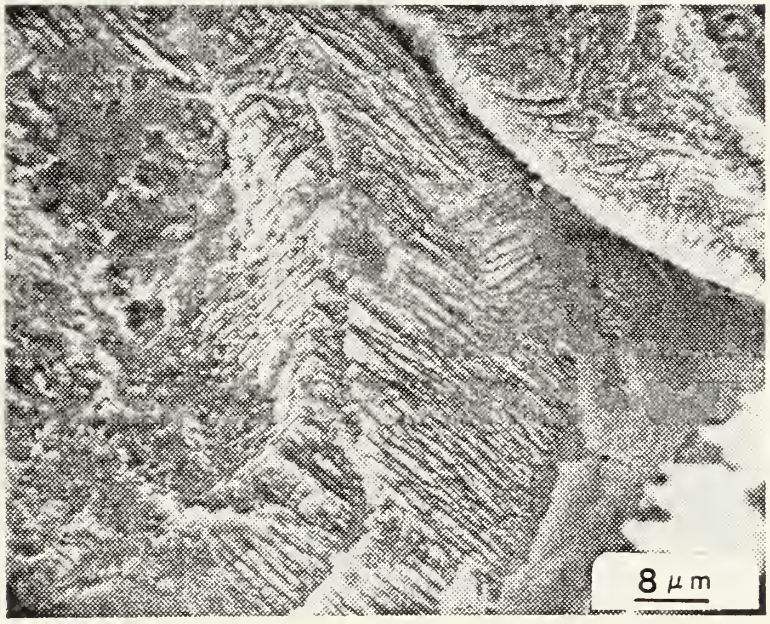

Figure 101

KA90-24 (1200X) Intergranular corrosion evidenced
in KA-90® twenty-four-hour immersion specimen

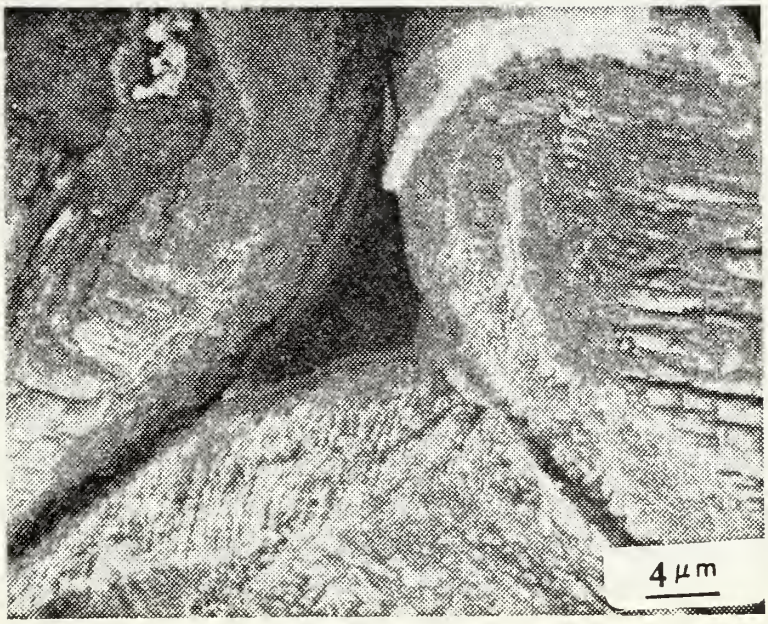

Figure 102

KA90-24 (2400X) Intergranular corrosion evidenced in KA-90® twenty-four-hour immersion specimen

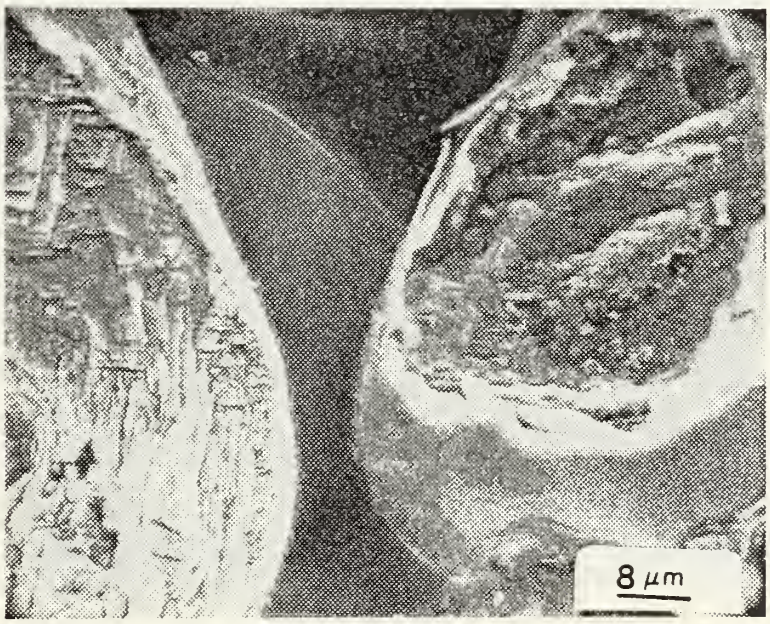

Figure 103

KA90-24 (1200X) Intergranular corrosion and grain encapsulation in a KA-90® twenty-four-hour immersion specimen

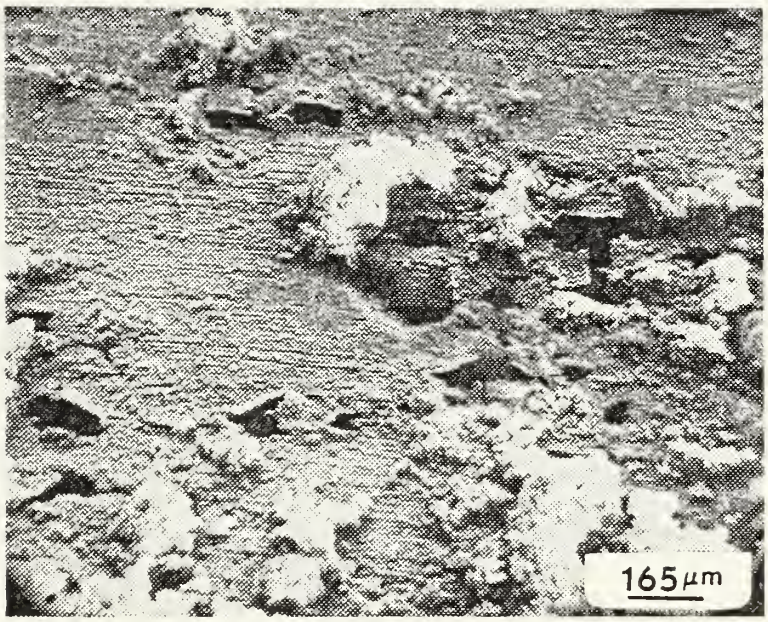

Figure 104

KA90-48 (60X) Accumulation of corrosion product around the pits on the surface of a KA-90® forty-eight-hour immersion specimen

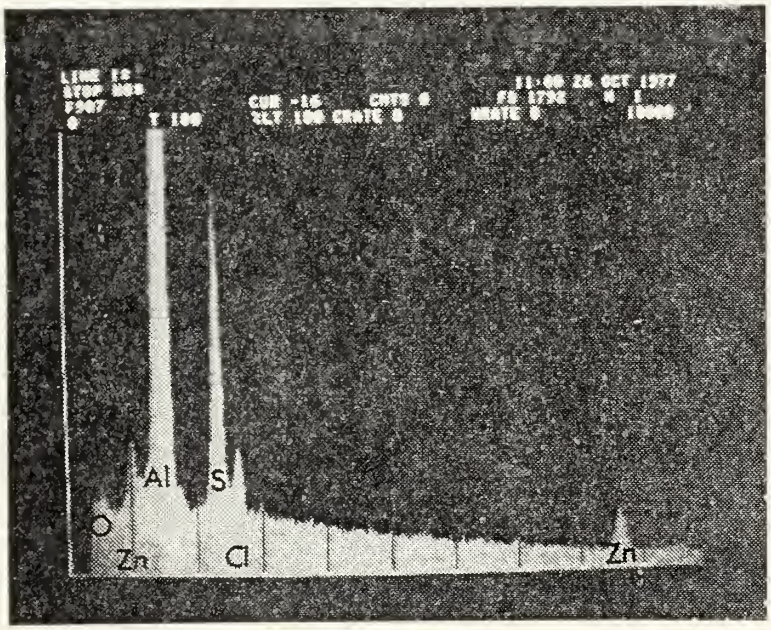

Figure 105

X-ray spectrum of corrosion product on a seventy-two-hour KA-90® immersion specimen

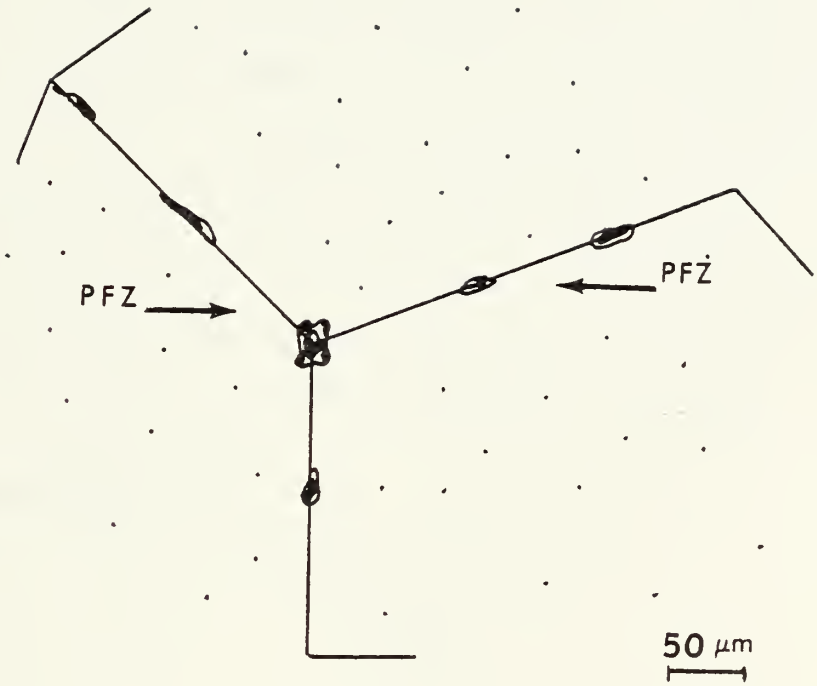

Figure 106

Sketch of base-metal microstructure of KA-90® aluminum sacrificial anode alloy (100X)

APPENDIX A

PREPARATION OF ARTIFICIAL SEAWATER

Synthetic standard seawater required during experimentation was prepared using the formula and procedure developed by Kester, et. al. [60]. A concentrated stock solution was initially produced for ease in handling prior to use.

The following amounts of gravimetric and volumetric salts, combined with enough distilled water for a total weight of 1 kilogram, were used per kilogram of synthetic seawater solution.

1. Gravimetric Salts

salt	g/kg of solution
NaCl	23.926
Na_2SO_4	4.008
KCl	0.677
$NaHCO_3$	0.196
KBr	0.098
H_3BO_3	0.026
NaF	0.003

2. Volumetric Salts

salt	Conc M/L	ml/kg of solution
$MgCl_2 \cdot 6H_2O$	1.000	53.27
$CaCl_2 \cdot 2H_2O$	1.000	10.33
$SrCl_2 \cdot 6H_2O$	0.100	0.90

3. Distilled water to bring total weight to 1 kilogram

The following is a comparison of the composition of natural and artificial seawaters by their ionic content:

Ion	Natural Seawater (g/kg)	Artificial Seawater (g/kg)	% Difference
Cl^-	19.353	19.353	0.0
Na^+	10.760	10.765	0.046
SO_4^{--}	2.712	2.711	0.037
Mg^{++}	1.294	1.295	0.077
Ca^{++}	0.413	0.414	0.24
K^+	0.387	0.387	0.0
HCO_3^-	0.142	0.142	0.0
Br^-	0.067	0.066	1.5
H_3BO_3	0.026	0.026	0.0
Sr^{++}	0.008	0.008	0.0
F^-	0.001	0.001	0.0

APPENDIX B

PROCEDURE DEVELOPED TO OBTAIN CONSISTENT RESULTS FROM THE PAR-331 CORROSION MEASUREMENT SYSTEM

In any scientific research program, the experimental procedures must be reproducible by other researchers and research facilities. When first attempting to use the PAR-331 system to obtain redundant results on the corrosion current of Galvalum®I, it became apparent that certain variations in operating procedures or specimen preparation were causing invalid data to be obtained. For instance, a given potentiodynamic polarization plot would show a corrosion potential of -0.5 volts (SCE), while the next plot would show a potential of -1.6 volts (SCE). This excessive degree of variation was overcome only after the procedures described in this appendix were developed. These procedures, which yield reliable, reproducible results, require that the following conditions be obtained:

A. Consistent specimen geometry;

B. Consistent specimen preparation;

C. Equipment cleanliness;

D. Consistent electrolyte preparation;

E. Proper electrode placement, and

F. Operational checks and balances.

It is this authors's intention to describe each of the items listed above so that the processes used during this

thesis research may be reproduced by others. Even though these procedures were used with aluminum samples, they are generally applicable to samples of other metals.

A. CONSISTENT SPECIMEN GEOMETRY

The recommended specimen geometry for the Princeton Applied Research Corrosion Measurement System is a right-circular cylinder with a height of 0.5 in. (1.27 cm) and a diameter of 0.375 in. (0.95 cm), with a hole drilled in one end to a depth of 0.25 in. (0.635 cm) and tapped to accept a 3-48 thread. The purpose of the right-circular cylinder geometry is to minimize edge effects and prevent directionalization of electric fields which might affect the polarization measurements. (Note that if it is not practical to obtain this recommended geometry, any specimen that will fit through the neck of the corrosion cell can be utilized.) The key to reproducibility is absolutely consistent geometry. The corrosion cell is illustrated in Figure B1 of this appendix.

In the present research, it was intended to examine the surface of various polarization specimens by scanning electron microscopy subsequent to various potentiostatically controlled exposures. For this duality of purpose, specimens must have dimensions of 0.375 in. (0.953 cm) height and diameter, with a 3-48 threaded hole tapped in the center of one end to a depth of 0.3125 in (0.794 cm). The surfaces of the specimens should be wet-sanded through at least 600 grit paper to remove machine marks.

B. CONSISTENT SPECIMEN PREPARATION

The following procedure was utilized to final-prepare and clean the specimen surfaces. The right-circular cylinders were polished with 000 grit paper to remove foreign particles and improve the surface. Final polishing was accomplished using a machine lathe set at 1000 rpm and polished for one minute. The specimens were then ultrasonically cleaned in acetone for five minutes, rinsed with deionized water and ethanol and blow-dried. Samples were placed in a covered plastic box until needed.

This procedure was always done on the day that a specific alloy was going to be tested to minimize atmospheric oxidation. Extra specimens were normally prepared to be used as "spares" in case additional polarization runs needed to be made; in this way, similarly prepared specimens were available.

C. EQUIPMENT CLEANLINESS

As with any experimental apparatus, cleanliness of the polarization cell is of paramount importance. In potentiodynamic corrosion studies this is particularly true because a small amount of contaminants in the electrolye may strongly affect the potentiodynamic curve. The corrosion cell and all of its associated components (gas sparger, sample holder, carbon rods) were initially cleaned with a good inorganic solubilizer (Micro®). Then the cell was ultrasonically cleaned, was rinsed with distilled water, and was rinsed with the electrolyte to be used in the experiment.

The associated components were subsequently rinsed with distilled water before each polarization run, and the cell was always cleaned as stated above prior to each subsequent polarization run.

D. CONSISTENT ELECTROLYTE PREPARATION

The corrosive medium (in this case, artificial seawater) was prepared by standard methods cited in Appendix A of this thesis. New (unused) electrolyte was utilized for each polarization run.

The corrosion cell was filled with electrolyte to a height of 3.5 in. (9.0 cm). The remaining components (except the specimen holder) were inserted into the cell, and all electrical connections were made. Nitrogen gas was then introduced into the electrolyte through the sparger. Once the nitrogen flow was regulated, the regulator valve was not touched until the end of a given series of four or more runs. The corrosion cell was placed on a magnetic stirrer, with a Nalgene® starhead magnetic stir bar used in the bottom of the cell. The stirring allows the nitrogen to mix with the electrolyte and deaerate it. This process was always carried on for five minutes prior to commencement of a polarization run.

E. PROPER ELECTRODE PLACEMENT

The placement of the Luggin electrode (combination salt bridge and calomel reference electrode) was critical. After the electrolyte was deaerated, stirring was stopped; and

the electrolyte allowed to become quiescent. The specimen holder was then inserted into the corrosion cell. A nominal time of two minutes was established as the time between specimen insertion in the electrolyte and commencement of a polarization run. The basic requirement of this particular step was that this pre-immersion time, prior to polarization, be consistent and long enough to allow the operator time to place the Luggin electrode next to the specimen.

The Luggin electrode was placed within 1 mm of the specimen, established from information obtained in Ref. 61, to eliminate difficulties associated with ion diffusivity and IR drop.

F. OPERATIONAL CHECKS AND BALANCES

In any experimental operation that requires a multiplicity of instrumental adjustments (knob turning and switch positioning), chances for error are compounded, as illustrated in photographs of the instrumentation shown in Figures B2 and B3. In order to avoid this type of error, a checklist type operational procedure was employed, using the checklist included in the PAR-331 operating manual.

Specific parameters were established for each polarization run. These were: (1) Potentiodynamic scan rate was set at 1.0 mV/sec, and (2) the potential axis was calibrated at 0.2 volts per major division.

It is believed that the use of a reproducible time of two minutes between immersion and the start of a potentiodynamic

run was the most critical factor necessary to obtain consistent data. This is because the specimen, when immersed in the electrolyte, begins to corrode freely so that its surface chemistry is constantly changing. Therefore, by starting each run at the same time, the surfaces of the different specimens were in reasonably similar conditions at the start of the runs.

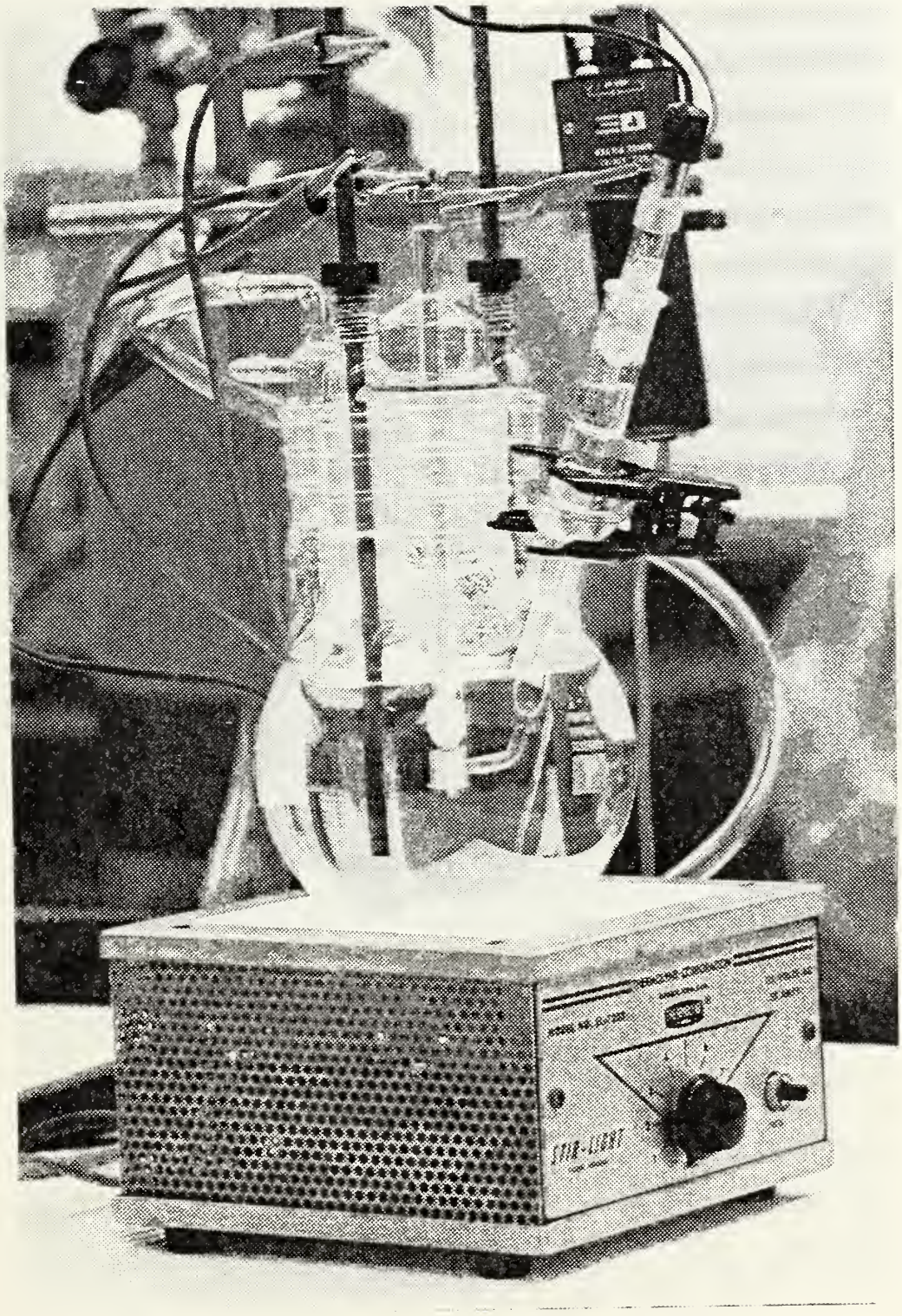

Figure B1

Corrosion cell and ancillary attachments
atop magnetic stirring mechanism

Figure B2

Princeton Applied Research
Model-331, Deluxe Corrosion
Measurement System

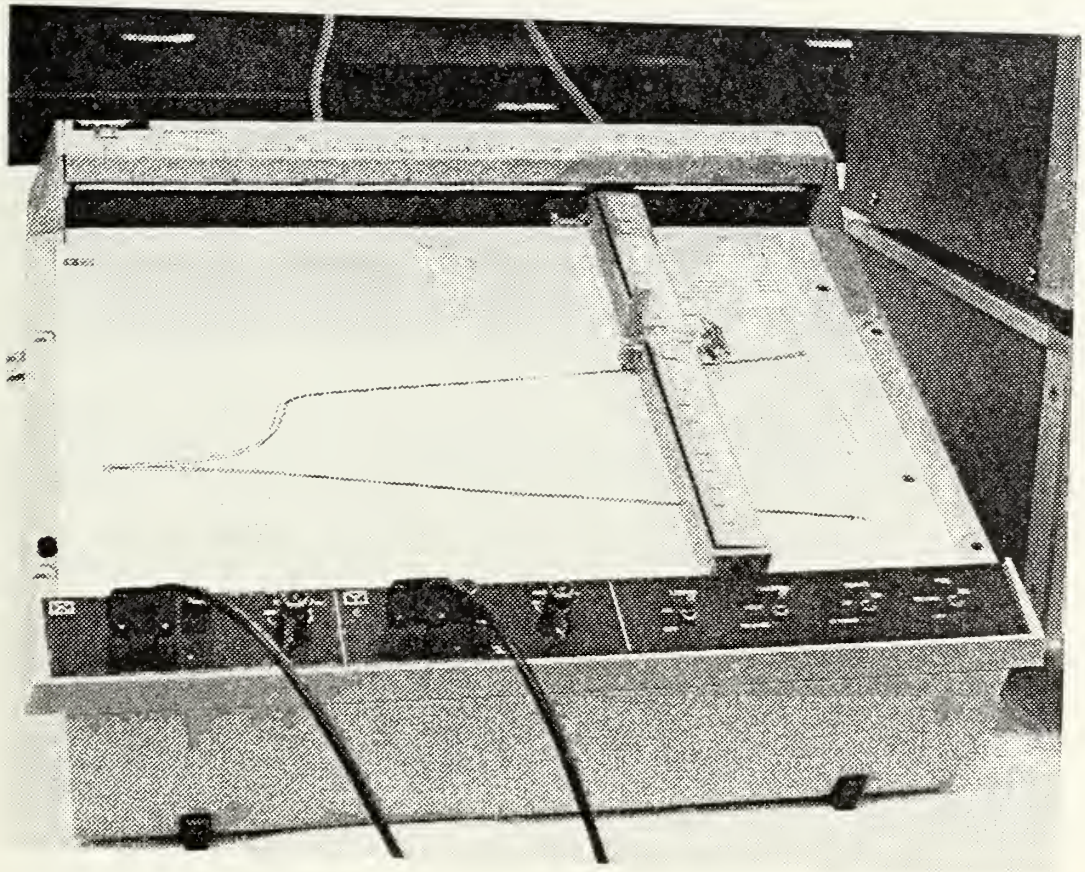

Figure B3

Hewlett-Packard Model 7040A, X-Y Recorder

LIST OF REFERENCES

1. Francis, R.C. and Cook, F.E., "Economics of Cathodic Protection for U.S. Navy Ships", Materials Protection, p. 16-26, February 1962.

2. Military Specification MIL-A-18001H, Anodes, Corrosion Prevention, Zinc; Slab, Disc and Rod Shaped, 28 June 1968.

3. Perkins, J., Luebke, W.H., Graham, K.J. and Todd, J.M., "Anodic Corrosion of Zinc Alloys in Sea Water", Journal of the Electrochemical Society, V. 124, No. 6, p. 819-826, June 1977.

4. Perkins, J. and Bornholdt, R.A., "The Corrosion Product Morphology Found on Sacrificial Zinc Anodes", Corrosion Science, V. 17, p. 377-384, 1977.

5. Private communication with W. Strasburg, Naval Ship Engineering Center, November 1977.

6. Reding, J.T. and Newport, J.J., "The Influence of Alloying Elements on Aluminum Anodes in Sea Water", Materials Protection, p. 15-18, December 1966.

7. Schrieber, C.F. and Reding, J.T., "Field Testing a New Aluminum Anode", Materials Protection, p. 33-36, May 1967.

8. Keir, D.S., Pryor, M.J. and Sperry, P.R., "Galvanic Corrosion Characteristics of Aluminum Alloyed with Group IV Metals", Journal of the Electrochemical Society, p. 777-782, August 1967.

9. Lennox, T.J., Jr., Peterson, M.H. and Groover, R.E., "A Study of Electrochemical Efficiencies of Aluminum Galvanic Anodes in Sea Water", Materials Protection, p. 33-37, February 1968.

10. Birnbaum, L.S., Taylor, B.M. and Strasburg, W.M., Jr., "Cathodic Protection", Naval Engineers Journal, p. 13-24, April 1971.

11. Jensen, F.O., "Corrosion and Protection of Offshore Steel Structure", Paper #182, presented at the National Association of Corrosion Engineers Convention, Houston, Texas, March 22-26, 1976.

12. Rachlot, B., "Sacrificial Anode Alloys -- Their Specifications and Uses", Proceedings of the Second International Congress on Metallic Corrosion, NACE, p. 285-289, 1966.

13. Mackay, W.B., "Deep Water Testing of Sacrificial Anodes", Materials Performance, p. 36-40, August 1974.

14. Mackay, W.B., "Deep Water Testing of Sacrificial Anodes (Part 2)", Materials Performance, p. 39-43, December 1975.

15. Russell, G.I. and Banach, J., "Selection of Anode Systems for Cathodic Protection in Natural Waters", Materials Performance, p. 18-23, August 1971.

16. Sakano, T., Toda, K. and Hanada, M., "Tests on the Effects of Indium for High Performance Aluminum Anodes", Materials Protection, p. 45-50, December 1966.

17. Kurr, G.W., "Sacrificial Anode Applications in Ships", Materials Protection, p. 3-7, November 1969.

18. Haney, E.G. and Kurr, G.W., "Sea Water Efficiency Tests on Aluminum Alloy Anodes Containing Zinc, Indium and Cadmium", Materials Performance, p. 27-30, May 1976.

19. Grandstaff, C.M., Schwertzer, J.N., Craig, H.L., Jr., and Compton, K.G., "Performance Evaluation of Quality Aluminum Anodes in Sea Water", Paper #110, presented at the National Association of Corrosion Engineers Convention, Chicago, Illinois, March 4-8, 1974.

20. Compton, K.G., "Cathodic Protection of Structures in Sea Water", Paper #13, presented at the National Association of Corrosion Engineers Convention, Toronto, Ontario, Canada, April 14-18, 1975.

21. Doremus, G.L. and Davis, J.G., "Marine Anodes: The Old and New, Cathodic Protection for Offshore Structures", Materials Protection, p. 30-34, January 1967.

22. Doremus, G.L. and Davis, J.G., "Modern Approach to Cathodic Protection of Offshore Pipelines", Pipeline Engineer, p. 36-45, October 1969.

23. Doremus, E.P. and Bass, R.B., "Cathodic Protection of 516 Offshore Structures - Engineering Design and Anode Performance", Materials Protection and Performance, p. 23-27, May 1971.

24. Davis, J.G., Doremus, E.P. and Bass, R.B., "New Aspects of the Application of Cathodic Protection to Offshore Facilities", Materials Performance, p. 9-15, September 1975.

25. Rizzo, F.E. and Bauer, E., "Cathodic Protection Current Distribution on Offshore Platforms", Paper #31, presented at the National Association of Corrosion Engineers Convention, San Francisco, California, March 14-18, 1977.

26. Johnson, D.L., "Diver Installed Anode Replacement Systems for Offshore Structures", Paper #32, presented at the National Association of Corrosion Engineers Convention, San Francisco, California, March 14-18, 1977.

27. Reding, J.T., "Sacrificial Anodes for Ocean Bottom Applications", Materials Protection and Performance, p. 17-19, October 1971.

28. Reding, J.T. and Boyce, T.D., "Cathodic Protection Performance of Offshore Anodes at a Simulated Depth of 600 Feet", Paper #111, presented at the National Association of Corrosion Engineers Convention, Chicago, Illinois, March 4-8, 1974.

29. Smith, S.N., Reding, J.T. and Riley, R.L., Jr., "Development of a Broad Application Saline Water Aluminum Anode -'Galvalum'III", Paper #180, presented at the National Association of Corrosion Engineers Convention, Houston, Texas, March 22-26, 1976.

30. Smith, S.N., Schrieber, C.F. and Riley, R.L., Jr., "Supplementary Studies of the Galvalum III Anode - Exposure Time and Low Temperature", Paper #35, presented at the National Association of Corrosion Engineers Convention, San Francisco, California, March 14-18, 1977.

31. Lennox, T.J., "Electrochemical Properties of Magnesium, Zinc and Aluminum Galvanic Anodes in Sea Water", Proceedings, Third International Congress on Marine Corrosion and Fouling, p. 176-190, October 1972.

32. Naval Research Laboratory Memorandum Report 2300, The Electrochemical Characteristics of Aluminum Galvanic-Anode Alloys in Sea Water, by T.J. Lennox, Jr., R.E. Groover and M.H. Peterson, June 1971.

33. Naval Research Laboratory Report 7648, The Effect of Mercury and Tin from Aluminum Galvanic Anodes on the Corrosion Characteristics of 5086-H34 and 6061-T6 Aluminum Alloys in Sea Water, by T.J. Lennox, Jr., R.E. Groover and M.H. Peterson, November 16, 1973.

34. Peterson, M.H., Lennox, T.J., Jr., and Groover, R.E., The Effect of Initial Low Anode Current Densities on the Subsequent Performance of Galvanic Anodes, paper presented at the National Association of Corrosion Engineers Convention, Toronto, Ontario, Canada, April 14-18, 1975.

35. Military Specification (Preliminary), Anodes, Corrosion Preventive, Aluminum, draft of 1 November 1974, prepared under project No. 5340-N060.

36. Wright, P.W., "A Scanning Electron Microscope Study of the Corrosion of Sacrificial Hull Anodes Under Simulated Ships Service Conditions", MSME Thesis, Naval Postgraduate School, December 1976.

37. Private communication with Mr. Ray Lindberg of Reynolds Metal Company, March 1977.

38. Private communication with Mr. Jack Schrear of Kaiser Magnesium Company, April 1977.

39. Leroy, R.L., "Evaluation of Corrosion Rates from Polarization Measurement", Corrosion - NACE, V. 31, No. 5, p. 173-177, May 1975.

40. Morris, P.E. and Scarberry, R.C., "Predicting Corrosion Rates with the Potentiostat", Corrosion - NACE, V. 28, No. 12, p. 444-452, December 1972.

41. "The Reproducibility of Potentiostatic and Potentiodynamic Anodic Polarization Measurements", an ASTM G-1/X1 Inter-laboratory Testing Program, prepared by ASTM Committee G-1, Subcommittee X1, Task Group 2, Materials Research Standards, p. 25-26, September 1969.

42. National Association of Corrosion Engineers Standard TM-01-69, Test Method: Laboratory Corrosion Testing of Metals for the Process Industries.

43. McCrone, W.C. and Delley, J.G., The Particle Atlas, The Electron Microscopy Atlas, ed. 2, V. 3, p. 577, Ann Arbor Science, 1973.

44. KA-90 - KA-95, Aluminum Anodes for Cathodic Protection in Marine Environments, Kaiser Aluminum and Chemical Corporation, 1977.

45. Uhlig, H.H., Corrosion and Corrosion Control, John Wiley & Sons, p. 334-350, 1971.

46. Rogers, H.T., Marine Corrosion, p. 272-283, George Newnes Limited, 1968.

47. LaQue, F.L., Marine Corrosion, Causes and Prevention, p. 104-106, John Wiley & Sons, 1975.

48. Latimer, W.M. and Bray, W.C., A Course in General Chemistry, Third Edition, The MacMillan Company, 1940.

49. Richardson, J.A. and Wood, G.C., "The Study of the Pitting Corrosion of Al by Scanning Electron Microscopy", Corrosion Science, V. 10, p. 313-323, 1970.

50. Pryor, M.J., "Contribution to a Discussion on 'A Study of the Pitting Corrosion of Al by Scanning Electron Microscopy' by J.A. Richardson and G.C. Wood", Corrosion Science, V. 11, p. 463-464, 1971.

51. Keir, D.S., Pryor, M.J. and Sperry, P.R., "Galvanic Corrosion Characteristics of Aluminum Alloyed with Group IV Metals", Journal of the Electrochemical Society, V. 114, No. 8, p. 776-782, August 1967.

52. Private communication with Coleman Grandstaff of Reynolds Metal Company, Richmond, Virginia, on November 3, 1977.

53. Vermilyea, D.A., "What I'd Like to Know about Corrosion", First International Congress on Metallic Corrosion, p. 62-71, Butterworths, 1962.

54. Edeleanu, C. and Gibson, J.G., "Influence of Crystal Structure on Corrosion", First International Congress on Metallic Corrosion, p. 72-77, Butterworths, 1962.

55. Bennema, P., "Generalized Herring Treatment of the Equilibrium Form", Crystal Growth; An Introduction, P. Hartman, ed., p. 342-347, North-Holland Publishing Company, 1973.

56. Kano, M., "Some Studies on Corrosion Mechanisms of Metals", Proceedings - Second International Congress on Metallic Corrosion, p. 375-380, NACE, 1966.

57. Buerger, M.J., Introduction to Crystal Geometry, McGraw Hill Book Company, 1971.

58. Scully, J.C., The Fundamentals of Corrosion, Second Edition, p. 56-130, Pergamon Press, 1975.

59. Uhlig, H.H., "Effect of Metal Composition and Structure on Corrosion and Oxidation", Proceedings - Second International Congress on Metallic Corrosion, p. 1-8, NACE, 1966.

60. Kester, D.R., Duedall, I.W., Conners, D.N. and Pytkowicz, R.M., "Preparation of Artificial Seawater", Limnology and Oceanography, V. 12, p. 176-178, December 1967.

61. Kortum, G. and Bockris, J.O'M., Textbook of Electrochemistry, V.2, p. 354-430, Elsevier Publishing Company, 1951.

INITIAL DISTRIBUTION LIST

		No. Copies
1.	Defense Documentation Center Cameron Station Alexandria, VA 22314	2
2.	Library, Code 0142 Naval Postgraduate School Monterey, CA 93940	2
3.	Department Chairman, Code 69 Department of Mechanical Engineering Naval Postgraduate School Monterey, CA 93940	1
4.	Professor A.J. Perkins, Code 69Ps Department of Mechanical Engineering Naval Postgraduate School Monterey, CA 93940	5
5.	Professor R.A. Reinhardt, Code 61Ri Department of Physics and Chemistry Naval Postgraduate School Monterey, CA 93940	1
6.	LT Jon R. Cummings NAVSHIPREPFAC, Yokosuka Japan FPO Seattle, WA 98762	2
7.	Mr. Kenneth J. Graham, Code 61Kg Department of Physics and Chemistry Naval Postgraduate School Monterey, CA 93940	1
8.	Mr. Jack Schrear Kaiser Magnesium P.O. Box 45170 Tulsa, OK 74145	1
9.	Mr. Ray Lindberg Reynolds Metal Company P.O. Box 27003 Richmond, VA 23261	1
10.	Mr. Chuck Schrieber (Plant A2301) Dow Chemical, Freeport Division Freeport, TX 77541	1